



DIPLOMARBEIT

Commissioning and Integration of the ALICE Silicon Pixel Detector

Ausgeführt am
Atominstitut der Österreichischen Universitäten

unter der Anleitung von
Univ.Doz. Univ.Prof. Dipl.-Ing. Dr. Christian Fabjan

durch

Horst Alexander Schödl
Hietzinger Hauptstraße 38E/3
A-1130 Wien

November 6, 2011

Unterschrift

Abstract

The construction of the Large Hadron Collider (LHC) at the European Organization for Particle Physics (CERN) is now in its final stage. It will allow the study of physics in sub-nuclear ranges with an accuracy never achieved in high energy physics before. The ALICE (A Large Ion Collider Experiment) experiment is optimized to study heavy-ion collisions to investigate the behavior of strongly interacting matter at extreme conditions of compression and temperature.

The Silicon Pixel Detector (SPD) constitutes the two inner most layers of the Inner Tracking System (ITS) of ALICE. Due to its high granularity the SPD can provide ALICE with precise tracking information in such a high multiplicity environment as predicted for Pb-Pb collisions (charged particle multiplicities of up to 8,000 per unit of rapidity), which is a fundamental element for adequate secondary vertexing in charm and beauty detection. The SPD barrel consists of 60 staves distributed in two layers at radii 3.9 cm and 7.6 cm around the beam pipe. The inner and outer layer cover the pseudorapidity range of $|\eta| = 1.9$ and 1.4, respectively. To get good track resolution in the low momentum spectrum a maximum material budget of $\sim 1\%X_0$ is allowed per pixel layer in order to have as small influence on the traversing particle as possible. In the design and the production process, the requirements are conformed, so that sensor and readout chip together will have a total thickness of only 350 μm .

This work focuses on the development of the ALICE silicon pixel detector and the integration tests carried out before installation. In particular the ladder tests prior to assembling to a half-stave are presented. Since the bump bond and flip chip bonding processes used in the ladder production include several metal depositions and patterning steps the overall quality of the ladder is strongly dependent on the production process. In order to verify the production quality a series of tests was performed on each ladder, including visual inspection, electrical tests and measurements with a source. The results obtained during the ladder production tests are presented and discussed.

Special emphasis was laid on the effects of long term operation of the half-staves in the experiment. A thermal cycling study was carried out to verify the reliability of the metallic interconnections used in each half-stave. These connections include ultrasonic wire bonds, Al-vias and Pb-Sn solder bump bonds. Failure of these connections will result in malfunctioning or even complete loss of one half-stave and their reliability is therefore crucial for the operation. On one half-stave and for comparison on one readout chip and one single assembly a test of 200 cycles in total was carried out. All three components are cycled in a heating chamber between 15 °C and

45 °C. The test was divided into four steps of 50 cycles. After each step a complete functionality test of the components was performed.

Extensive integration tests of the ALICE SPD were conducted in a clean-room at CERN using the final power supply installation, cables, readout chain and cooling system as foreseen in the experiment. The functionality of each of the 10 sectors was tested separately. All half-staves were tested following a well defined procedure. The operation parameters of every half-stave in terms of minimum threshold, bias voltage and working pixels were measured. The results of the sector tests are presented and compared to the results after integration to the two half-barrels of the SPD.

Kurzfassung

Die letzte Phase der Konstruktion des "Large Hadron Colliders" (LHC) an der europäischen Organisation für Teilchenphysik (CERN) hat begonnen. Dieser Beschleuniger wird die Studie von subnuklearen Phänomenen mit einer noch nie dagewesenen Präzision ermöglichen. ALICE ("A Large Ion Collider Experiment") ist eines der vier Experimente am LHC und ist für Studien von Kollisionen schwerer Ionen konzipiert. Das Ziel dabei ist, stark wechselwirkende Materie bei extremer Energiedichte zu beobachten und die Physik des Quarkgluonplasmas und QCD-Phasenübergänge zu untersuchen.

Der Siliziumpixeldetektor (SPD) bildet die beiden inneren Lagen des ALICE Experiment und kann auf Grund seiner hohen Granularität genaue Informationen über Teilchenspuren in einer Umgebung mit hoher Multiplizität, wie sie im LHC bei Schwerionenkollisionen vorkommt, liefern. Der SPD besteht aus 60 Modulen (Staves), die auf zwei Zylindern mit den Radien 3.9 cm und 7.6 cm um das Strahlrohr positioniert sind. Die innere und äußere Lage decken einen Bereich der Pseudorapidität von $|\eta| = 1.9$ und 1.4 ab. Der SPD liefert ALICE präzise Informationen über Teilchenspuren, die fundamental für die Vermessung von sekundären Vertices sind. Um eine gute Spurauflösung im niedrigen Impulsspektrum zu erhalten, ist ein maximales Materialbudget von $\sim 1\% X_0$ erlaubt, damit der Einfluss auf die durchlaufenden Teilchen möglichst gering ist. Diese Vorgaben wurden im Produktionsprozess berücksichtigt, sodass Sensor und Auslesechip zusammen eine Dicke von nur $350\ \mu\text{m}$ haben.

Der Fokus dieser Arbeit lag unter anderem auf der Entwicklung des ALICE Siliziumpixeldetektors sowie den Integrationstests, welche vor der Installation im Experiment durchgeführt wurden. Die Ergebnisse der "Leitertest" - eine Leiter besteht aus einem Sensor und fünf Pixelchips - werden im Detail präsentiert. Da bei der Leiter-Produktion "Bump-bond" und "Flip-Chip-Bonding" Techniken verwendet wurden, ist die Qualität der Leitern sehr vom Produktionsprozess abhängig. Um die Produktionsqualität zu überprüfen, wurde eine Reihe von Tests durchgeführt, welche eine visuelle Inspektion, Elektroniktests und Messungen mit einer radioaktiven Quelle beinhalteten. Die Ergebnisse der Tests, die während der Leiter Produktion durchgeführt wurden, werden in dieser Arbeit präsentiert und diskutiert.

Ein weiterer Schwerpunkt dieser Arbeit war die Langzeitoperabilität der Detektormodule (Half-Staves) im Experiment. Zu diesem Zweck wurden thermische Alterungs-Tests durchgeführt, um die metallischen Verbindungen, die in einem Half-Staff verwendet werden, zu überprüfen. Diese Verbindungen bestehen aus Aluminium-vias (Durchkontaktierungen) und Pb-Sn Lötverbindungen. Fehler bei diesen Verbindungen resultieren

in eine Störung oder sogar kompletten Ausfall des Half-Staves. Deren Zuverlässigkeit ist daher entscheidend für die Funktionalität des Detektors. Dabei wurden ein Detektormodul, ein Testmodul (Assembly) und ein Pixelchip in einem speziellen Ofen anhand eines vorgegebenen Schema 200-mal auf 45 °C erhitzt, beziehungsweise auf 15 °C abgekühlt. Diese 200 Heizzyklen wurden in vier Einheiten zu je 50 Zyklen unterteilt. Nach jeder Einheit wurden die drei Testeinheiten auf ihre Funktionalität getestet.

Die umfassende Funktionstests des ALICE Siliziumpixeldetektors wurden nach dem Zusammenfügen der Sektoren in einem Reinraum am CERN durchgeführt. Dabei wurden die Netzgeräte, Kabel, Ausleseelektronik und Kühlsystem, wie sie im Experiment vorgesehen sind, verwendet. Alle 10 Sektoren des Detektors wurden einzeln überprüft, d.h. jedes Modul wurde einem definierten Funktionstest unterzogen. Dabei wurden Betriebsparameter jedes Moduls, also der Mindestschwellwert, die Vorspannung und die Anzahl an funktionierenden Pixel, bestimmt. Die Ergebnisse der Sektortests werden in dieser Arbeit präsentiert und mit jenen Werten, die nach der Fertigstellung des Detektors gemessen wurden, verglichen.

Acknowledgements

First, I would like to thank Professor Christian Fabjan, who raised my interest in particle detector physics and offered me the possibility to carry out my diploma theses at CERN.

Special thanks go to Petra Riedler who introduced me with a great understanding, experience and patience to the physics of semiconductor detectors.

Further, I am grateful to Giorgio Stefanini and Vito Manzari for welcoming me in the ALICE SPD group. I would also like to thank the SPD group for the good working atmosphere, especially many thanks to Fadmar Osmic for the introduction to the ladder testing, Simone Ceresa, Henrik Tydesjö, Ivan Amos Cali, Cesar Torcato for their support and work in the DSF, and Alex Kluge, Michel Morel and Michael Burns for their help in electronics.

I also would like to take the opportunity to mention people, who have been important to me. Michael, who helped me correcting my thesis. His positive criticism always brought me down to the factual ground, and my supportive family, who never held me back and was always there when I needed encouragement.

Contents

1	The ALICE Experiment at LHC	1
1.1	The LHC and its Experiments	1
1.1.1	The Large Hadron Collider - LHC	1
1.1.2	The Experiments at LHC	2
1.1.3	ATLAS	3
1.1.4	CMS	3
1.1.5	LHCb	3
1.1.6	ALICE	4
1.2	Physics in ALICE	4
1.2.1	QGP	4
1.2.2	Proton - Proton Collisions	5
1.3	The ALICE Detector System	6
1.3.1	High Momentum Particle Identification Detectors - HMPID	6
1.3.2	Photon Spectrometer - PHOS	6
1.3.3	Photon Multiplicity Detector - PMD	7
1.3.4	Transition Radiation Detector - TRD	8

1.3.5	Time Projection Chamber - TPC	8
1.3.6	Forward Detectors - T0, V0, FMD	9
1.3.7	Time-of-Flight - TOF	10
1.3.8	Zero Degree Calorimeter - ZDC	11
1.3.9	Electromagnetic Calorimeter - EMCAL	11
1.3.10	Inner Tracking System - ITS	11
2	Semiconductor Detectors	15
2.1	Doped Semiconductors	15
2.1.1	Transport Phenomena	17
2.1.2	<i>p-n</i> Junction	20
2.1.3	Charge Carrier Generation	23
2.2	Semiconductor Detector Types	25
2.2.1	Production of Silicon Wafers	25
2.2.2	Silicon Strip Detector	27
2.2.3	Silicon Pixel Detector	28
2.2.4	Silicon Drift Detector	30
3	Component Test - Quality Measurements	32
3.1	The Components of the ALICE SPD	32
3.1.1	Half-Barrel	32
3.1.2	Sector	33
3.1.3	Half-Stave	34
3.2	Test Setup, Measurements and Results	39

3.2.1	The Ladder Test System	40
3.2.2	Half-Stave Tests	44
3.2.3	Aging Tests	52
3.2.4	Optical Tests	61
4	Commissioning and Integration	70
4.1	Test Setup	70
4.1.1	Carbon Fibre Support	70
4.1.2	Cooling System	71
4.1.3	Sector and Half-Barrel Tests	72
4.1.4	Cosmic Test	74
4.2	Measurements and Results	75
4.2.1	Visual Inspection	75
4.2.2	Leakage Current	77
4.2.3	Temperature	78
4.2.4	Minimum Threshold	78
4.2.5	Noisy Pixel	81
4.2.6	Cosmic Test	81
4.2.7	Integration of the SPD in ALICE	83
	Conclusion	85
	A Tables	88
	B General Principle of Semiconductors	89
B.1	Crystal Structure and Energy Bands	89

B.2 Intrinsic Semiconductors	91
C List of Constants	92
Bibliography	101

Chapter 1

The ALICE Experiment at LHC

1.1 The LHC and its Experiments

1.1.1 The Large Hadron Collider - LHC

At CERN the latest High Energy Particle (HEP) accelerator - the Large Hadron Collider (LHC) - is installed in a tunnel of 27 km in circumference. It is planned to collide counter rotating beams of protons or heavy ions (Pb, Ar) at energies of 7 TeV and 5.5 TeV (per nucleon pair), respectively.

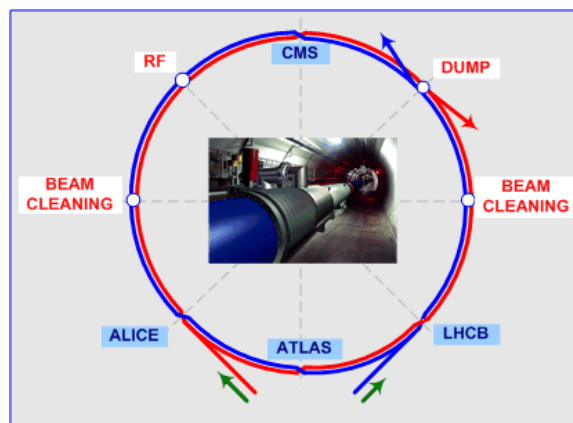


Figure 1.1: The Large Hadron Collider and its experiments [1].

The LHC will not only enter into a new energy domain, but also pro-

vide high luminosity beams. In proton-proton (p-p) collisions a luminosity of $L = 1.0 \times 10^{34} \text{ cm}^{-2}\text{s}^{-1}$ will be achieved, whereas for heavy ion collisions the luminosity will be smaller due to the limitations of the accelerator, $L = 1.0 \times 10^{27} \text{ cm}^{-2}\text{s}^{-1}$. At the nominal intensity, the bunch spacing in the LHC will be 25 ns for p-p collisions and 100 ns for heavy ions. Each of the two beam pipes will be filled with 2,808 bunches in p-p runs and 592 bunches for heavy ion runs.

LHC aims to answer the remaining open questions of the standard model. Special emphasis is laid on the search of the HIGGS particle in the two general purpose experiments ATLAS and CMS. Further, it will be possible to search for supersymmetry in the LHC experiments.

In total there are four experiments built to explore LHC physics: ATLAS and CMS are designed as general p-p experiments; LHCb will focus on B-physics and ALICE is designed to study in particular heavy ion collisions.

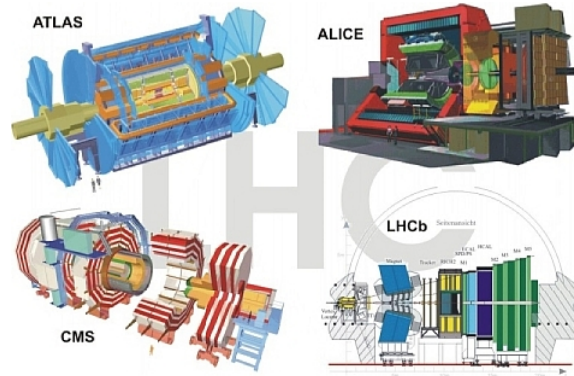


Figure 1.2: ATLAS, CMS, ALICE, LHCb [2].

In the following section a short description of the four experiments and their main goals is given.

1.1.2 The Experiments at LHC

ATLAS and CMS are two general-purpose detectors and therefore they are designed to measure the broadest range of signals. Their main goals are finding the HIGGS boson and to look for evidence of physics beyond the standard model, such as supersymmetry, or extra dimensions.

ALICE is optimized for studying heavy ion collisions. The temperature and density at a collision of lead nuclei is expected to be high enough to generate a quark-gluon-plasma. In this phase quarks and gluons are almost

free. It is believed that the quark-gluon-plasma existed approximately $1 \mu\text{s}$ after the Big Bang. ALICE will be able to investigate heavy ion collision at an unprecedented particle density and energy.

LHCb's specialty is the b-physics ('B factory'). In particular it will measure the parameters of CP violation in the interactions of b-hadrons.

1.1.3 ATLAS

With a length of 46 m and a diameter of 25 m ATLAS (A Toroidal LHC AparatuS) is the largest detector at the LHC.

The tracking detector of ATLAS consists of a Silicon Pixel Detector (SPD), Silicon Strip Detector (SSD) and a Transition Radiation Detector (TRD). It is surrounded by an solenoidal magnet which generates an uniform magnetic field. The Electromagnetic Calorimeter (ECal) and the Hadronic Calorimeter (HCal) build the next two layers of the detector. They are enclosed by the Muon Detector including the Muon Toroidal magnets [3].

1.1.4 CMS

The main detector of CMS (Compact Moun Solenoid) is the Inner Tracker System. It consists of 10 layers of silicon strip and pixel detector with a total surface of $\sim 200 \text{ m}^2$. The next layer, the Electronmagnetic Calorimeter, is built of 80,000 scintillating lead tungsten crystals. The Hadronic calorimeter (HCAL) consists of scintillator layers sandwiched with layers of brass or steel. The HCAL is surrounded by a super-conducting solenoid magnet which provides a 4 Tesla magnetic field. The outermost layer is the muon system and Return Yoke. It consists of Drift Tubes (DT), Cathode Strip Chamber (CSC) and Resistive Parallel Plate Chambers (RPC). For high precise trajectory measurements the DTs are placed in the central barrels while the CSCs are mounted in the End Caps. The RPCs are placed in both the Barrel and the End Caps [4].

1.1.5 LHCb

LHCb will look at CP-violation using the decay modes of b-mesons. LHCb will use the results coming from other experiments like KEK-B and PEP-II. With LHC it will be possible to measure precisely CP-asymmetry and processes, which change the flavor of quarks and leptons. The two main detec-

tors of LHCb are semiconducting trackers and a Ring-Imaging-Cherenkov detector (RICH).

1.1.6 ALICE

ALICE (A Large Ion Collider Experiment) will study mainly collisions of heavy ions. In this collisions matter has a high density - 100 times higher than in a nucleus. A new state of matter is expected at these densities, the Quark-Gluon-Plasma (QGP). In this plasma quarks and gluons do not exist in their compound state like in hadrons. The existence and the properties of this plasma can give answers to questions of quantum chromodynamics (QCD), a better understanding of the confinement and information about the transition from the hadronic state to the QGP. It will also give information about the restoration of the chiral symmetry, the symmetry of right and left handed particles. With the LHC it will be possible to produce this plasma which was created approximately $1 \mu\text{s}$ after the Big Bang. The ALICE detector is specifically designed to observe such states. The inner tracker system (ITS) consists of several layers of semiconducting elements to look especially on particles containing strange- and bottom-quarks. The Time Projection Chamber (TPC) with a volume of 80 m^3 is the largest ever built and will allow to reconstruct the tracks of charged particles and to identify particles by $\frac{dE}{dx}$ measurements in low-momentum regions. The PHOTon Spectrometer (PHOS) consists of lead tungsten crystals and is designed to take the temperature of the collision point by detecting the photons getting out of this point. The Multigap Resistive Plate Chambers, 3.7 m away from the beam axis, will identify the particles based on the data from the other detector layers. Finally a muon system (sandwich composite technology) constitutes the outer regions of the detector.

1.2 Physics in ALICE

1.2.1 QGP

The Quark-Gluon-Plasma (QGP) is a phase where the quarks are deconfined. In normal matter quarks pair with an anti-quark to build mesons or they group in triplets to build baryons. At high temperature and/or density quarks and gluons can exist for a very short time in an unbound state and can move freely. This high temperature and density can be reached by colliding ultra relativistic heavy nuclei i.e. lead or gold nuclei in an accelerator like the LHC. In the phase where the nuclei penetrate each other the

quarks and gluons can move freely and collide inelastically until an equilibrium condition is reached. This equilibrium is called Quark-Gluon-Plasma. Due to the inner pressure the plasma expands and cools down until a critical temperature is reached where the hadronization starts. Heavy ion collisions at CERN-SPS and BNL-RHIC have reported evidence for the QGP. Fig. 1.3 shows a schematic lead-lead collision as it will occur in the ALICE experiment at CERN. The QGP cannot be observed directly due to the short life-time of this phase. Instead other signatures have to be used to measure this medium such as strangeness enhancement or J/Ψ suppression [5].

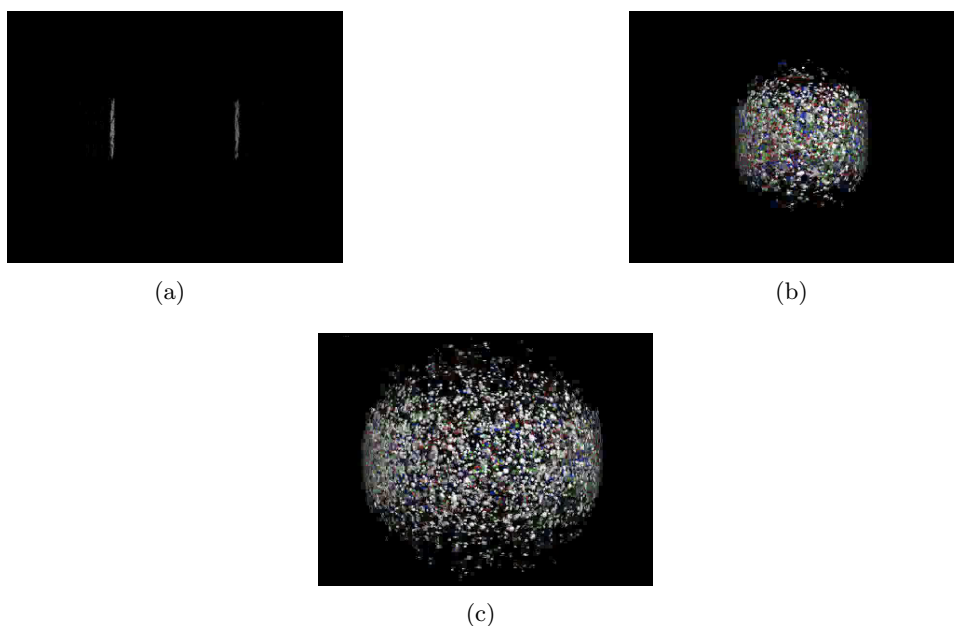


Figure 1.3: Animation of a collision and expansion of two lead bunches with $E_{\text{cm}} = 5.5$ TeV. [6].

1.2.2 Proton - Proton Collisions

The proton-proton program will be an integral part of the ALICE experiment. It will provide first insights into p-p physics in a new energy domain, to study soft hadronic physics and its gradual evolution for a better understanding of the perturbative QCD regime. The study of p-p collisions is essential as comparison with heavy ion data. It will also allow to compare results with previous experiments at SPS. Further the analysis of p-p data will give a reference for the study of ion-ion collisions and provide low multiplicity data to commission and calibrate the various components of the ALICE detector [7].

1.3 The ALICE Detector System

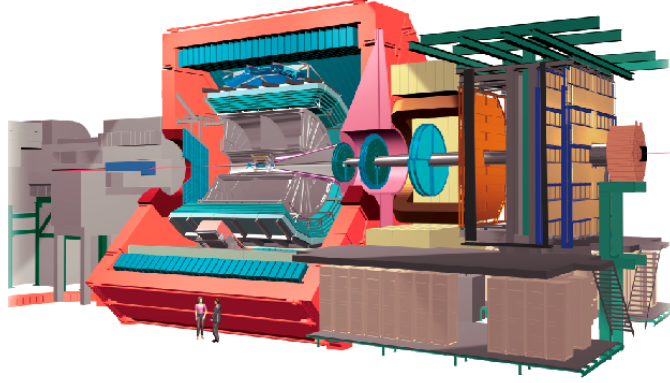


Figure 1.4: Overview of the ALICE experiment [6].

In the following section a more detailed description of the ALICE experiment is presented. Beginning with the outermost layer closest to the L3¹ magnet down to the ITS which houses the Silicon Pixel Detector (SPD). A more deeper view into the SPD is taken in chapter 3.

1.3.1 High Momentum Particle Identification Detectors - HMPID

The ALICE HMPID (Fig. 1.5) consists of seven $1.5 \text{ m} \times 1.5 \text{ m}$ Ring Imaging Cerenkov (RICH) proximity focusing counters, mounted at a radial distance of 4.7 m from the interaction point on a space frame, covering 5 % of the ALICE barrel acceptance. Each of these modules contains six $0.64 \text{ m} \times 0.4 \text{ m}$ CsI photocathodes (PCs) covering a total active area of 11 m^2 . The HMPID identifies pions and kaons in the range of $1 < p_t < 3 \text{ GeV}/c$ and protons and kaons in the range of $2 < p_t < 5 \text{ GeV}/c$ [8], [9].

1.3.2 Photon Spectrometer - PHOS

The Photon Spectrometer is optimized to measure photons with a high resolution and to detect light neutral mesons (π^0 and η) through their two-photon decay. The PHOS (Fig. 1.6) has been designed to cover the pseudorapidity range $|\eta| = 0.12$ and an azimuthal domain of 100 degrees. The detector consists of five identical modules, each with 3,584 channels, 17,920 in total.

¹The Magnet is called L3, since it is reused from the former LEP experiment L3.



Figure 1.5: Photograph of the HMPID. ©A.Saba [10]

Each detection channel consists of a $2.2 \times 2.2 \times 18 \text{ cm}^3$ lead-tungstate crystal, PbWO_4 (PWO), coupled to an Avalanche Photo-Diode (APD) and a low-noise preamplifier [11].

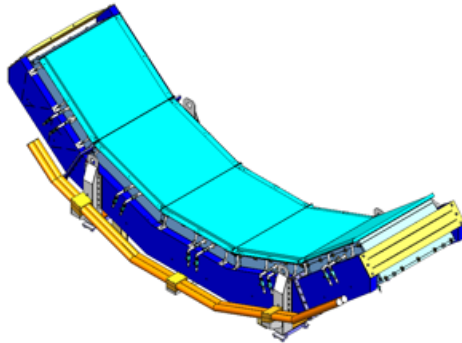


Figure 1.6: Scheme of the PHOS detector [12].

1.3.3 Photon Multiplicity Detector - PMD

The pre-shower Photon Multiplicity Detector has a fine granularity and full azimuthal coverage in the pseudo-rapidity region $1.8 \leq \eta \leq 2.6$. It will be mounted on the L3 magnet door 5.8 m from the interaction point. Charged particles are rejected using a charged particle veto (CPV) in front of the converter (Fig. 1.7). Both the CPV and the pre-shower converter are based on a honeycomb proportional chamber design. There are $\sim 2 \times 10^5$ cells each having an area of 1 cm^2 . The honeycomb wall forms a common

cathode, operated at a high negative voltage. The signal will be read out from the anode wires at ground potential using a specially developed ASIC, MANAS, for the front-end electronics. The PMD will be able to take data in conjunction with the dimuon spectrometer and other high rate detectors [13].



Figure 1.7: Scheme of the cross-section of the PMD showing the veto plane, lead converter and the preshower plane. SS denotes the support plate on which lead plates and chambers will be mounted [14].

1.3.4 Transition Radiation Detector - TRD

The Transition Radiation Detector will be installed between the space frame and the Time Projection Chamber. The TRD barrel has a radius range between 2.9 m and 3.7 m from the beam axis and 7 m length along the beam axis covering the central rapidity region of $|\eta| < 0.9$. The TRD is divided into 540 modules organized in 18 sectors and 6 layers. The detector has a total area of 750 m² of gas chambers with radiators for particle tracking and electron identification above 1 GeV/c. The TRD will also allow to trigger on high- p_t e^+e^- pairs in order to reduce the collision rate to the readout event rate, by increasing the statistics on rare signals such as J/Ψ and Υ [15], [16].

1.3.5 Time Projection Chamber - TPC

The Time Projection Chamber (Fig. 1.8) is the main detector in the central barrel of ALICE. Its functions are

- track finding with an efficiency better than 90 %,

- charged particle momentum measurement with a resolution better than 2.5 % for electrons with a momentum of about 4 GeV/c,
- particle identification with an $\frac{dE}{dx}$ resolution better than 6 % and
- two-track separation in the region of $p_t < 10$ GeV/c and a pseudo-rapidity of $|\eta| < 0.9$.



Figure 1.8: Photograph of the TPC. ©A. Saba [10]

The TPC is a cylindrical gas detector with an active volume between 85 cm to 250 cm in radial direction and a length of 500 cm along the beam axis. A high voltage (HV) electrode is located at its center, which will be aligned to the interaction point, dividing the barrel into two symmetric drift volumes of 250 cm length. The HV electrode, which consists of an aluminized stretched Mylar foil, and two opposite axial potential degraders create a highly uniform electrostatic field. The potential of the drift region is defined by Mylar strips wound around 18 inner and outer support rods [6], [17].

1.3.6 Forward Detectors - T0, V0, FMD

The Forward Detector (FWD) consists of two arrays of Cherenkov radiators (T0), two rings of plastic scintillators (V0) and five rings of silicon strip detectors (FMD). Fig. 1.9 shows a scheme of the detector. It can be seen that the system consists of detectors on both sides (side A and C) of the interaction point (IP) at various distances along the beam axis. In this section a short description of these three detectors is given.

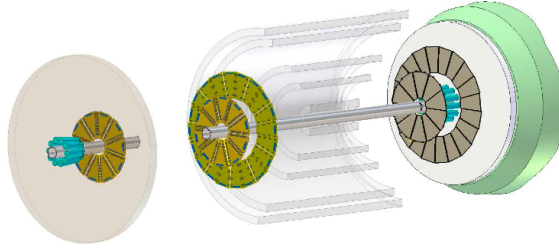


Figure 1.9: Schematic of the placement of T0, V0 and FMD on both sides of the interaction point of ALICE. The five layers of the ITS are sketched in the central region[18].

The T0 detector consists of two arrays of PMTs equipped with Cherenkov radiators and is positioned on the opposite side of the IP. The main task of the T0 is to supply a signal for the level 0 trigger for ALICE, in particular for the Transition Radiation Detector (TRD) and delivering a reference time for the Time Of Flight (TOF) detector. The T0 has a time resolution better than 50 ps and covers a range in pseudo-rapidity of $-3.3 \leq \eta \leq -2.9$ and $4.5 \leq \eta \leq 5.0$, respectively.

The V0 consists of two disks of segmented plastic scintillator tiles (eight segments) read out by optical fibres. It covers approximately the same range of pseudo-rapidity as the FMD. The main functionality of the V0 system is to provide the online level zero (L0) centrality trigger for ALICE by setting a threshold on deposited energy, and to provide a background rejection capability for the dimuon arm.

The FMD finally consists of 51,200 silicon strip channels distributed over five ring counters. There are two types of ring counters which have 20 and 40 sectors each in azimuthal angle. The main function of the FMD is to provide precise charged particle multiplicity measurements in the pseudo-rapidity range of $-3.4 \leq \eta \leq -1.7$ and $1.7 \leq \eta \leq 5.0$, respectively. Due to the readout time of $\approx 13 \mu\text{s}$ the FMD will only contribute to the level 2 trigger in ALICE. Together with the pixel detector system the FMD will provide charged particle multiplicity distributions for all collision types in the pseudorapidity range of $-3.4 \leq \eta \leq 5.0$ [18].

1.3.7 Time-of-Flight - TOF

One technique to identify charged particles in ALICE is the use of a Time-of-flight detector. It will allow a separation of kaons from pions up to 2.5 GeV/c or protons from kaons up to 4 GeV/c, which requires a global time resolution

of $\simeq 100$ ps. The ALICE TOF is arranged in 18 supermodules, covering 360° in azimuth and a range in pseudo-rapidity of $|\eta| < 1$ with a total area of $\simeq 150 \text{ m}^2$. Each Supermodule consists of five modules, containing between 15 and 19 Multigap Resistive Plate Chambers (MRPC) strips. Each strip contains two stacks of resistive glass plates, separated with equal sized spacers, creating a series of uniform gas gaps with voltage applied to the external surfaces. The MRPC stack is made of six layers of glass forming five gaps with $250 \mu\text{m}$ width [19], [20]. This technique, especially developed for ALICE, provides a time resolution of ~ 50 ps.

1.3.8 Zero Degree Calorimeter - ZDC

The event by event determination of the centrality plays a basic role in heavy ion collisions. It is used at the trigger level to enhance the sample of central collisions and to estimate the energy density reached in the interactions. The Energy E_S carried away by non-interacting nucleons (spectators) is the measurable quantity most directly related with the centrality of the collision. The ZDC consists of two radiation hard calorimeters, one for the spectator neutrons, the other for the spectator protons made of quartz-fibre, which allows a very compact design of the detector [21].

1.3.9 Electromagnetic Calorimeter - EMCAL

The Electromagnetic Calorimeter (Fig. 1.10) is a large Pb-scintillator sampling calorimeter with cylindrical geometry, located ~ 4.5 m radial from the beam axis inside the L3 magnet. Covering a range in pseudo-rapidity of $|\eta| < 0.7$ the EMCAL is positioned opposite in azimuth to the PHOS. The calorimeter is segmented into 12,672 projective towers, each covering $\delta\eta \times \delta\phi \sim 0.014 \times 0.014$. The Readout fibers are coupled to an Avalanche Photodiode (APD) sensor. The EMCAL provides level 0 and 1 triggers for photons, electrons and jets [6].

1.3.10 Inner Tracking System - ITS

The basic functions of the Inner Tracking System are the determination of the primary vertex and of the secondary vertices necessary for the reconstruction of charm, and hyperon decays, particle identification and tracking of low-momentum particles. It will also contribute to the track reconstruction by improving the momentum resolution obtained by the TPC. This will

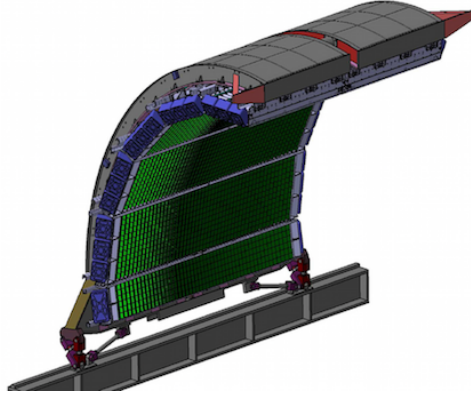


Figure 1.10: The array of super modules of the EMCAL shown in their installed position on the support structure [6].

be beneficial for practically all physics topics which will be addressed by the ALICE experiment. The global event features will be studied by measuring the multiplicity distributions and the inclusive particle spectra. The detector system consists of six layers of coordinate-sensitive detectors, covering the central rapidity region $|\eta| < 0.9$ for vertices located within the length of the interaction diamond ($\pm 1\sigma$). In the next section a short overview is given of the different parts of the ITS, which are the Silicon Strip Detector (SSD), the Silicon Drift Detector (SDD) and the Silicon Pixel Detector (SPD).

Silicon Strip Detector

The Silicon Strip Detector (SSD) (Fig. 1.11) is crucial for the connection of tracks from the ITS to the TPC. The two layers of the detector at radii 39.1 cm and 43.6 cm are made of double-sided strip detectors (SSD) and have a length of 45.1 cm and 50.4 cm, respectively. The sensors, each with 768 strips of 25 - 50 μm wideness and 95 μm pitch, have an area of $75 \times 42 \text{ mm}^2$ and a thickness of 300 μm . The stereo angle between the strips on one sensor is ± 17.5 milliradians. The SSD also provides $\frac{dE}{dx}$ information to assist particle identification for low-momentum particles [22], [23].

Silicon Drift Detector

The Silicon Drift Detector (SDD) has been selected to equip the two intermediate layers of the ITS, since they combine a very good multi-track capability with $\frac{dE}{dx}$ information. At least three measured samples per track, and therefore, at least four layers carrying $\frac{dE}{dx}$ information, are needed. The

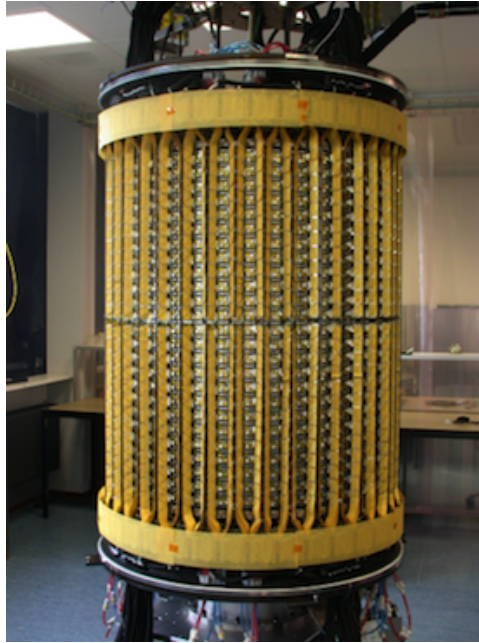


Figure 1.11: The Picture shows the complete SSD mounted on the Carbon fiber support [6].

SDDs, each $7.0 \times 7.5 \text{ cm}^2$ in active area, are mounted on linear structures so called ladders, each holding six detectors for the inner and eight detectors for the outer layer. The detector consists of two barrel layers located at radii 14.9 cm and 23.8 cm, respectively. The inner layer is composed in total of 14, the outer layer of 22 ladders. Fig. 1.12 shows a picture of the one SDD ladder [24].

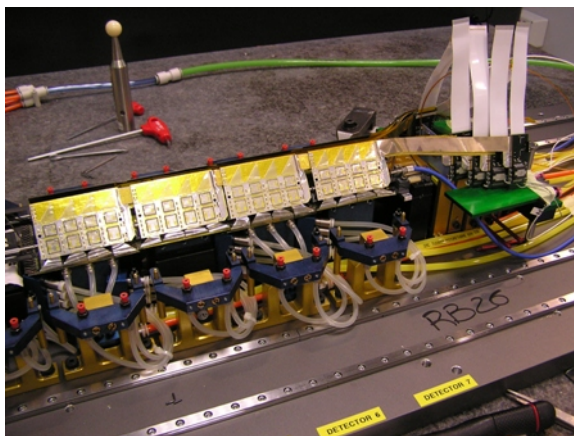


Figure 1.12: The 1st ladder of the ITS Silicon Drift Detector showing four modules with readout and end cap electronics [6].

The ALICE Silicon Pixel Detector

The ALICE Silicon Pixel Detector (SPD) constitutes the two innermost layers of the ALICE inner tracking system (Fig. 1.13) [23]. It consists of two barrel layers located at radii of 3.9 cm and 7.6 cm. The inner and outer layer cover the pseudorapidity range of $|\eta| = 1.9$ and 1.4, respectively. The two barrels are divided into 10 sectors, each containing 12 modules (half-staves). The whole SPD contains 1,200 mixed signal ASICs in radiation hardened design produced in $0.25 \mu\text{m}$ CMOS process with a total of 9.8 million pixel cells. All communication (data, control, clock) with the off-detector electronics is carried out via bidirectional optical links. An evaporative cooling system with C_4F_{10} is used to remove the 1.5 kW dissipated power from the SPD. The material budget limitations require a careful design of all components of the SPD in order to achieve a total material budget per layer of $\sim 1\% X_0$ [25], [6].

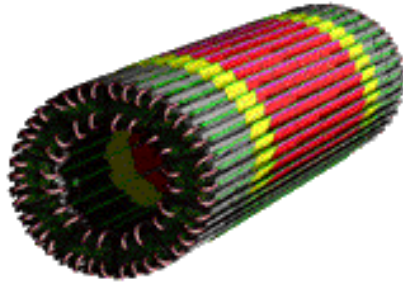


Figure 1.13: The ALICE Silicon Pixel Detector.

A more detailed description of the SPD will be given in chapter 3. In the following chapter a summary of semiconductor detectors and their working principle is presented.

Chapter 2

Semiconductor Detectors

Semiconductor detectors as solid state detectors offer a compact design. The average energy to generate an e^-h^+ -pair is only 3.6 eV which is approximately $\frac{1}{10}$ of the energy needed to produce ions in a gas detector. The energy transferred of a particle traversing the semiconductor is directly converted into an electrical signal. Semiconductor detectors have a high efficiency and a low dead time. As silicon pixel detector they provide high 3D spatial resolution and are therefore suitable for primary and secondary vertexing, also in high multiplicity environments. At the LHC semiconductor detectors are mainly used close to the interaction point (IP). The high performance electronics requires special cooling systems and the high production costs usually narrow the field of application of semiconductor detectors.

In this chapter some basic properties of semiconductors are discussed. Further, a review of the various transport phenomena in semiconductors under the influence of an electric field is given. The general behavior of a single-crystal semiconductor material containing a p-n junction is explained at the end of the first section. The last two sections give a general overview about semiconductor detector types and describe in more detail the Hybrid Pixel Detector as used at LHC.

2.1 Doped Semiconductors

In this section the important properties of semiconductors as detector material are described. A more detailed description of the properties of semiconductors can be found in Appendix B.

The conductivity of semiconductors, which makes them interesting as detector material, may easily be modified by introducing impurities into their crystal lattice. The process of adding controlled impurities to a semiconductor is known as *doping*. The amount of impurity (*dopant*) added to an *intrinsic* (pure) semiconductor varies its level of conductivity. If silicon is doped with arsenic atoms, which has five valence electrons, it becomes a *n-type* semiconductor. Arsenic is referred as a *donor*. Similarly, replacing silicon atoms with boron atoms results in a *p-type* semiconductor and boron is called an *acceptor*. In the doped semiconductor impurity energy levels are introduced in the forbidden band gap and the semiconductor becomes *extrinsic* [26]. Fig. 2.1 shows schematically a silicon lattice in which individual silicon atoms are replaced by either an arsenic or a boron atom.

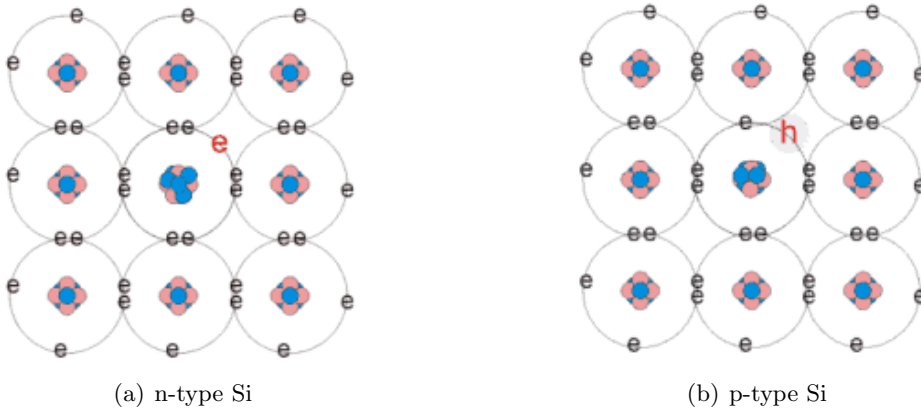


Figure 2.1: Schematic bond pictures for doped silicon [27].

The electron and hole concentrations in a n-type semiconductor can be expressed as

$$n_n = \frac{1}{2} \left[N_D - N_A + \sqrt{(N_D - N_A)^2 + 4n_i^2} \right], \quad (2.1)$$

$$p_n = \frac{n_i^2}{n_n}. \quad (2.2)$$

Similarly, one can obtain the hole and electron concentration for a p-type semiconductor

$$p_p = \frac{1}{2} \left[N_A - N_D + \sqrt{(N_A - N_D)^2 + 4n_i^2} \right], \quad (2.3)$$

$$n_n = \frac{n_i^2}{p_p}. \quad (2.4)$$

The subscript n and p refer to the n-type and p-type semiconductor, respectively. N_D is the donor concentration and N_A is the acceptor concentration [26].

2.1.1 Transport Phenomena

In this section we consider the transport phenomena in a semiconductor. In a n-type semiconductor with uniform donor concentration in thermal equilibrium the kinetic energy of an electron can easily be calculated by

$$\frac{1}{2}m_n v_{th}^2 = \frac{3}{2}kT \quad (2.5)$$

where m_n is the effective mass of electrons and v_{th} is the average thermal velocity. The electrons move rapidly in all directions and they collide with lattice atoms. The distance between two collisions, the *mean free path* is around 10^{-5} cm and the time between two collisions, the *mean free time* τ_c is ~ 1 ps.

If an electric field E is applied, the electrons are accelerated along this field. The resulting drift velocity can be described using the formula

$$v_n = -\frac{q\tau_c}{m_n}E \quad (2.6)$$

or with the *electron mobility* $\mu_n = \frac{q\tau_c}{m_n}$

$$v_n = -\mu_n E. \quad (2.7)$$

A similar equation can be found for holes $v_p = -\mu_p E$. The mobility is related to the mean free time, which on the other hand is depending on the scattering mechanisms, mainly lattice scattering and impurity scattering. Latter becomes less significant at higher temperatures and the lattice scattering is then the dominating part.

The sum of the probabilities of the different scattering mechanisms leads to the probability of a collision in a unit time, $\frac{1}{\tau_c}$ and can be calculated using the formula

$$\frac{1}{\tau_c} = \frac{1}{\tau_{c,lattice}} + \frac{1}{\tau_{c,impurity}}. \quad (2.8)$$

According to this equation the *mobility* can then be expressed as

$$\frac{1}{\mu} = \frac{1}{\mu_l} + \frac{1}{\mu_i}. \quad (2.9)$$

For lightly doped semiconductors the lattice scattering mechanism dominates and the mobility decreases as the temperature increases. For a given temperature the mobility decreases with increasing impurity concentration. Further, the electron mobility ($\sim 1400 \text{ cm}^2\text{V}^{-1}\text{s}^{-1}$ in Si at 300 K) is greater than the one of holes ($\sim 4500 \text{ cm}^2\text{V}^{-1}\text{s}^{-1}$ in Si at 300 K) due to the smaller mass of the electrons.

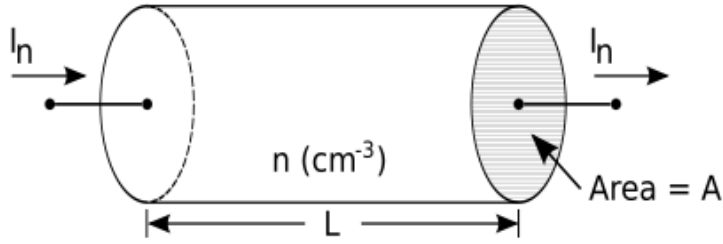


Figure 2.2: Current conduction in a uniformly doped semiconductor [26].

Due to the transport of the electrons and holes along the electrical field, a current, the *drift current*, is induced. In a semiconductor sample with an area A , a length L and a carrier concentration of n electrons/ cm^3 (Fig. 2.2), the electron current density J_n is then

$$J_n = \frac{I_n}{A} = -qnv_n = qn\mu_n E \quad (2.10)$$

and for holes the hole current density J_p can be expressed as

$$J_p = \frac{I_p}{A} = qnv_p = qn\mu_p E. \quad (2.11)$$

The total current flowing in the sample is then the sum of J_n and J_p which leads to the conductivity

$$\sigma = q(n\mu_n + p\mu_p). \quad (2.12)$$

The corresponding resistivity of the semiconductor, which is the reciprocal of σ , is given by

$$\rho = \frac{1}{\sigma} = \frac{1}{q(n\mu_n + p\mu_p)}. \quad (2.13)$$

For extrinsic semiconductors only one component of the resistance and conductivity, respectively, is significant.

For n-type semiconductors the resistance is then

$$\rho = \frac{1}{qn\mu_n} \quad (2.14)$$

and for p-type semiconductors the resistance is then

$$\rho = \frac{1}{qp\mu_p}. \quad (2.15)$$

If there is a local variation of carrier concentrations in a semiconductor, the carriers tend to move from regions of high concentration to a region of low concentration. This induced current is called *diffusion current* and is given by

$$J_n = qD_n \frac{dn}{dx} = q\left(\frac{kT}{q}\mu_n\right) \frac{dn}{dx}, \quad (2.16)$$

where D_n is the *diffusivity*, which can be expressed with the Einstein relation as

$$D_n = \left(\frac{kT}{q}\mu_n\right). \quad (2.17)$$

This relation couples the two important transport constants, the diffusivity and the mobility.

Whenever the thermal equilibrium is disturbed, that means $pn \neq n_i^2$, processes are initiated which restore the system until the equilibrium is reached. These recombination processes can be classified as direct and indirect processes. In a direct-bandgap semiconductor, such as GaAs, direct recombination takes place whereas in an indirect-bandgap semiconductor (e.g. Si) indirect recombination is dominant. The indirect recombination can further be divided in bulk and surface recombination processes.

2.1.2 *p-n* Junction

Using semiconductors as a particle detector two important facts have to be considered. First, recombination of charge carriers produced by the traversing particle should be avoided. Second, no free charge carriers should be left in the sensor volume. For this, a semiconductor material containing both n-type and p-type regions forming a p-n junction and operated in a reversed biased state is used (Fig. 2.3).

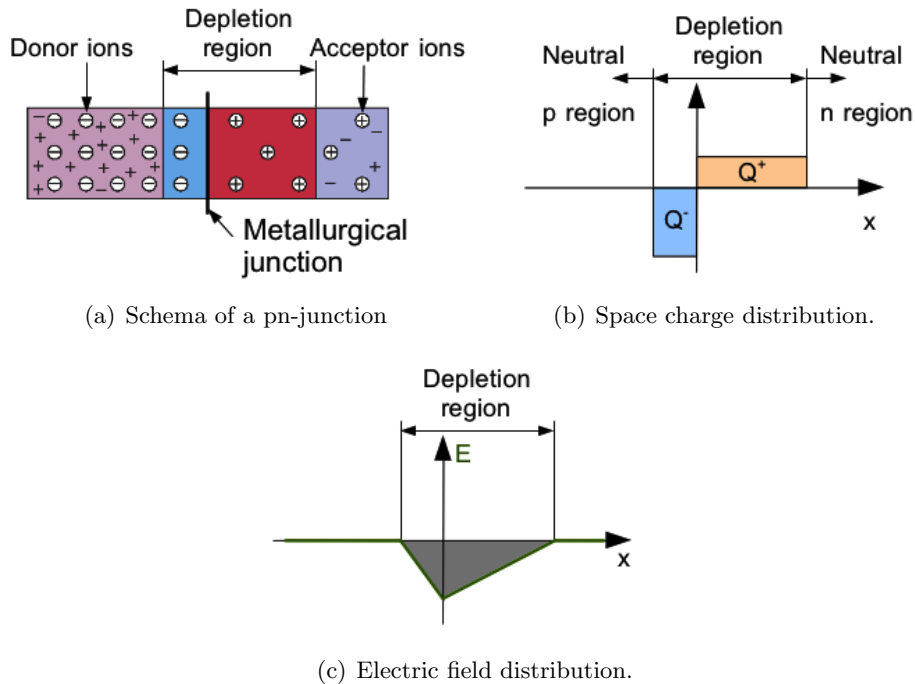


Figure 2.3: Electrical characteristics of an pn-junction with abrupt doping changes at the metallurgical junction [28].

Due to the large carrier concentration gradients at the junction a carrier diffusion is caused, where the holes move from the p-side to the n-side and the electrons, vice versa, from the p-side to the n-side. An electrical field

builds up due to the uncompensated acceptor (N_A^-) and donor (N_D^+) ions which are fixed in the lattice. At thermal equilibrium a total electrostatic potential, the *build-in potential* V_{bi} , between the p-region and n-side neutral regions can be obtained by

$$V_{bi} = \frac{kT}{q} \ln \frac{N_A N_D}{n_i^2}, \quad (2.18)$$

where N_A and N_D is the acceptor and donor density, respectively and n_i is the intrinsic carrier density. Between the two sides lies a neutral regions, the *depletion zone* where the density of mobile carriers is zero. The extension w_p and w_n , respectively, of the depletion zone into the p-side and n-side can be expressed as a function of the electrostatic potential

$$w_n = \sqrt{\frac{2\epsilon_s V_{bi}}{q N_D (1 + \frac{N_D}{N_A})}}, \quad (2.19) \quad w_p = \sqrt{\frac{2\epsilon_s V_{bi}}{q N_A (1 + \frac{N_A}{N_D})}}, \quad (2.20)$$

where ϵ_s is the *dielectric constant* of the semiconductor. It can be seen that in case one side is more doped than the other, the depletion zone will extend farther into the lighter doped region. For instance, if $N_A \gg N_D$, then the width w_n is larger than w_p , which means that the depletion region is almost entirely in the n-side of the junction [29]. The total width of the depletion zone can then be expressed as

$$W = w_n + w_p = \sqrt{\frac{2\epsilon_s V_{bi}}{q} \left(\frac{N_A + N_D}{N_A N_D} \right)}, \quad (2.21)$$

where V_{bi} is positive for forward bias and negative for reverse bias. Due to the electrical configuration of the p-n junction, the depletion layer can also be interpreted as a capacitor, which influences the noise characteristic when using it as a detector. The capacitance of this parallel-plate capacitor is given by

$$C_j = \epsilon_s \frac{A}{W}, \quad (2.22)$$

where C_j is the capacitance of the junction. A is the depletion area, ϵ_s the dielectric constant of the semiconductor and W the previously derived

depletion width.

Until now all considerations referred to a p-n junction in thermal equilibrium. If a voltage is applied to a junction the balance between the diffusion current and the drift current is disturbed.

For germanium p-n junction at low current densities the current-voltage characteristics can be described using the *ideal diode equation*

$$J = J_s \left(e^{\frac{qV}{kT}} - 1 \right), \quad (2.23)$$

where J_s is the *saturation current density* [26]. For silicon (and germanium arsenide) this equation gives only a qualitative approach. Due to generation and recombination procedures the total current in reversed bias operation is

$$J_R = q \sqrt{\frac{D_p}{\tau_p} \frac{n_i^2}{N_D}} + \frac{qn_i W}{\tau_g}, \quad (2.24)$$

where D_p is the *diffusivity* of holes, τ_p the *lifetime* of a hole and τ_g the *generation lifetime*. For forward bias a similar equation can be derived

$$J_F = q \sqrt{\frac{D_p}{\tau_p} \frac{n_i^2}{N_D}} e^{\frac{qV}{kT}} + \frac{qn_i W}{2\tau_r} e^{\frac{qV}{2kT}}, \quad (2.25)$$

where τ_r is the effective recombination lifetime. For a sufficiently high reverse voltage the p-n junction breaks down which leads to a very large current. This current cannot be described with the above formula. The two important breakdown mechanisms are the tunneling effect and the avalanche multiplication. The breakdown voltage V_B can be determined from the solution of Poisson's equation

$$V_B = \frac{E_C W}{2}, \quad (2.26)$$

where E_C [V/cm] is the *critical electric field* and W the depletion width.

2.1.3 Charge Carrier Generation

The ALICE experiment aims to measure particles in a wide momentum range, including those below 100 MeV/c. These low momentum tracks can only be detected with the ITS. The expected particles which can be detected in the pixel layers of the ALICE experiment are mainly pions, electrons and protons. The expected doses in the SPD layers are 2.5×10^3 Gy for the inner layer and 6.94×10^2 Gy for the outer layer. The fluence for both layers as 1 MeV-Neutron-Equivalent is $2.9 \times 10^{12} \text{ cm}^{-2}$ and $1.72 \times 10^{12} \text{ cm}^{-2}$, respectively.

The basis of detecting a particle is the interaction with the detector material. In the following section a brief overview of the various interaction processes is given. Fig. 2.4 shows the operating principle of a semiconductor detector. The p⁺n junction is operated in reversed bias mode. A charged particle or x-ray passing through the fully depleted n-bulk generates e⁻h⁺ pairs by ionization which are moving towards the electrodes due to the electric field in the bulk. The generated signal can then be registered in the electrodes.

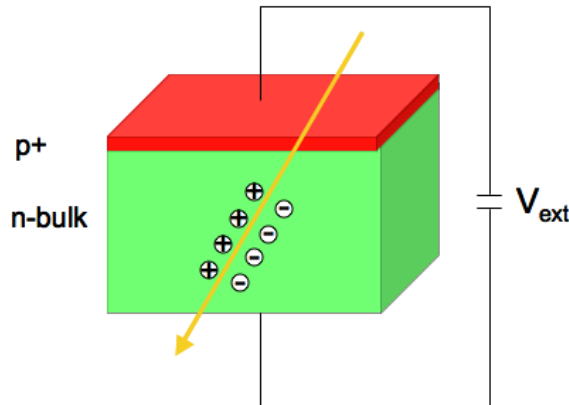


Figure 2.4: p⁺n junction reversed biased. When a particle passes e⁻h⁺-pairs are created.

Energy Loss of Heavy Charged Particles

Two main processes characterize the passage of charged particles through matter:

- inelastic collisions with electrons of the material and

- elastic scattering from nuclei.

Also other processes occur but are rather rare in comparison to those listed above. The major part of the energy loss is due to inelastic collisions which are purely statistical. The elastic scattering is more important for heavier particles like α -particles. However, since the number of particles of collisions per path length is large, the fluctuation is small and we can use the average energy loss per unit path length. This energy loss ($\frac{dE}{dx}$) was first calculated by Bohr and later with quantum mechanical arguments by Bethe and Bloch (for detailed list of the constants see Appendix C [30]):

$$-\frac{dE}{dx} = 4\pi \frac{Z_1^2 e^4}{m_e c^2 \beta^2} \rho N_a \frac{Z}{A} \left[\ln \left(\frac{2 m_e \beta^2 \gamma^2 c^2}{I} \right) - \beta^2 - \frac{\delta}{2} - \frac{C}{Z} \right] \cdot (1 + \nu). \quad (2.27)$$

Fig. 2.5 shows the energy loss in different materials as a function of $\beta\gamma$. dE/dx is proportional to β^{-2} for small velocities ($\beta \ll 1$), whereas in high relativistic regions ($\beta \approx 1$) the energy loss increases logarithmic. This increase is very flat for most of the interesting particles and materials in particle physics. Particles with energies around the minimum ($\beta \simeq 3$) are often referred as *Minimum Ionising Particles (MIPs)*.

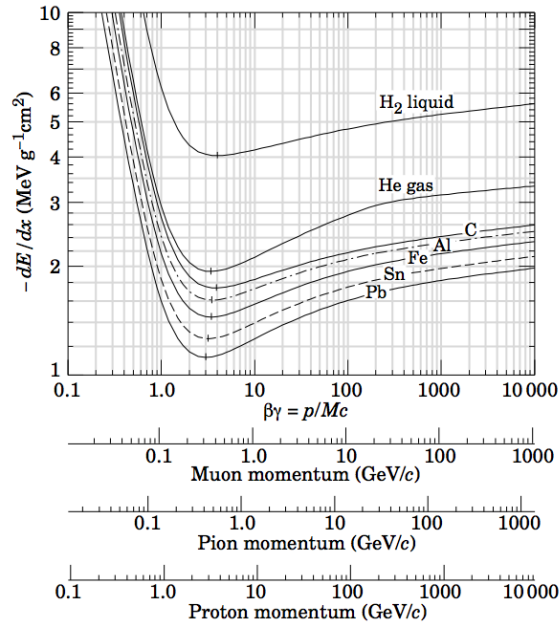


Figure 2.5: Mean energy loss rate in liquid (bubble chamber) hydrogen, gaseous helium, carbon, aluminum, iron, tin and lead [31].

2.2 Semiconductor Detector Types

Nowadays, semiconductor devices can be found in a broad range of applications. Especially silicon is widely used as detector material, since well known industrial production processes can be adapted for the experimental application. Position sensitive silicon detectors are usually based on pn-junctions with segmented electrodes. In High Energy Physics (HEP) semiconductors are commonly used as high-resolution spatial detectors like micro-strip detector, pixel detector and drift detector. In the following section a short overview of the silicon wafer production is given and subsequent to this a brief introduction to this three detector types is presented.

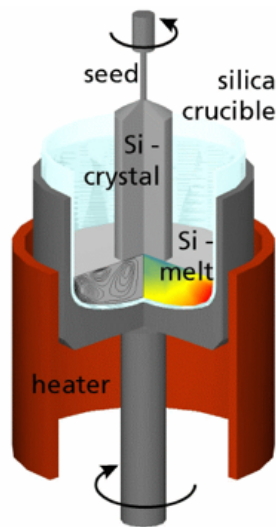
2.2.1 Production of Silicon Wafers

To produce a silicon wafer polycrystalline silicon is molten at $\sim 1,420$ °C and grown into a cylindrical ingot with a single crystal orientation. One can distinguish between two growing techniques:

- In the Czochralski Technique (CZ) the Si crystal is pulled out of the silicon melt which is placed in a silicon crucible (Fig. 2.6a). The silica crucible is dissolving oxygen into the melt which leads to a high O₂ concentration in the ingot. The CZ is usually used for microelectronics.
- In the Float Zone (FZ) process the end of a long polycrystalline silicon rod is locally melted using a radio frequency heater and brought in contact with a monocrystalline silicon seed (Fig. 2.6b). The zones slowly migrates through the poly rod leaving behind the final perfect crystal. The FZ gives a very pure crystal and is mainly used for silicon sensors.

After the ingots are produced one or more flat regions are ground along the length of the ingot to indicate the crystal orientation, then they are sliced to get wafers. The wafers, which are lapped to receive an even and flat surface, are etched to remove the damaged crystal layers and finally polished to get a perfect surface. Out of this wafers sensors for pixel or micro-strip detectors can be produced by the so called *planar process*. This process is adapted from the microelectronic industry and can be divided into steps listed below [32]:

1. N-type wafer is cleaned and oxidized by heating it in an O₂ atmosphere at ~ 1000 °C (SiO₂).



(a) Czochralski technique



(b) Floating Zone process

Figure 2.6: The two main growing techniques for producing silicon ingots [32].

2. Photoresist is spun onto one side of the wafer.
3. A mask (made of quartz with Al pattern) is placed on top of the wafer and illuminated.
4. The non exposed areas of the surface are then etched and the SiO_2 in this area is removed.
5. The remaining SiO_2 acts as a mask.
6. The patterned side is implanted with boron. The backside is implanted with As.
7. The wafer is heated to $600 - 800^\circ\text{C}$ to anneal the crystal damage caused by implantation and to get the implanted atoms properly built into the lattice.
8. Aluminum is deposited either by sputtering or evaporation to provide the electrical connection to the diode.
9. Photolithographic etching of the aluminium.
10. Heating of the wafer to create a good connection between the silicon and aluminum ($\sim 400^\circ\text{C}$).
11. Adding of a mechanical protection layer on some parts of the sensor (e.g. polyimide or SiO_2).

2.2.2 Silicon Strip Detector

Silicon strip detectors provide a 1-dimensional information about the particle passing through the detector. A high resistivity n-type silicon detector ($\rho > 2 \text{ k}\Omega\text{cm}$) is used as the basic material onto which in the simplest case p^+ diode strips with Al-contacts are implanted. The detector has a thickness in the order of $300 \mu\text{m}$. On the backside a n^+ -layer is embedded to provide a good resistive contact. For a minimum ionizing particle the average energy loss per path length ($\frac{dE}{dx}$) in Silicon is $39 \text{ MeV}/\mu\text{m}$, the average ionization energy $I_0 = 3.62 \text{ eV}$. Thus, for a $300 \mu\text{m}$ detector $3.2 \times 10^4 e^-h^+$ -pairs are expected. Fig. 2.7 shows a layout of a micro-strip detector. The position resolution of a silicon strip detector is around a few μm due to charge sharing between neighboring strips [33].

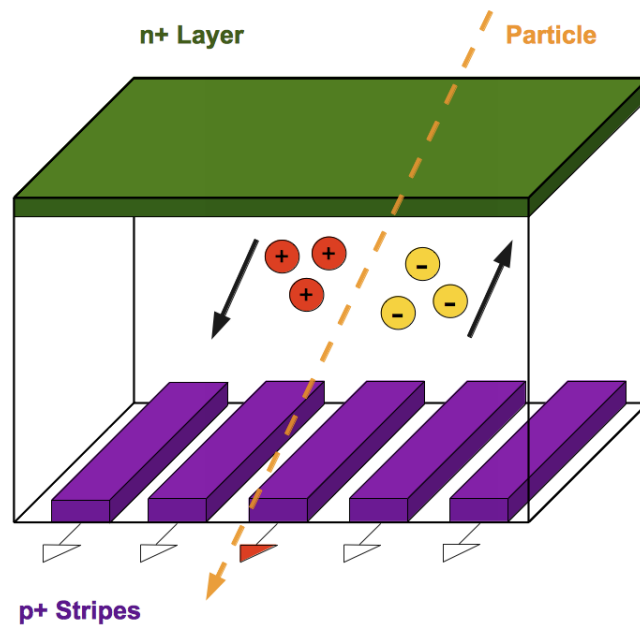


Figure 2.7: Layout of a silicon strip detector. The strip pitch can be between $\sim 10 - 100 \mu\text{m}$ [33].

It is also possible to achieve two dimensional information with a micro-strip detector by sticking micro-strip detector modules together (more detector material) or by using a second strip layer orthogonal to the first one, which keeps the detector thickness constant. The production and handling of such modules is rather complicated and at high occupancy they deliver ambiguous signals. A possible solution to get 2-dimensional information offers the silicon pixel detector which will be explained in the next section [32], [28].

2.2.3 Silicon Pixel Detector

A pixel detector has a 2-dimensional matrix of sensitive elements, each having its own pulse processing electronics. The first silicon pixel detectors based on charged coupled devices (CCD) were built in the late 1980s. Currently hybrid pixel detectors are used in HEP experiments. New types of SPDs are being investigated, such as monolithic silicon pixel detectors e.g.

- Hybrid Silicon Pixel Detector
- Monolithic Silicon Pixel Detector

The following pages give a short overview of these detector types.

Hybrid Silicon Pixel Detector

A hybrid silicon pixel detector (Fig. 2.8) consists of three parts:

- sensor (silicon in most applications)
- Readout chip (p⁺n silicon pixel detector)
- Bump bonds

The pixel chips which can be thinned down to 150 μm and the sensor are optimised separately and connected via bump bonds.

Each pixel cell of the sensor is connected to a corresponding cell in the readout chip via a bump bond. The pixel cell in the readout chip registers the resulting signal produced by a traversing particle. In Fig. 2.9 the basic principle of a hybrid pixel detector can be seen.

Hybrid pixel detectors are radiation hard up to several tens of Mrad. Similar to micro-strip detectors the sensor has usually a thickness between 200 - 300 μm which gives 2.1×10^4 - 3.2×10^4 e⁻h⁺-pairs. The complex flip chip bonding technology, the material budget (sensor and chip) and the high production cost limits the range of applications of hybrid pixel detector [32].

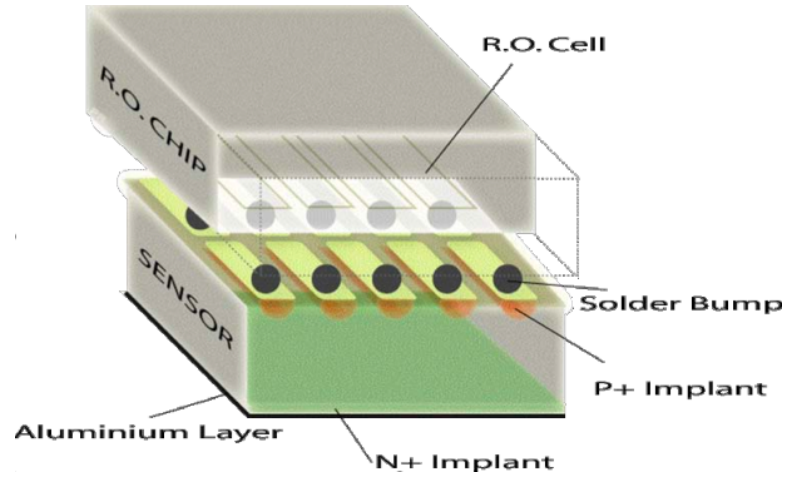


Figure 2.8: Layout of a hybrid silicon pixel detector [32].

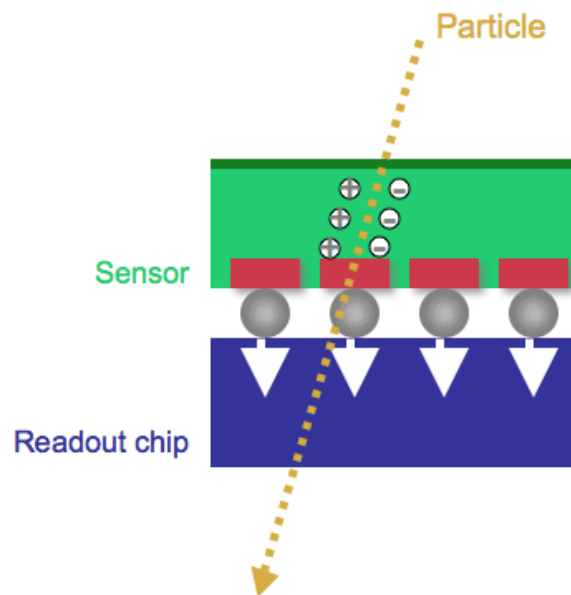


Figure 2.9: In the sensor cell a signal is produced by the traversing particle and read out by the corresponding cell in the readout chip [32].

Monolithic Silicon Pixel Detector

First prototypes of monolithic silicon detectors were built in the 1990s. The principle is that the radiation detection is done inside the CMOS circuitry (Fig. 2.10). In a p-type low resistivity silicon n-type charge collectors are integrated. The signal is created in an epitaxial layer with a thickness $\sim 10 \mu\text{m}$ and collected by diffusion. The aim is to get a low mass high granular silicon pixel detector without an interconnection to a sensor [32].

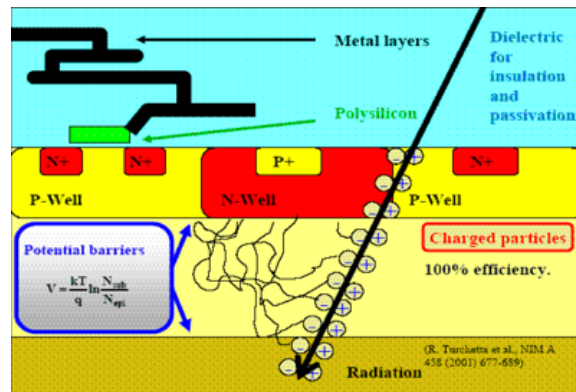


Figure 2.10: Monolithic pixel detector [32].

The advantages are a compact and thin ($< 30 \mu\text{m}$) design, a small read-out pitch and that no interconnections like bump bonds are needed. But the signal produced by diffusion is small. Monolithic Pixel Detectors are also less radiation hard compared to Hybrid Pixel Detectors. The Monolithic Pixel Detector is still under development and would be an interesting technique for future applications [32].

2.2.4 Silicon Drift Detector

The principle of Silicon Drift Detectors (SDD) is based on creating a drift field parallel to the wafer surface. The sensitive area is split into two drift regions by the high voltage cathode. p^+ cathode strips fully deplete the detector volume. Fig. 2.11 shows the layout of a ALICE SDD module.

The potential inside the wafer has a parabolic form with a minimum at the central dividing plan [29]. Electrons which are created at some point in the wafer drift along the longitudinal component of the E-field to the central cathode. Measuring this drift time gives information similar to gas drift detectors.

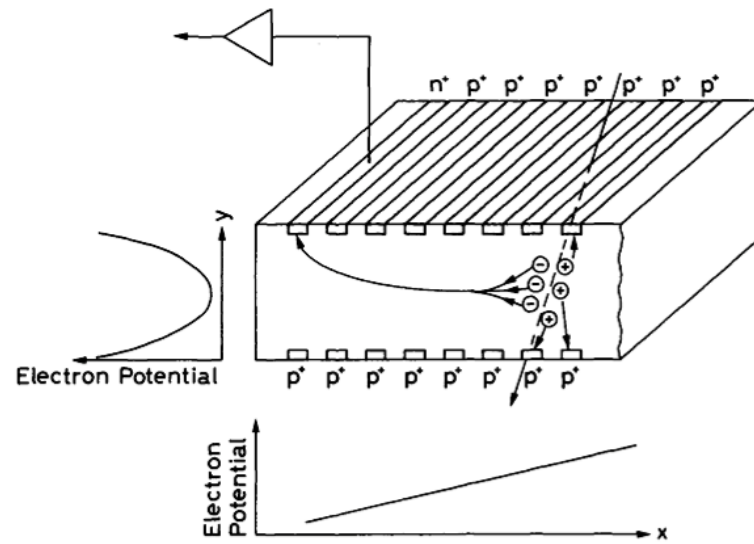


Figure 2.11: Operating principle of a silicon drift detector [33].

Chapter 3

Component Test - Quality Measurements

In the first section of this chapter a detailed description of the ALICE pixel detector is given. Further the test procedures and measurements of the different production states of the SPD are described and the test results are presented.

3.1 The Components of the ALICE SPD

The SPD consists of 10 sectors divided into two half-barrels. Each module of these 10 sectors underwent several tests throughout the production in order to guarantee the full functionality. In the following sections a detailed description of the different SPD components is presented.

3.1.1 Half-Barrel

The SPD is made of two half-barrels each consisting of five sectors. The mechanic support structure of each sector is made of Carbon Fibre (CF) to comply with the material budget constrains. The entire detector is housed inside a carbon fibre shell. Each half-barrel is tested individually in a clean-room with the complete electronic read-out chain, the final power supplies and cables and the cooling plant as it will be used in the ALICE experiment. During the test phase each sector was associated with a number corresponding to the production state. These numbers differ from the sec-

tor numbering in the SPD. Fig. 3.1 shows the conversion between sector test (outer numbers) and position in the SPD (inner numbers) seen from side A¹. In the following text the two Half-barrels are referred to *HB1* for Half-barrel 1 (Sector 0 to 4) and *HB2* for Half-barrel 2 (Sector 5 to 9).

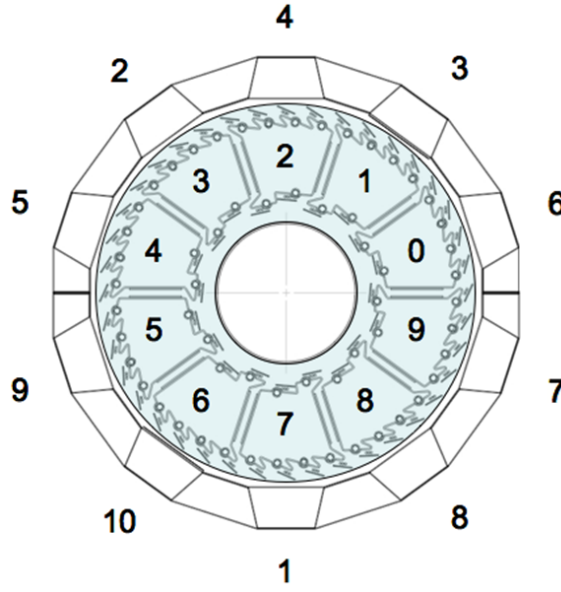


Figure 3.1: Schematic view of both half-barrels. The outer numbers corresponds to the production state. The inner numbers give the position after assembling of the two half-barrels.

3.1.2 Sector

Due to the tight requirements concerning the thickness of the detector a special carbon fiber (CF) structure was developed with $200\ \mu\text{m}$ thickness to form the mechanical support of the SPD. This CF support is divided into 10 sectors. Cooling tubes made of PHYNOX (Co-Cr-Ni alloy) with 1 mm diameter and $40\ \mu\text{m}$ wall thickness are embedded in the CF structure. On every sector four detector modules (half-staves) are mounted to form the inner and eight detector modules to form the outer barrel. In order to avoid dead areas a turbine shaped configuration in the outer barrel was chosen which leads to a higher material budget in some regions of the detector. Fig. 3.2 shows the half-stave numbering for one half sector [25].

¹The side of the detector refers to the circulation of the particles in the accelerator. One beam will circulate clockwise corresponding to side C, one will circulate anti-clockwise corresponding to side A.

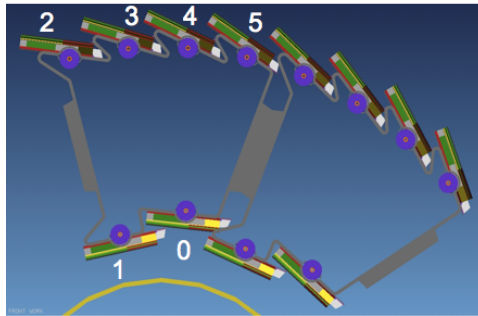


Figure 3.2: Numbering of the half-staves seen from side A.

3.1.3 Half-Stave

The basic detector module is the half-stave (HS), which consists of one multi-chip-module (MCM) and two bumpbonded sensor ladders glued on a flexible multi-layer aluminum/polyamid laminate carrying power, control and signal lines [34]. The connections between the Pixel Bus, readout chip and the MCM are carried out via ultra-sonic wire-bonding using 10×103 (32 data lines, 71 lines for control, test and power purpose) aluminium wire bonds of $25 \mu\text{m}$ diameter. The edge of the pixel bus is connected to the MCM, which controls the entire communication from and to the off-detector electronic. Finally, a $12 \mu\text{m}$ thin grounding foil of aluminium deposited on kapton, which is glued between the carbon fibre and the readout chip, completes the layout of the half-stave.

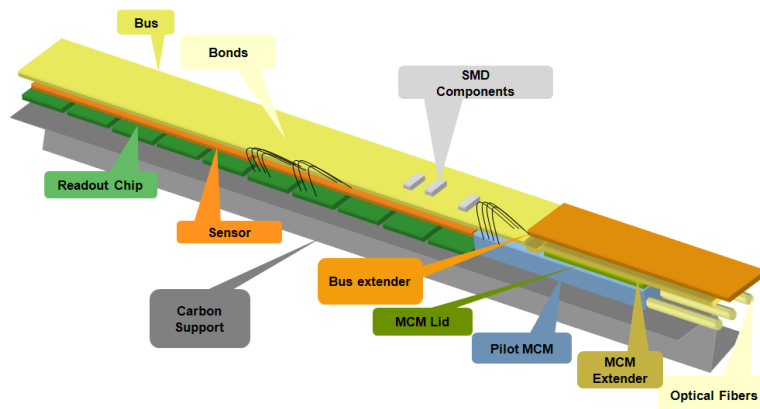


Figure 3.3: Scheme of a half-stave - the three fibers on the right side are the data, serial and clock line.

Fig. 3.3 shows the scheme of a half-stave. Two copper/polyamide laminates are connected to the pixel bus and the MCM to provide power to the readout electronics and the sensors. Each half-stave is supplied with

1.85 V/ 5 A for the Bus and 2.6 V/ 0.5 A for the MCM, respectively [35], [34].

The ALICE detector concept relies on the low material budget of the Silicon Pixel Detector. Therefore, the materials used are as thin as possible using wherever possible light-weight materials. As a result the ALICE SPD has a material budget of 1.14% X_0 per layer which is the lowest value for pixel detectors at the LHC. Table 3.1 shows type, thickness and radiation length of each part of the detector along a radial particle trajectory in the active area.

SPD Element	Thickness [μm]
<i>Pixel Bus</i>	
2 Al layers (LV power / ground)	100
3 Al layers (data / control)	15 – 30
Glue (7 layers)	35 - 70
Polyamide (5 layers)	60
Total bus	210 – 260
<i>Other Componets</i>	
Pixel chip	150
Sensor	200
Solder bumps	20
Grounding foil (Kapton/Al)	25 + 50
Thermal grease	150
Carbon fiber	200
Total Components	745 – 770

Table 3.1: Material Budget of one SPD Layer [14].

Ladders

One sensor ladder consists of five ALICE pixel chips which are flip-chip bonded to one p-in-n sensor (see Fig. 3.4). The flip-chip bonding is carried out at VTT² using Pb-Sn bump bonds of $\sim 25 \mu\text{m}$ diameter [25].

ALICE Pixel Readout Chip

The ALICE1LHCB pixel readout chip is a mixed signal ASIC developed in a commercial $0.25 \mu\text{m}$ CMOS process and is radiation hardened by design

²VTT Center for Microelectronics, Espoo, Finland, <http://www.vtt.fi/index.jsp>

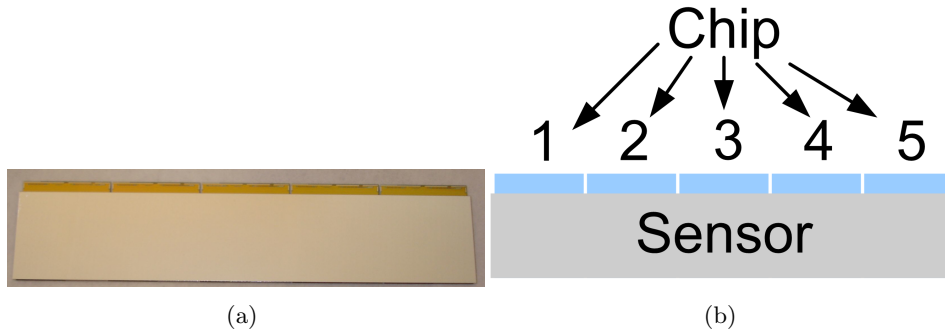


Figure 3.4: Picture (a) and Layout (b) of a sensor ladder. [36]

layout techniques. Each chip with a size of $13.5 \text{ mm} \times 15.8 \text{ mm}$ includes the internal DACs, the JTAG part, the chip controller part and the wire bonding pads. The 8,192 readout cells of $50 \mu\text{m} \times 425 \mu\text{m}$ are arranged in 32 columns and 256 rows. Each readout cell is connected via bump bonds to a sensor cell. The 32 columns are read out sequentially at a frequency of 10 MHz. The control of the acquisition readout is performed via dedicated signal lines. The configuration of the pixel chip is performed via a JTAG circuitry with two input lines on each chip for redundancy in the JTAG chain (Fig. 3.5). In case of a faulty chip the configuration data can be bypassed to the subsequent chip. Fig. 3.6 shows a block diagram of a pixel cell [25], [37].

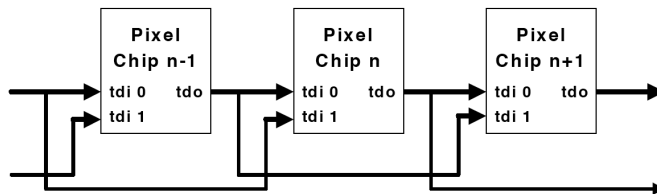


Figure 3.5: The tdi/tfo interconnections between the pixel chips [37].

Between the pixel matrix and the I/O pads for the contacts of the wire bonds, 42 8-bit digital analog converts (DAC) are located. The DACs provide globally the voltage and current references to the analog front-end and the currents starved logic of each pixel cell. The DACs as well as the pixel matrix are controlled via the serial interface following the IEEE JTAG standard [36].

A special feature of the ALICE SPD is the FastOr signal. Whenever a pulse above the threshold is produced by a hit it will trigger a FastOr signal. This signal is produced after the threshold discrimination and sent to the off-

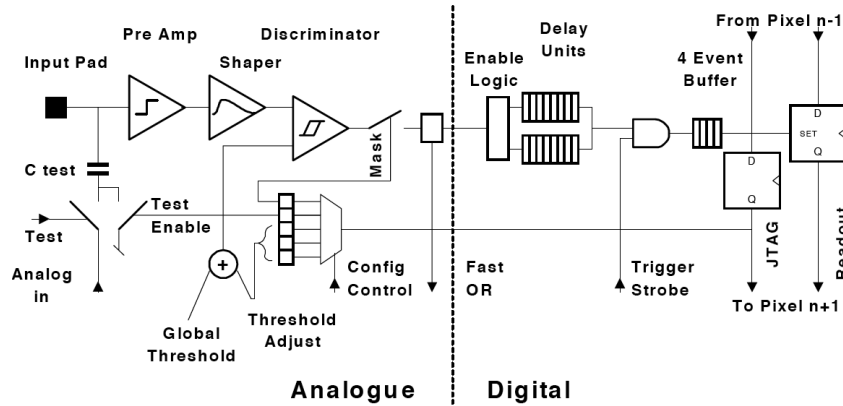


Figure 3.6: Block diagram of a pixel cell [37].

detector electronics without further processing in the readout cells allowing a fast response. The individual cells are ORed together to generate one FastOr pulse for each chip. Thus, the SPD can provide 1,200 independent FastOr signals to the L0 trigger decision (800 from the outer and 400 from the inner layer) [36].

Pixel Sensors

The pixel sensors (Fig. 3.7) have an active size of $70.7 \text{ mm} \times 12.8 \text{ mm}$. They are produced on 5" high resistivity n-type silicon wafers of $200 \mu\text{m}$ thickness to comply with the material budget constraints. The sensors contain a pixel matrix of $5 \times (32 \times 256)$ pixel cells of $50 \mu\text{m} \times 425 \mu\text{m}$ elongated to $625 \mu\text{m}$ at the junctions between two chips [25].

Multi-Chip-Module

A Multi-Chip-Module (MCM) is located at the outer end of each half-stave. It houses the readout and control electronics and consists of four ASICs which are mounted as bare dies for space constraints: the ANAPIL chip provides reference voltages to the 10 pixel chips and contains an ADC for monitoring the currents and voltages. The DIGITAL PILOT transmits the signals and configuration data to the router module located in the control room and provides timing, control and readout for the half-stave. The GOL (Gigabit Optical Link) serializes the data and the RX40 acts as a receiver for the PIN diodes in the optical module. The latter is a custom designed optical transceiver housed in a silicon package and contains two PIN diodes and one

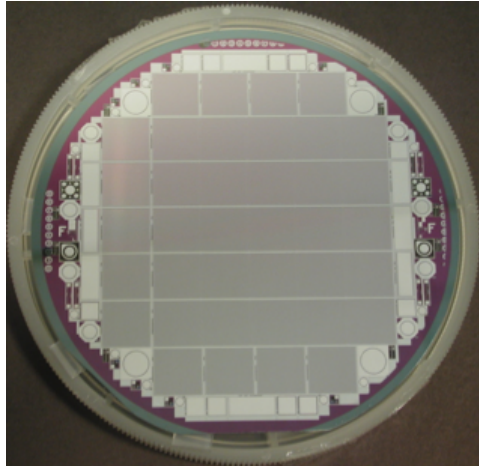


Figure 3.7: The 5" sensor wafer. The picture shows the front side of the sensor with large pixel sensors in the center of the wafer. Different test structures and single chip sensors are placed around the sensor edge.

laser diode. The module is extremely compact with a size of $116 \text{ mm} \times 6 \text{ mm}$ and a thickness of 1.2 mm and has bond pads for electrical connections. Due to the space constraints, the implementation of stress relief on the fibre pigtails is limited, which, therefore, requires a careful handling of the fibre optics. The MCM carries the reference analog voltages with an accuracy of 10 mV and digital data streams at speeds of 800 Mbits/s without any observable cross-talk effects. The incoming 40 Mb/s clock is recovered with a maximum jitter of 42 ps allowing proper functionality of the 800 Mbits/s G-Link. The jitter on the 800 Mbit/s stream is as low as 11 ps . The optical noise margin for the incoming and outgoing data is higher than 14 and 9 dB , respectively, and is adequate to compensate for radiation effects and aging. Fig 3.8 shows a picture of a MCM [25], [34].

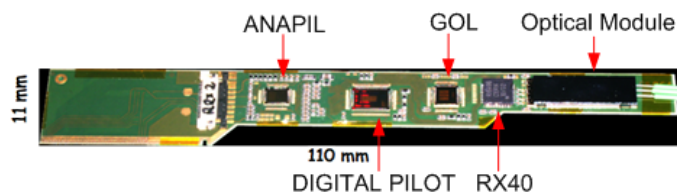


Figure 3.8: Multi-Chip-Module.

Pixel Bus

The 250 μm thick aluminum/polyamide laminate (Pixel-Bus) provides the connection between the 10 chips and the MCM (Fig. 3.9). It consists of five Al-layers, two for the power supply and three for the signal routing, separated by a polyamide foil. Each subsequent layer is 500 μm shorter than the layer below in order to make it accessible for wire bonds. In total approximately 1,000 wire bonds are used on each half-stave. The connection of the three aluminium signal layers is carried out with 'plated-through' holes (microvias). Fig. 3.10 shows a SEM picture of a microvia between the first two layers.

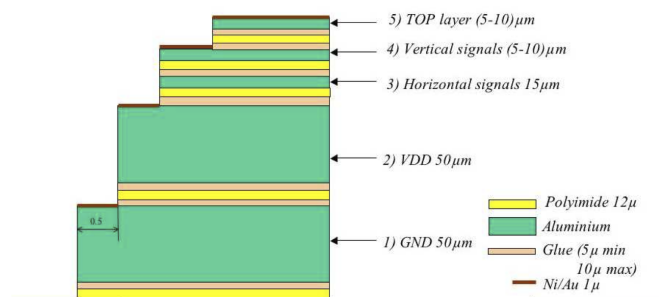


Figure 3.9: Cross section through a half-stave. The picture shows the different layers of the half-stave.

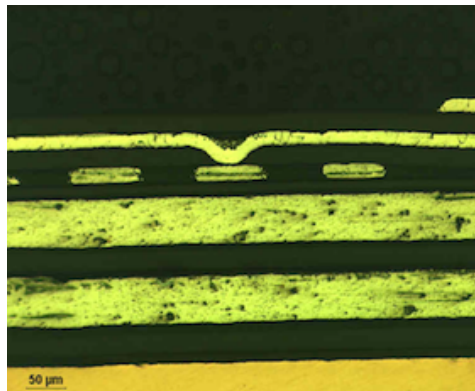


Figure 3.10: SEM picture of an Al-microvia.

3.2 Test Setup, Measurements and Results

The construction of the ALICE SPD requires many testing steps during the production process. Each of the components are qualified in several steps

before they are assembled to finally build a half-barrel. In this section a description of the different test procedures, the quality criteria and their results for the SPD are presented. In this work, a series of tests on a subset of ladders are performed in order to verify the production quality of these ladders. The results of the complete ladder production of the SPD is presented later in this section. One special emphasis in this work is laid on the long term operability of the half-staves in the experiment. A thermal cycling study is carried out to verify the long term reliability of the metallic interconnections present on the half-staves.

3.2.1 The Ladder Test System



Figure 3.11: The SÜSS probe station at CERN. The probe card is connected via cables J1 + J2 to the DAQ adapter board. The voltage supply to the chip is provided via the DAQ adapter board. The bias voltage is supplied via a needle which is connected to the back-side of the sensor [36].

The test setup for the ladder testing is based on LabView and VME and includes a Karl Süß³ probe station and CCD camera connected to a microscope used for the visual inspection of the ladder. For the voltage supply a Gossen⁴ (chip) and a Keithley⁵ (sensor bias voltage) power supply is used. The connection of the readout chip to the test system is carried out via a custom made probe card. A detailed description of the test procedures can be found in [36]. Fig. 3.11 shows an image of the probe station used at CERN. The following list shows the individual steps of the test procedure:

- A visual inspection of the sensor back-side of each ladder is carried

³SÜSS MicroTec AG, Garching, Germany, <http://www.suss.com>

⁴Gossen-Metrawatt GmbH, Nürberg, Germany, <http://www.gossenmetrawatt.com>

⁵Keithley Instruments Inc., Cleveland, Ohio, <http://www.keithley.com>

out

- Measurement of the analog and digital current [mA]
- JTAG functionality test (passed/ not passed)
- Internal DAC functionality
- Measurement of the mean minimum threshold and rms
- Mean noise and rms
- FastOr signal threshold is determined
- Radioactive source test
- Leakage current measurement up to 100 V

Table 3.2 gives a summary of the classification criteria of the ladders. Only class I ladders are used for half-stave assembly. The leakage current measured at the end of a ladder test can only give an indication of the sensor quality since only one chip is connected with the probe card at the time. Therefore, only the leakage current of the sensor area close to the contacted chip is measured and not of the complete sensor. This can only be done when all five chips on a ladder are simultaneously powered which is only possible after the half-stave assembly.

Measurements and Results

Until now 439 ladders have been tested. 343 meet class I requirements, 28 class II and 68 class III (Fig. 3.12). Of the 264 ladders mounted on the 11 sectors - 10 are assembled in the detector, 1 sector remains for testing - there are $\sim 0.77\%$ non working pixels. Fig. 3.13 shows the amount of non working pixels, which is the sum of noisy and dead pixels. Noisy pixels are channels which always send a signal regardless of what threshold is set. Those pixels are software-wise masked and appear as non working (dead) pixels in the analysis.

Ladders, which were rejected due to defects in one or two chips, have been chosen for rework at the bonding facility. Those ladders were retested and were again classified. This also increased the yield of class I ladders.

Class I Used for HS mounting	Class II backup for HS mounting	Class III not used for HS
JTAG test passed.	JTAG test passed.	JTAG test failed.
$I_{\text{anlague}} \leq 350 \text{ mA}$	$I_{\text{anlague}} \leq 350 \text{ mA}$	$I_{\text{anlague}} \geq 350 \text{ mA}$
$I_{\text{digital}} \leq 270 \text{ mA}$	$I_{\text{digital}} \leq 270 \text{ mA}$	$I_{\text{digital}} \geq 270 \text{ mA}$
Minimum threshold exists	Minimum threshold exists	Minimum threshold does not exist
FastOr min. threshold exists	FastOr min. threshold exists	FastOr min. threshold does not exist
Mean threshold is less than 50 mV ($\sim 3000 e^-$)	Mean threshold is less than 50 mV ($\sim 3000 e^-$)	Mean threshold $\geq 50 \text{ mV}$
Noisy Pixel can be masked	Noisy Pixel can be masked	Noisy Pixel cannot be masked
Less than 1% defect pixels in threshold scan and source test	More than 1% but less than 3% defect pixels in threshold scan and source test	More than 3 % defect pixels in threshold scan and source test
Leakage current stable and $\leq 2 \mu\text{A}$ @ 50 V	Leakage current stable and $\geq 2 \mu\text{A}$ and $\leq 5 \mu\text{A}$ @ 50 V	Leakage current not stable and $\geq 5 \mu\text{A}$ @ 50 V

Table 3.2: Classification criteria for the ALICE SPD ladders [36].

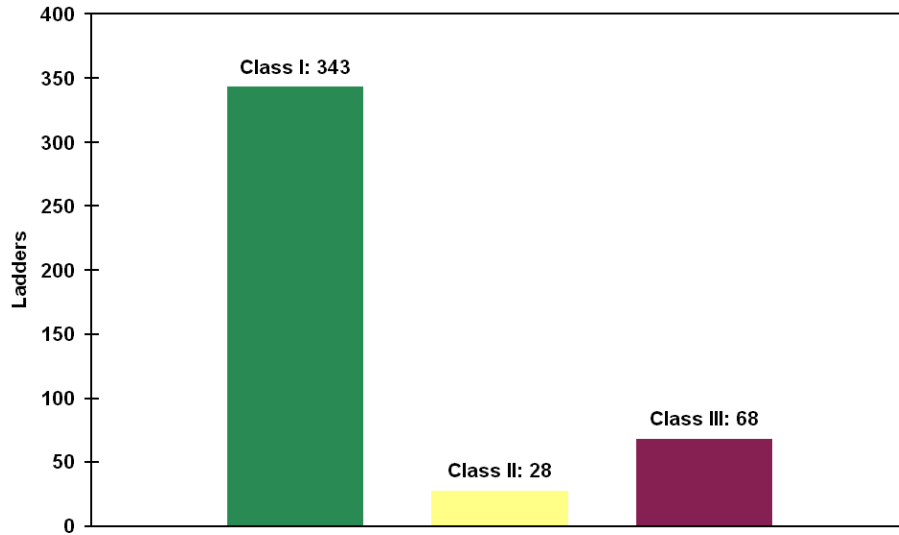


Figure 3.12: Yield of the ladder production.

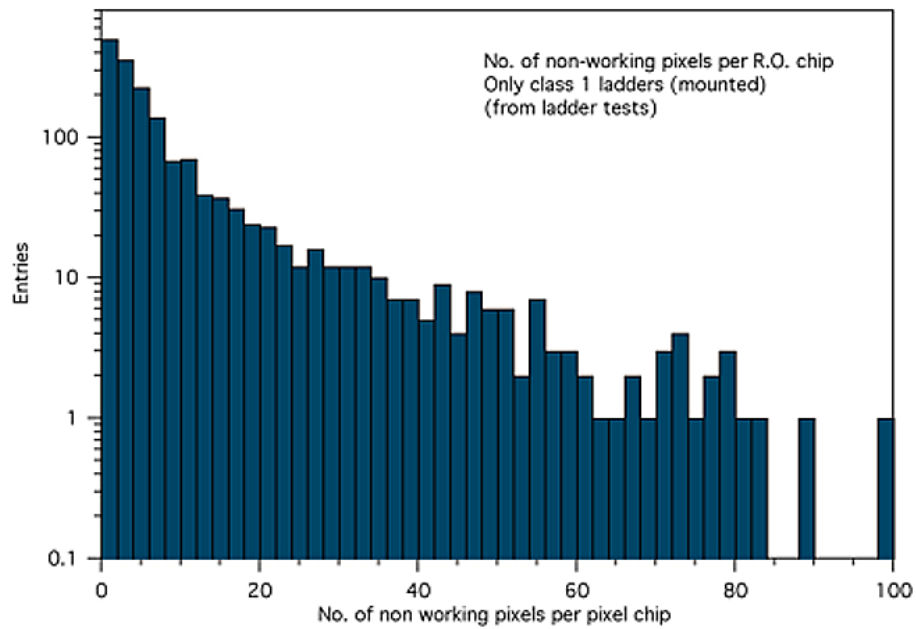


Figure 3.13: Number of non working pixels per chip. Only ladders with less than 1 % of non working pixels are used. [38]

3.2.2 Half-Stave Tests

All half-staves are assembled in Bari (Italy) and tested in Bari and in Padova (Italy) before mounting on the sectors, respectively. The half-stave tests after sector mounting are carried out at CERN in a cleanroom using the complete electronic read-out chain, the final power supplies and cables as foreseen in the ALICE experiment. In the following sections a short description of the data acquisition and detector control system is given.

Test procedures

The individual steps of the test procedure are listed below:

- Leakage current measurement from 5 V to 100 V: the leakage current is measured for both ladders of a HS simultaneously giving one value per set voltage for both sensors. The leakage current is verified to be stable over time.
- Measurement of the temperature with both Pt1000 chains: two chains consisting of five Pt1000 elements each are used to measure the temperature of the HS.
- Uniformity scan of the pixel matrix.
- Measurement of the minimum threshold.
- Radioactive source test with a Sr90 source: The L1 and L2 trigger signals are generated using the FastOr signal. The resulting hit map is saved and analysed giving the positions of non-working pixels (dead, in-, overefficient or noisy).
- Evaluation of noisy and dead pixels.

Further, current and voltage of the MCM and bus are monitored during the tests. The different DAC values are adjusted and optimized during the measurements. Finally, the measured values are stored in a configuration file which is uploaded into the configuration database for later use in the sector and half-barrel tests.

Data Acquisition and Detector Control

The SPD data acquisition system, which is controlled by the ALICE Data Acquisition and Test Environment (*DATE*) software, consists of two *Local Data Collectors* (LDC), each reading 10 *Detector Data Links* (DDL). The data received by the LDCs are merged together forming a sub-event in the *Global Data Collector* (GDC).

The SPD Detector Control System (DCS) consists of two software tiers: The bottom tier is based on the commercial SCADA (Supervisory Control And Data Acquisition) software *PVSS*⁶. SCADA is a computer system that control and monitor technical processes e.g. power generation, fabrication. The *Front End Device* (FED) server is a communication layer between PVSS and the hardware. It accepts complex macro instructions for configuration and control operations of the hardware. It is also responsible for the inter-connection with the configuration database.

The upper tier of the DCS software is build by the *Finite State Machine* (FSM) which is based on the *State Machine Interface*⁷ (*SMI++*). The FSM serves as the logical connection between the SPD subsystems and is the interface with the global ALICE DCS and the *Experimental Control System* (ECS). Fig. 3.14 shows the structure of the DAQ system.

PVSS protects the detector system via control scripts, which are implemented to identify alarm states of the various system parts and it also provides state information for the FSM. The SPD DCS is also used for the detector calibration procedures. The data produced in several steps of the calibration procedure is retrieved by the DCS itself or by the *SPD DAQ*, which also analyses the used detector configuration parameters. Further, PVSS also provides a fully graphical interface for monitoring and controlling the power supplies and cooling system.

For these tests the data is viewed with the custom designed software *SPD Monitoring Online Data* (SPDMOOD). The analysis of the data is performed by a program called *Detector Algorithm* (DA) and then displayed via a software called *Reference Data Display*. As an example Fig. 3.15 shows a screenshot of the SPDMOOD and the Reference Data Display. Fig. 3.15a shows the uniformity scan of an half sector. Each line of the displayed matrix corresponds to a half-stave (0 to 5), whereas each column correspond to the chips (0 to 9) of the half-stave. The red column on chip 8 of half-stave 0 indicates a malfunction of this chips. In fig. 3.15b one can see the mul-

⁶ETM professional control GmbH, Eisenstadt, Austria, <http://www.pvss.com>

⁷<http://smi.web.cern.ch/smi/>

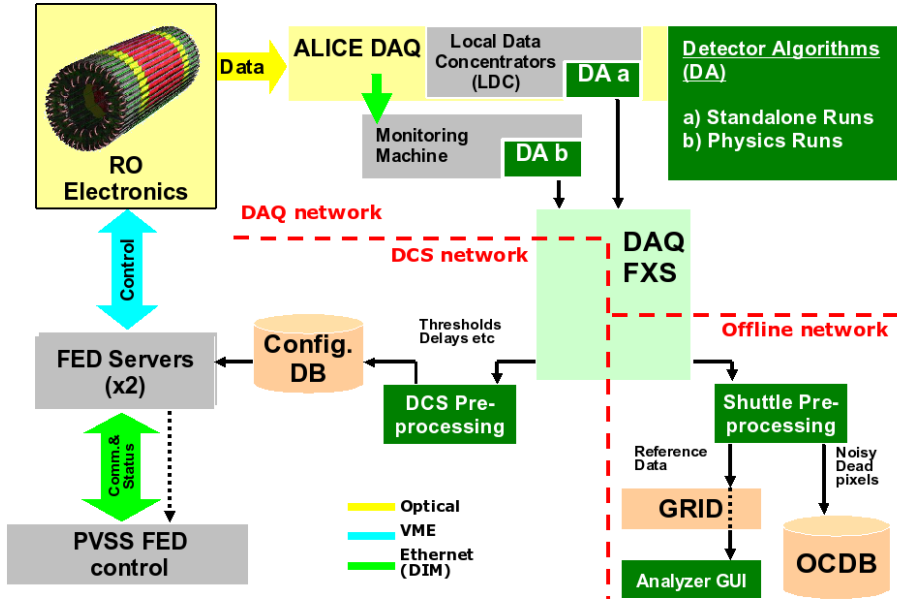


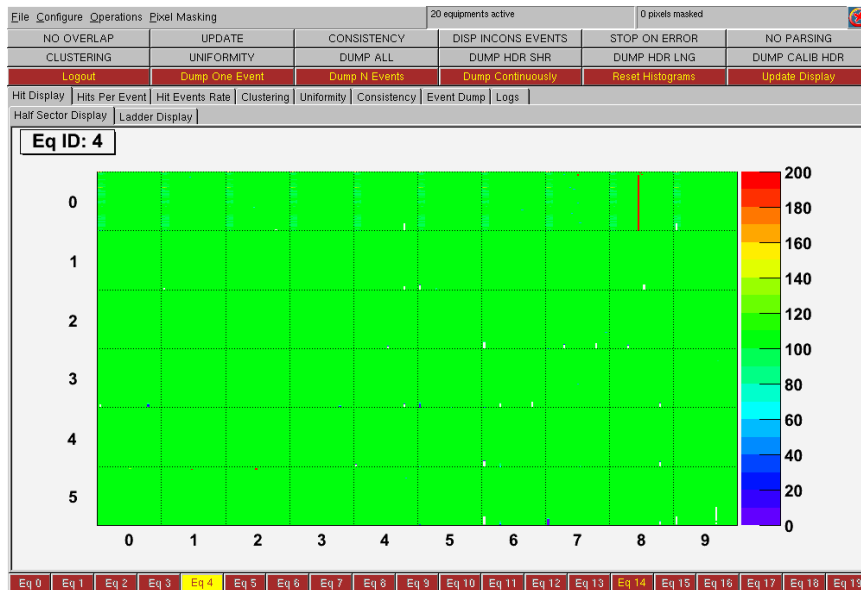
Figure 3.14: Structure of the DAQ and DCS system [38].

tiplicity plot of one half-stave. The Detector Algorithm software analyzes the data of the minimum threshold scan and displays it using the Reference Data Display. The measured values are stored in a database and can also be accessed over this program (more details about uniformity scan and minimum threshold one can find in this section below 3.2.2).

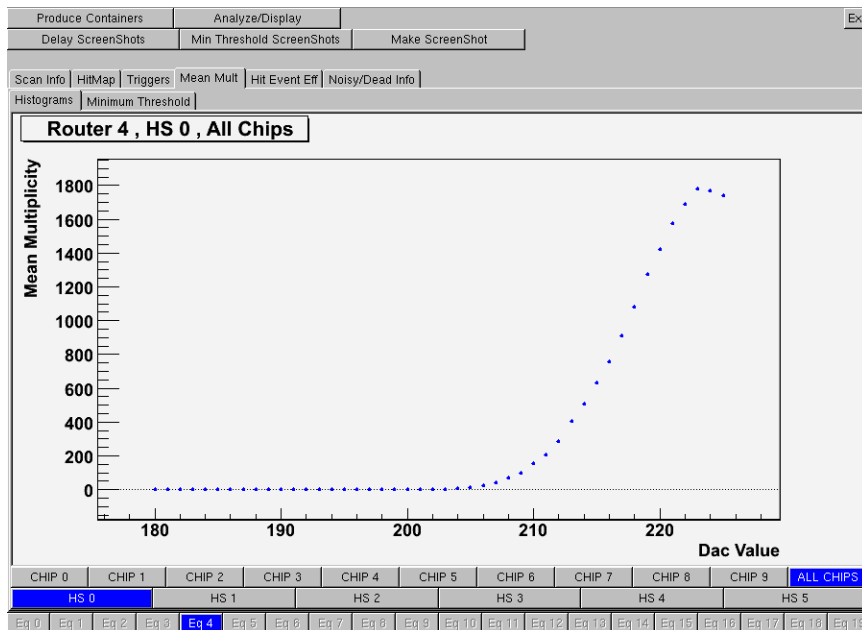
Router and Link Receiver

20 *Router* modules (Fig. 3.16), each carrying three 2-channel *Link Receiver* cards, provide the interface between the on-detector electronics and the DAQ. The router has six channels in order to connect all the optical links for the operation of one half of a sector. Each channel consists of three optical fibre links, one for receiving the data and two for transmission of clock, control and configuration signals. The router processes the data from the detector and sends it to the ALICE DAQ via DDL. Further, it provides monitoring for the *Pilot Chip Readout State Machine* and for data errors. The routers contributes to the temperature interlock by controlling the second Pt1000 chain.

In the Link Receiver the pixel data stream is de-serialized, the received data is checked for format errors and stored in a FIFO for subsequent hit encoding. After, the data is zero-suppressed, encoded, reformatted and writ-



(a) The picture shows a scan of a half-sector using a test pulse (uniformity scan). With the selector on the bottom part, one can change the view to another activated half-sector.



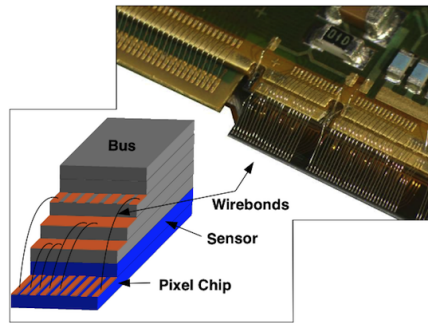
(b) The graph shows a multiplicity plot used to determine the chip minimum threshold of one half-stave. The write DAC value is where the graph starts to rise.

Figure 3.15: Two screen-shots of the Graphical User Interface of the SPDMOOD and Reference Data Display.

ten in the dual port memory of the link receiver. When all data belonging to one event is stored in the dual memory, the Link Receiver provides an event ready flag for the router processor. The Link Receiver confirms the error flag, that is identified in the data stream coming from the detector.



(a) SPD Router card with three Link Receiver.



(b) This picture shows wire bonds which connect the readout chip to the bus. Araldit is used for protection [14].

Figure 3.16: Picture of router and wire bonds.

Measurements and Results

As mentioned before the half-stave consists of two ladders glued on the pixel bus. After wire bonding (Fig. 3.16) extensive tests are conducted to ensure the full functionality of the half-staves. One test is the measurement of the leakage current. The operation voltage of the sensor is 50 volts and the current is required to be stable in time. Fig. 3.17 shows the leakage current characteristics of a half-stave.

Another important parameter is the temperature which is continuously monitored during the operation of the half-stave. While the temperature of the MCM stays around room temperature, the temperature of the ladders and pixel bus increase over $60\text{ }^{\circ}\text{C}$ without cooling. At this temperature the glue which is used for the assembling softens and the stability of the half-stave is not guaranteed anymore. For this reason a sophisticated cooling system is used for the SPD. For half-stave tests a fan which cools the support of the half-stave is sufficiently enough although a good thermal contact using thermal grease is very important. A temperature over $40\text{ }^{\circ}\text{C}$ on the pixel bus would indicate a bad thermal contact. As a reference system a thermal camera is used to double check the reading of the Pt1000 chains (Fig. 3.18).

After the basic tests, calibration runs are carried out in order to evaluate the configuration settings and the full functionality of the half-stave. First

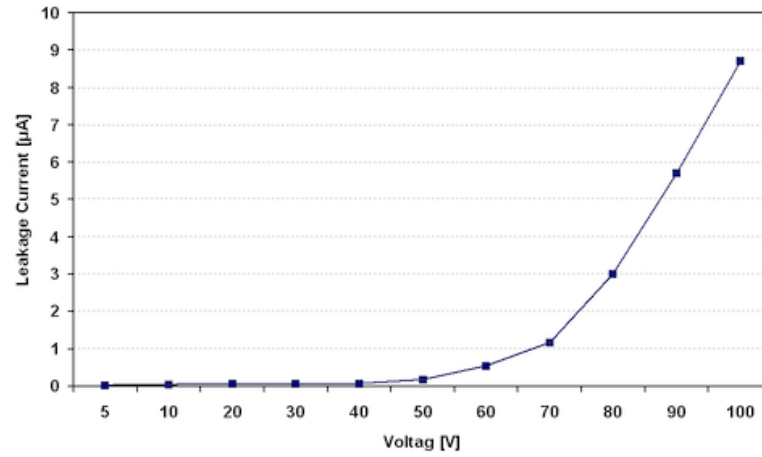


Figure 3.17: Leakage current of HS149R. After integration of the ladders into the half-stave the leakage current is measured for both ladders.

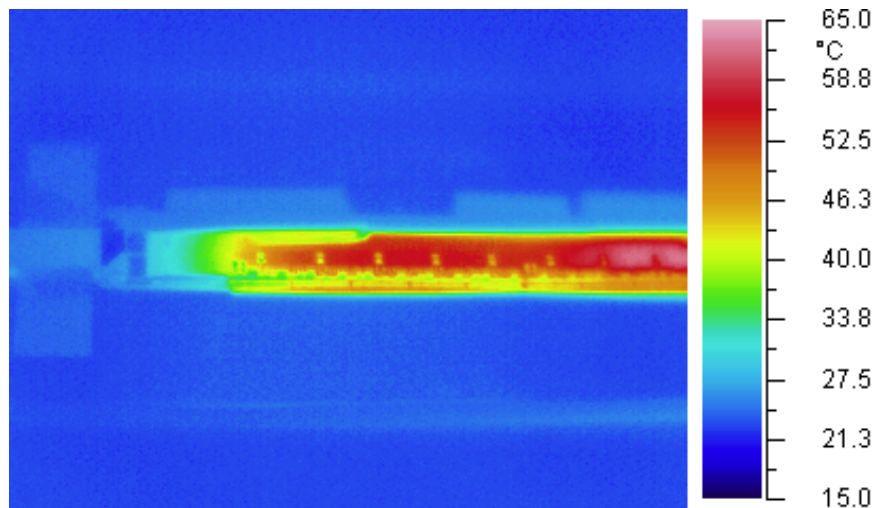


Figure 3.18: Picture of a HS powered-on taken with a thermal camera. The different colors indicate the temperature distribution over the half-stave.

the minimum threshold for all chips is measured. The lowest DAC value (highest efficiency), at which the chips are still operating noise free, is used for all further tests. Fig. 3.19 shows the analysis of the minimum threshold scan of HS149R.

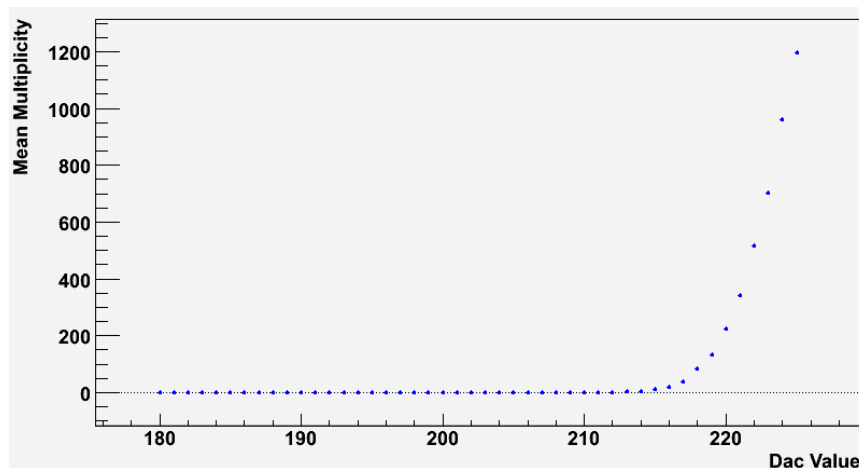


Figure 3.19: The minimum threshold is analyzed using the reference data display.

The uniformity scan at minimum threshold is carried out by sending a test pulse to the readout chip. It gives information about dead or noisy channels in the readout. Before the scan the right strobe delay has to be adjusted in order to read back the 100 pulses sent to each pixel. Fig. 3.20 shows uniformity scan of one half-stave. The dead columns on some chips indicate test columns which only appear in the test pulse scan.

Finally, a source test using the FastOr trigger signal is processed (Fig. 3.21). Only this test gives information about missing or broken bump bonds and about noisy pixels which appeared to be silent in the previous run. On the picture can be observed that the chips 2 to 8 have less hits in their lower part. This is due to the low activity of the source. The radiation is reduced by the aluminum clamp which are situated on the lower part of these chips in order to hold the half-stave on the support. It can be seen that chip 3 has a higher amount of hits which is caused by the manual movement of the source over the half-stave. Fig. 3.22 shows the matrix of a pixel chip in detail. The axis represents the rows and columns of a pixel chip. A non working pixel determined in a source test appears as white spot on the matrix. The detector algorithm analyzes the data from the source test and stores the coordinates of the non working pixels in the database and displays it over the SPDMOOD software.

The half-stave tests are important for the integration of the module into

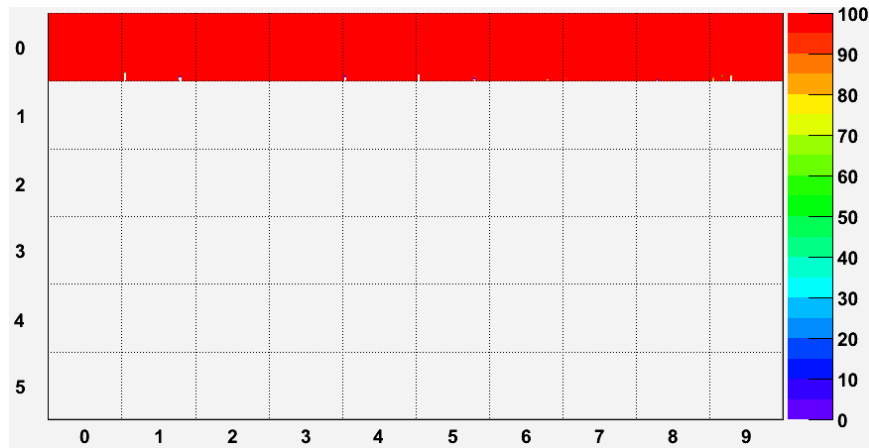


Figure 3.20: Scan with a test pulse at minimum threshold of one half-stave. The GUI displays a complete half-sector with one half-stave activated. 100 pulses are sent to each pixel. Thus, a proper working pixel shows 100 hits in this test. If the half-stave has no dead pixels, the result is displayed as a uniform (red) matrix.

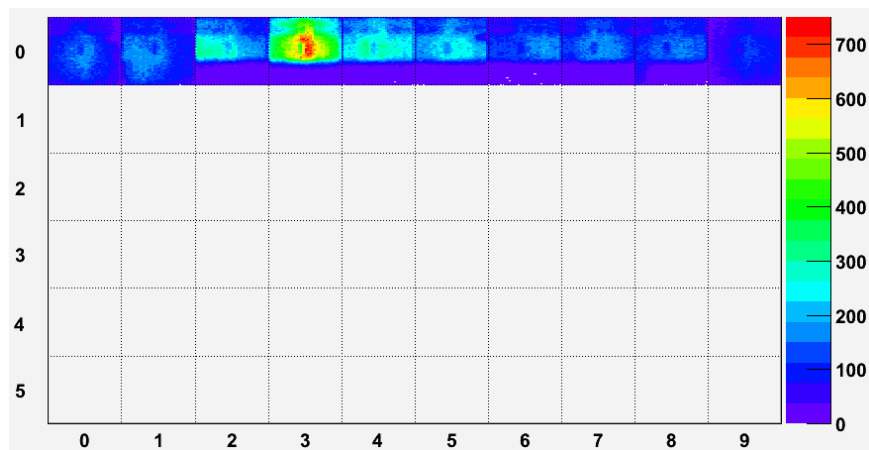


Figure 3.21: For the source test a Sr^{90} is used. Due to manually moving the source over the half-staves the irradiation is not homogeneous. But one can see some non-working pixels (white spots) in the chips 1, 4, 5, 6 and 8. The color code on the right side gives the amount of particles hit one pixel. Red is always the highest amount of hits. Thus, the spectrum is rescaled the hits a pixel received.

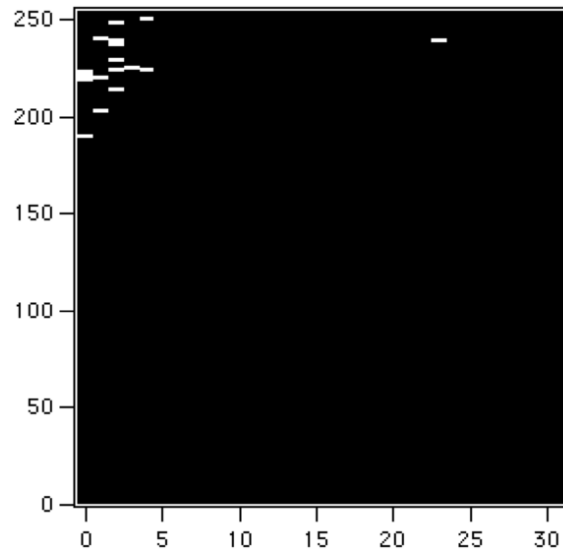


Figure 3.22: The picture shows the matrix of a pixel chip. The axis represents the 256 rows and 32 columns, respectively. The white spots are non working pixels. Thus, the coordinates of a non working pixel can be directly determined from picture.

a sector. Further, the retrieved data is used as a reference for the sector tests later. The found calibration values are stored in a configuration file and uploaded into the configuration database.

3.2.3 Aging Tests

Three different tests can be performed to verify the integrity of electronic components: *Intermetallic tests*, *humidity test*, *cycling test*. In the following the different tests are presented in detail.

Intermetallic Test

Temperature cycle profiles at various stress levels are employed to evaluate the effect of stress and to detect unknown failures. A temperature profile can be defined by

- High extreme temperature T_{\max} ,
- Low extreme temperature T_{\min} ,

- Temperature change $\Delta T = T_{\max} - T_{\min}$,
- Ramp rates,
- Dwell times at extreme temperatures

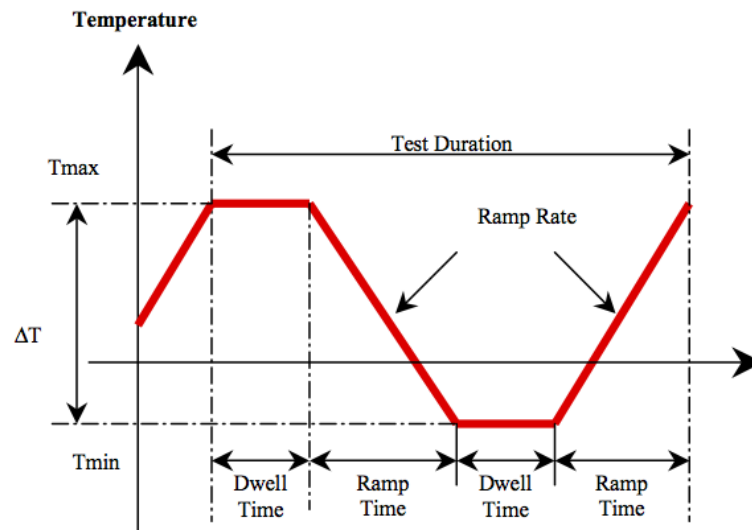


Figure 3.23: The Schema shows a temperature cycling profile [39].

The larger T_{\max} , ΔT , dwell time and ramp rate are the higher is the stress level for the components. Temperature cycling tests are used in industry to characterize the product capability and to detect unknown failure modes. They are important to qualify connections between different metals [39]. A temperature cycling profile is shown in Fig. 3.23. In the SPD there are different intermetallic connections: between readout chip (Al) and bump bond (Pb) and between MCM (Al) and Bus (Cu). Tests would be interesting for characterizing the long-term reliability of the detector. But due to the limited temperature which can be applied on the optical package ($\leq 50^\circ\text{C}$) it is not possible to carry out such tests in a realistic time frame [40]. At this temperature limit it would need 1 1/2 years of cycling to reach the total life expectancy of the detector. With a temperature of $\leq 100^\circ\text{C}$ the total life expectancy of the detector would be reached only be 30 hours.

Humidity Test

Sometimes detectors are operated at temperatures below the dew point. If the electronics is not fully encapsulated, moisture can cause problems on the electronics. However, the SPD is operated at around 30°C and humidity

and the temperature is controlled by the ALICE experiment. Therefore, moisture is not considered to be a problem [40].

Cycling Test

To test the mechanical stress of the components during the entire operating time of the SPD a number of cycles representing the turn on and off of the detector system are processed. The amount of turn on/off are estimated to be between 200 and 300 times over the 10 years of operation [40]. The tests are conducted with a chip assembled on a test card, an assembly (chip + sensor) and on a half stave. All three components are cycled in a heating chamber between 15 °C and 45 °C. After 50 cycles a complete functionality test of the components is carried out. A similar system like the ladder test system is used for testing the chip and assembly after a cycle period. For the half-stave the complete off-detector electronics and power supplies like it is foreseen to be in the experiment is used. The results of these measurements are discussed in the following section.

Measurements and Results

As mentioned previously the aim of the aging tests is to proof the stability of the different components of the SPD. First, the functionality of the components is tested. After the components are put into a heating chamber (Fig. 3.24). After each cycling period a functionality test is carried out according to the test procedures described in the previous sections.

Half-stave

The half-stave is tested after 50, 100, 150 and 200 cycles with $T_{\max} = 45$ °C and $T_{\min} = 15$ °C (Fig. 3.25). After each cycle period a full functionality test is performed on the half-stave including a measurement of the optical power, while a JTAG validation test of the MCM is performed during the cycling period.

After 100 cycles the optical package died during the test phase. It turned out that the optical package got too hot during heating due to the powered MCM. The temperature specification for this unit lies at 50 °C. The package was replaced and the temperature of the heater adjusted to $T_{\max} = 40$ °C. Table 3.3 gives an overview of the measured values over the cycling period.



Figure 3.24: Heating chamber used for the cycling tests.

Cycles	Min. Threshold	$I_{\text{det}} [\mu\text{A}]$	Temperature [$^{\circ}\text{C}$]	Opt. Power [μW]
0	214	8.94	59.5	851
50	213	9.08	57.5	883
100	214	1.87	32.1	895
150	213	2.73	37.1	610
200	213	2.96	35.4	634

Table 3.3: Summary of the half-stave measurements carried out after the cycling. After the first two cycling periods the leakage current was high due to missing thermal grease. Nevertheless, the leakage current increases after each cycling period.

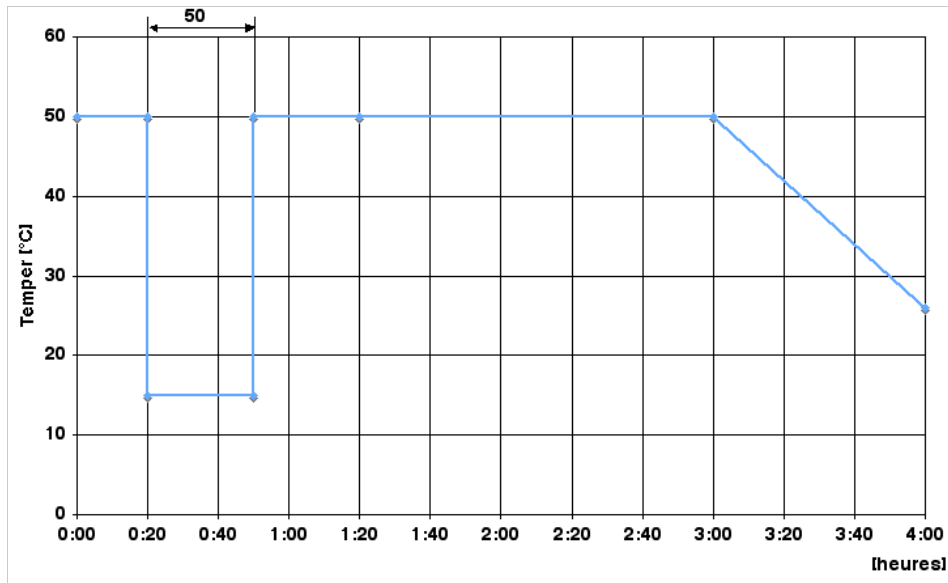


Figure 3.25: Cycling parameters

The heater is controlled by software. The picture shows a graph of the cycling parameters.

The minimum threshold of the half-stave does not show any change over the cycling periods (Fig. 3.26), whereas the leakage current increases (not taking in account the first two cycles, where the thermal grease was missing). The optical power seems to decrease with the time which indicates an effect on the optical package although the temperature was reduced after the first package died.

In Fig. 3.27 the leakage current and the temperature is plotted over the cycling periods. It can be seen that the temperature of the bus in the first two measurements is significantly higher compared to the latter measurements. It turned out that the half-stave had a bad contact to the support frame which also works as a heat sink. After 50 cycles the thermal grease was replaced which resulted in a much better thermal contact and a drop of the temperature by nearly 15 °C. Also the leakage current decrease since it is strongly depending on the temperature.

The measurements show no significant damage to the half-stave over the cycling periods. Due to the excess of the temperature specification of the optical package the pin diode in this component was destroyed. This effect is not related to the aging of the half-stave since the temperature of the MCM during the operation of the detector is around room temperature and therefore far away from the temperature reached in these tests.

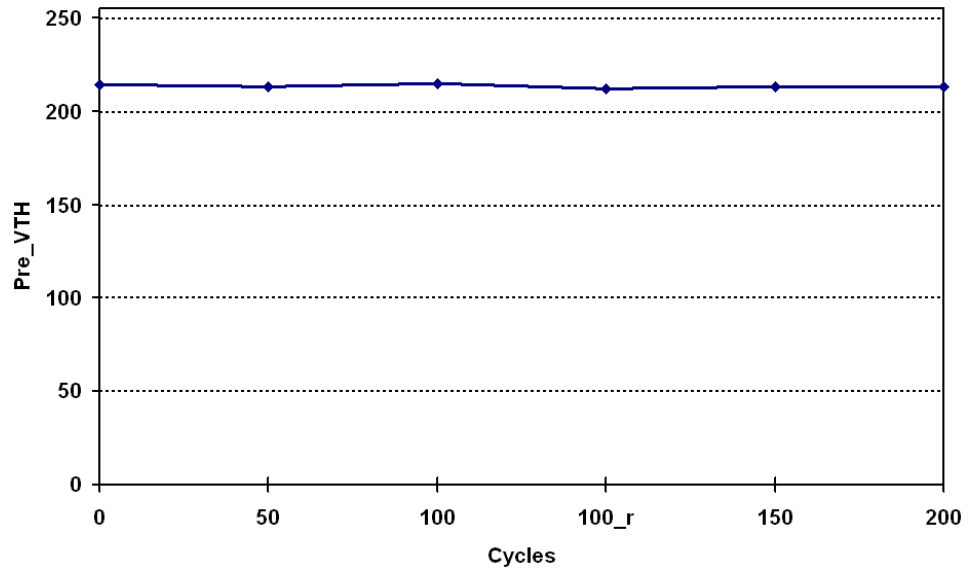


Figure 3.26: The minimum threshold of the half-stave stays constant over the cycles.

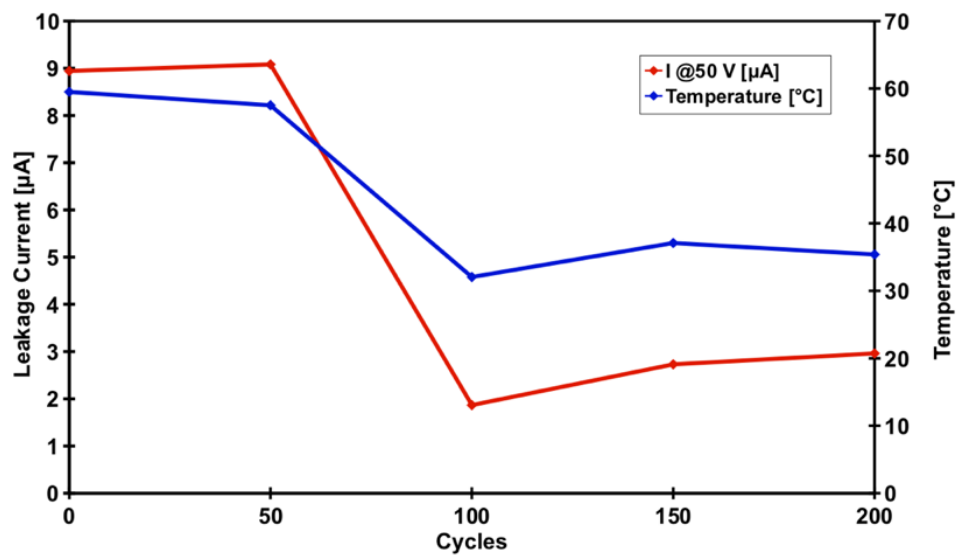


Figure 3.27: The picture shows the leakage current after each cycling step. In the beginning the current was high due to the high temperature (measured with thermal camera) of the bus.

Assembly and Readout Chip

Assembly and readout chip are tested with a test setup similar to the one of the ladder tests. Both components are tested after 25, 75, 175 and 275 cycles. On one half of the readout chip and the assembly Globtop was applied which is a special electronic glue with good encapsulation properties. It has an excellent thermal cycling and mechanical stability and provides very good humidity protection. The goal of this test was to see if the Globtop on these modules and the wire bonds accelerate the aging properties.

On the second half of the wire bonding connection on the readout chip and the assembly Araldite was applied, which is a two-component glue widely used in industry. Araldite is used as a protection of the wire bonds during the half-stave assembly. Araldite was studied as an alternative to Globtop to provide protection of the wire bonding connections.

The leakage current of the assembly shows no change over the full cycling period (Fig. 3.28). The high first value is due to a too short measurement time of the software. In later measurements the waiting time between each step was increased properly in order to give the sensor time to stabilize. Fig. 3.29 and Fig. 3.30 shows that also the minimum threshold of chip and assembly show no degradation. But after 25 cycles the number of dead pixels of the assembly increased significantly. The measurements showed that one column did not respond to the test pulse and the source test. The reason for this malfunction could be manifold: either the data output of this column which is via a single wire bond is damaged, the data output buffer of the ASIC is working incorrectly or the configuration is not loaded correctly into the chip. Several rests and power cycles of the chip did not reactivate the output of the column. After 175 cycles a second column, which is directly next to the dead column, did not respond to test-pulse and source test (Fig. 3.31). This column could be reactivated after several times of re-setting of the chip. The wire bonds of both columns are covered by Globtop which makes it impossible to see if the bond is broken since Globtop is not transparent (Fig. 3.32). Concerning the column which does not provide any output a failure of the wire bonding connection is the most likely cause of the malfunction. For the second column a complete failure of the wire bond is unlikely as data from individual pixels are still visible. The data from all other columns in the chip are transferred correctly which would not be possible if the general chip configuration is loaded incorrectly. The most likely cause for the partial inefficiency of one column is a bad contact to the output pad. The exact cause cannot be determined by visual inspection or electrical measurement as the Globtop prevents any access to this pad.

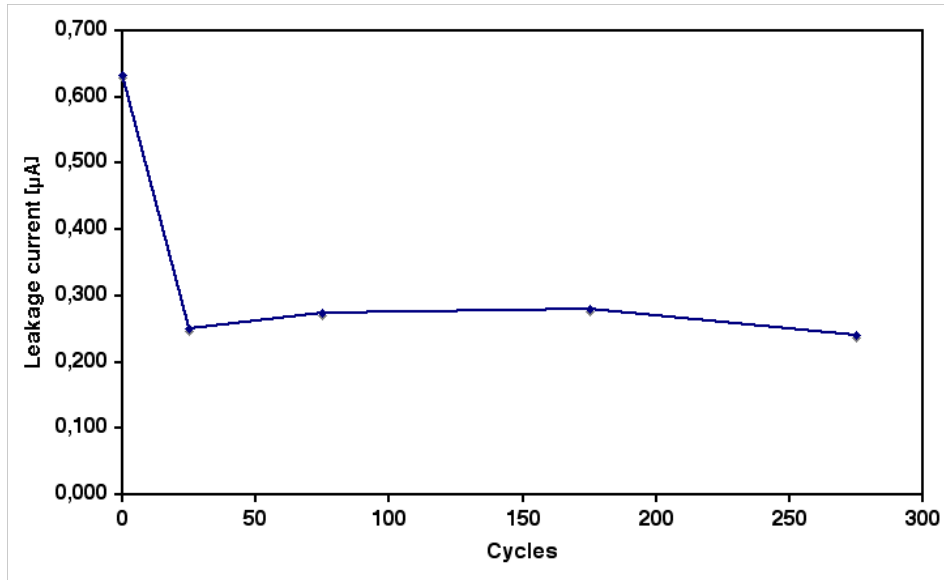


Figure 3.28: Leakage current of assembly 7.

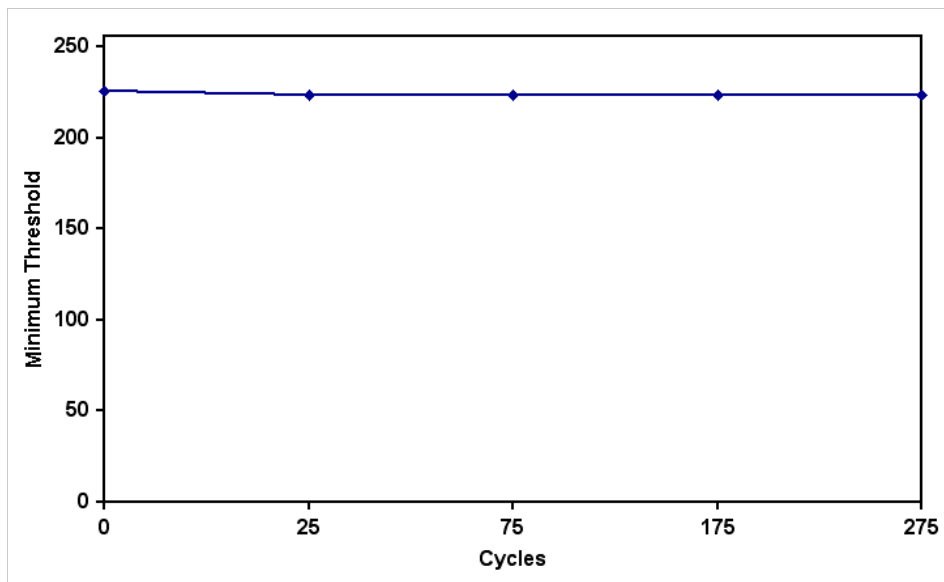


Figure 3.29: Minimum threshold of the readout chip.

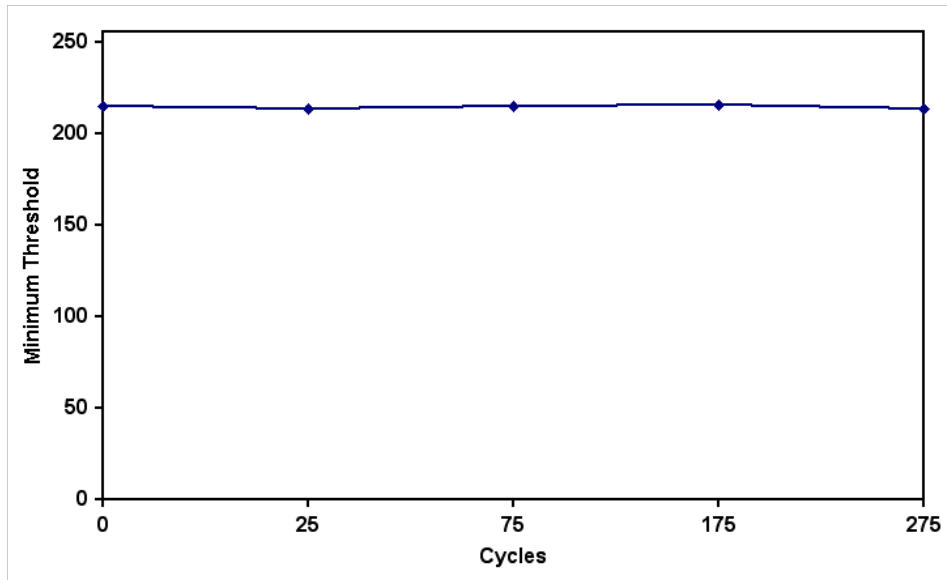


Figure 3.30: Minimum threshold of the assembly.

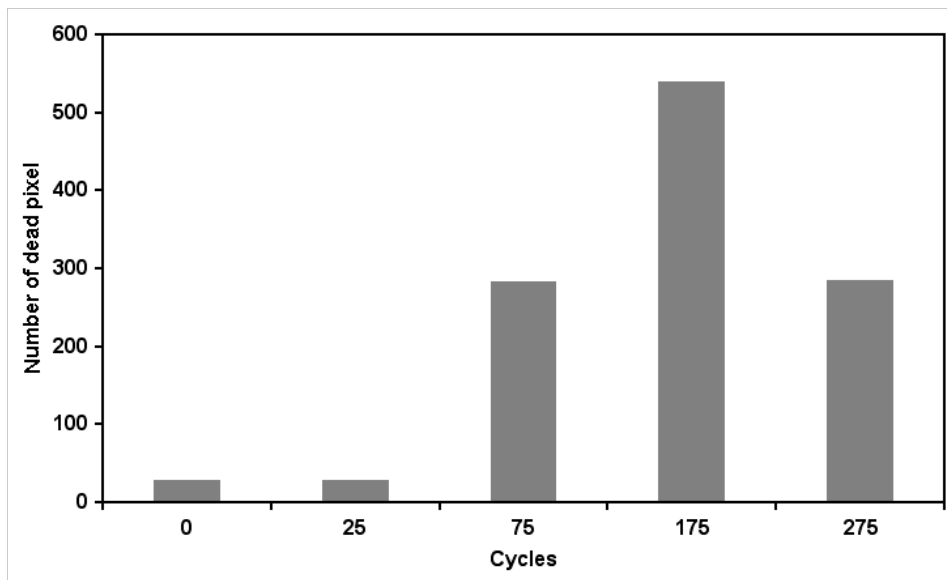


Figure 3.31: The diagram shows the number of dead pixels after each cycling period. After 175 cycles one column partly did not respond to the test pulse and source test. After resetting the chip several times this column could be reactivated.

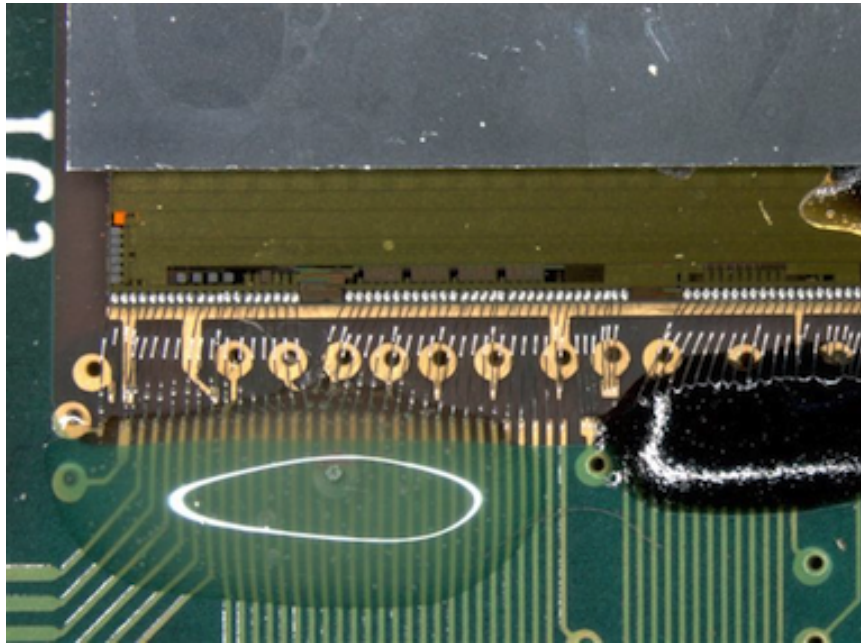


Figure 3.32: The picture shows Araldite (left) and Globtop (right) on the wire bonds.

3.2.4 Optical Tests

The functionality of the optical connections is vital for the detector operation and performance. Therefore, the power margins of the optical links are measured and compared with the measured values of the production state. Furthermore an absolute qualification of the optical power is given to have a comparison after the integration and installation in the ALICE experiment. Finally, an evaluation of the digital signal is taken on a subset of half-staves by analyzing eye diagrams⁸ on an oscilloscope to estimate the error rate and the robustness of the optical links. In the next sections a short description of the power measurements and evaluation of the eye diagram is given. A detailed explanation of these measurements is given in [41].

⁸An eye diagram, also known as eye pattern, is an display on the oscilloscope in which a digital data signal sent from a receiver is repetitively sampled. The vertical opening gives information if data transition is possible, whereas the horizontal opening gives an time interval for data analyzing.

Power Measurements

The power output of all half-staves is measured with a power meter and for comparison with an oscilloscope. For the measurement a LeCroy WP7100A oscilloscope⁹ with 1 GHz bandwidth and a Kingfisher KI3600¹⁰ power meter is used. The operating wavelength λ is 1310 nm and the total uncertainty of the power meter is 0.3 dB. Due to accessibility limitations on the fully assembled second Half-barrel two different setups were used for the measurements (Fig 3.33 and Fig. 3.34). The power loss lies between 0.4 dB - 0.5 dB for setup 1 and ~ 0.6 dB - 0.7 dB for setup 2. A detailed description of the setup can also be found in [41].

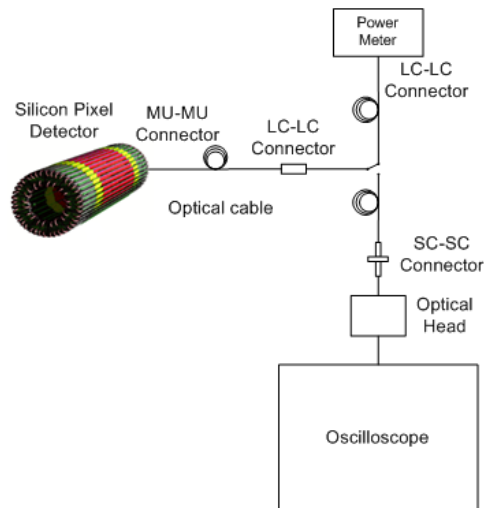


Figure 3.33: The picture shows the setup for the power measurements and eye diagram evaluation of HB 1. The signal from the detector is received either by the power meter or the oscilloscope.

Eye Diagram

The eye diagram is a useful tool to evaluate the quality of the signal in a digital transmission. It contains information about the signal-to-noise ratio, clock timing jitter and skew. The eye diagram is obtained with an oscilloscope with memory by superposition of several acquisitions of the digital signal and using the on-board functionality for data taking. Fig. 3.35 shows a typical eye diagram taken with an half-stave. The eye is built by two signals crossing twice by changing their transition level. One signal changes

⁹<http://www.lecroy.com/tm/products/scopes/WavePro/default.asp>

¹⁰<http://www.kingfisher.com.au/Products/KI3600/3600.htm>

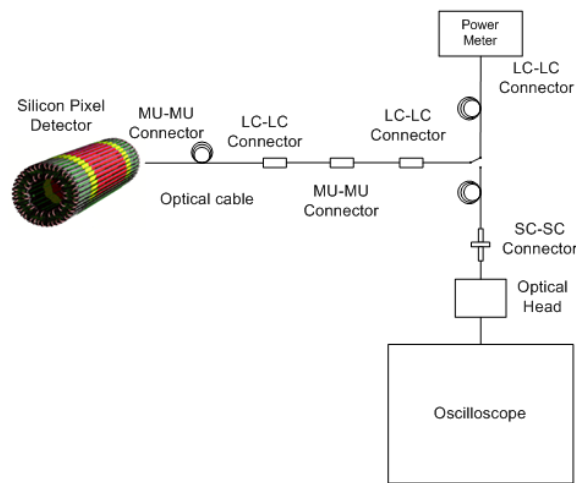


Figure 3.34: The picture shows the setup for the power measurements and eye diagram evaluation of HB 2. Two additional connectors and 17 m of fiber are added due to accessibility limitations.

from the high level, the so called *mark* level, to the low level, the so called *space* level and back to the *mark* level. The second signal changes from *space* to *mark* and again to *space* level. For the selection of the eye diagram one has to consider two constraints: First, the window of the measurement has to be as narrow as possible to be as close as possible to the point of interest. Second, the window has to contain a sufficient number of transitions in order to derive statistical quantities without increasing the time of measurement too much. The dimensions of the window is always a compromise between these two constraints. For the evaluation of the eye diagram, one has to measure the horizontal and vertical opening of the eye.

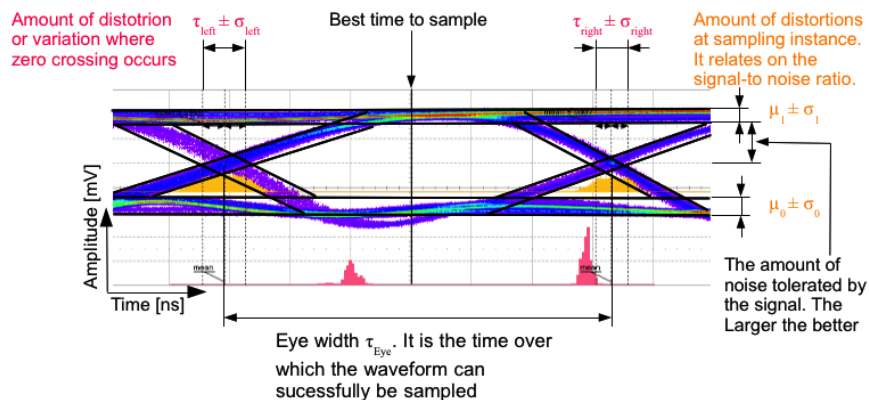


Figure 3.35: Typical form of an eye diagram. The measured values for τ_{left} , τ_{right} , μ_0 , μ_1 and their standard deviations are labeled.

The horizontal width covers the hole time range and is centered at the half amplitude level. The two yellow histograms in Fig. 3.35 correspond to the left and right crossings of the repetitively sampled rising and falling flanks of the eye. The mean values of these histograms, τ_{left} and τ_{right} , yield the temporal positions of the half amplitude levels at the left and right flank. With these two values the width of the eye diagram can be expressed with the formula

$$\tau_{Eye}[ns] = \tau_{right} - \tau_{left}. \quad (3.1)$$

The standard deviations τ_{left} and τ_{right} of the two horizontal histograms describe the RMS of the signal.

The vertical dimension covers the whole measured amplitude range. There are also two values recorded in this direction which correspond to the mark and space amplitudes of the eye diagrams (red histograms in Fig. 3.35). The mean value μ_1 in the mark distribution corresponds to the mean amplitude of the *marks* in the signal whereas the mean value of the space distribution μ_0 corresponds to the mean amplitude level of the *spaces* in the signal. The mean mark amplitude μ_1 and mean space amplitude μ_0 give rise to several characteristic values which will be described below.

The Extinction Ratio ER, which describes the properties of the optical data transmitter, can be calculated using the formula

$$ER [dB] = 10 \cdot \log_{10}\left(\frac{\mu_1}{\mu_0}\right). \quad (3.2)$$

Analog to the timing jitter described above the standard deviation σ_1 of the vertical histogram yields to the amplitude noise AN

$$AN [mV] = \sigma_1. \quad (3.3)$$

A high amplitude noise indicates a poor signal quality as it degrades the eye opening of the eye diagram. To get an absolute quality indicator for the data signal, the amplitude noise must always to be considered in combination with the mean signal amplitude (Signal-to-noise ratio) which can be described with the formula

$$SNR [dB] = 10 \cdot \log_{10}\left(\frac{signal}{noise}\right) = 10 \cdot \log_{10}\left(\frac{\mu_{0,1}}{\sigma_{0,1}}\right). \quad (3.4)$$

In order to compare the eye diagram of different signals one can define the following factor

$$Q_{Eye} = 1 - \frac{A \cdot (\sigma_1 + \sigma_0)}{\mu_1 - \mu_0}. \quad (3.5)$$

The Q_{Eye} factor defined in these tests includes the standard deviations and the mean values of both distributions. Under the assumption that the amplitude noise is dominated by Gaussian noise, the factor A is chosen such that the mark and space levels are well separated. The factor A is set to 3 to consider the error level of the Gaussian distribution of 0.1 %. If this is not the case the receiver could not distinguish between those two levels and produces errors. A low value indicates a low signal quality whereas a value closer to 1 shows a better signal quality. Q_{Eye} is used for comparison with other eye diagrams in this work [42].

Measurements and Results

Table 3.4 shows a summary of the optical power per half-barrel and side of the detector. The derived measurements of the power meter match with the values of the oscilloscope considering the errors mentioned previously. Fig. 3.36 and Fig. 3.37 show the histogram of the optical power for HB1 and HB2.

Half-Side	Power Meter				Oscilloscope			
	Mean Power [dBm]	σ [dBm]	Mean Power [μ W]	σ [μ W]	Mean Power [dBm]	σ [dBm]	Mean Power [μ W]	σ [μ W]
HB1 Side A	-1.13	0.79	689.52	173.40	-1.51	0.80	626.11	159.58
HB1 Side C	-1.11	0.96	705.25	186.41	-1.56	0.95	639.08	171.23
<i>HB1 A & C</i>			<i>697.40</i>	<i>178.80</i>			<i>632.09</i>	<i>162.84</i>
HB2 Side A	-1.83	1.57	782.63	135.03	-2.25	1.58	717.13	125.14
HB2 Side C	-1.83	2.02	792.90	163.91	-2.26	2.02	714.57	148.92
<i>HB2 A & C</i>			<i>787.77</i>	<i>150.27</i>			<i>715.90</i>	<i>136.38</i>

Table 3.4: Mean values and standard deviations of the power output for each half barrel of the SPD.

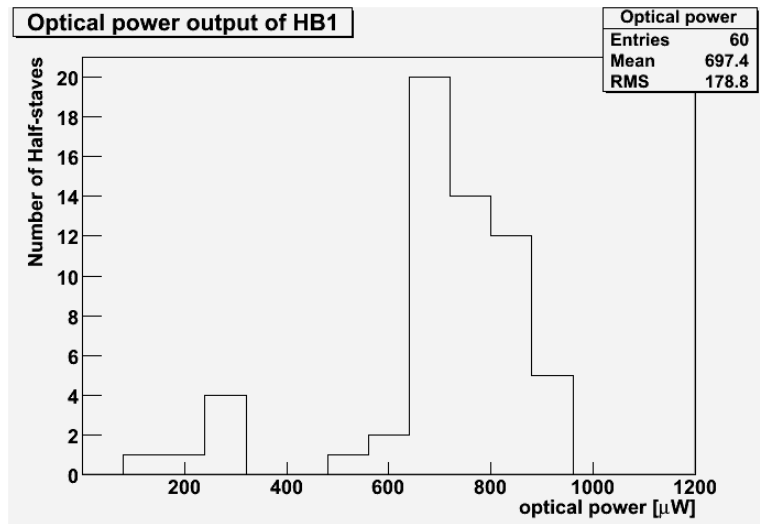


Figure 3.36: Optical Power of all half-staves of Half-Barrel 1.

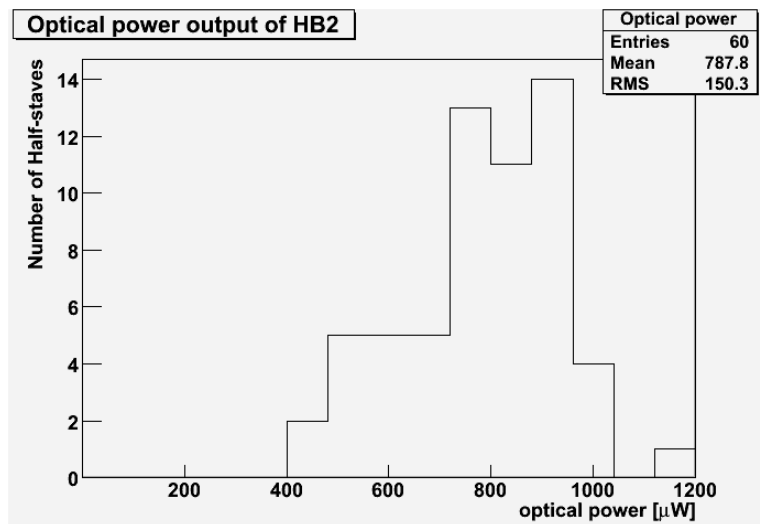


Figure 3.37: Optical Power of all half-staves of Half-Barrel 2.

In table 3.5 and table 3.6 the measured values for the eye width τ_{Eye} , extinction ratio ER and the quality factor Q_{Eye} are listed for HB1 and HB2, respectively. Fig. 3.38 and Fig. 3.39 show the histograms of the extinction ratio and the quality factor. Looking on the standard deviations σ_0 and σ_1 listed in table A.1 and table A.2 it can be seen that mainly σ_0 has bigger values which is a result of the under shots in the space levels. The bigger σ_0 leads to a smaller (worse) Q_{Eye} . The extinction ratio ER which shows the properties of the optical data transmitter of each half-stave gives no indication of a degradation of the transmitter output after the integration in the half-barrels.

The optical power measurements show that all half-staves have sufficient power output which is far above the specification limit. The worst case optical attenuation due to patch panels, splitter and degradation due to radiation and aging is 9.5 dB for side C and 10 dB for side A, respectively. The margin of the transmitter lies at ~ -16 dBm. No difference between the values measured on HB1 and HB2 can be observed. The values are comparable with the production state and show no degradation [43]. Also, the detailed analysis with the cooling system and the bus show the expected behavior.

Detailed analysis of the optical power with different configurations of the half-stave are carried out. More information can be found in [41].

The evaluation of the eye diagrams show a good signal quality of the transmitters. The eye width and the quality factor show similar values on all half-staves. Despite the high bandwidth of 800 Mbits/s the signal quality satisfies the specifications and guarantees data transmission of very good quality for the whole operating time of the detector.

Half-Stave	τ_{Eye} [ns]	ER [dB]	Q_{Eye}
1-C-1	1.246	2.298	0.897
2-A-0	1.302	2.623	0.906
2-A-2	1.316	2.711	0.790
2-A-5	1.225	2.543	0.887

Table 3.5: Measured eye width τ_{Eye} , extinction ratio ER and quality factor Q_{Eye} for some half-staves of HB 1. One can see that the Q_{Eye} factor of all half-staves is close to 1 which indicates a good data transmission quality. The eye width and extinction ratio show similar values on all half-staves.

Half-Stage	τ_{Eye} [ns]	ER [dB]	Q_{Eye}
5-A-0	1.283	2.442	0.739
5-A-1	1.220	2.340	0.702
5-C-0	1.234	2.354	0.815
5-C-1	1.287	2.260	0.858
6-A-2	1.216	2.129	0.837
6-C-2	1.206	2.262	0.738
7-A-5	1.206	2.067	0.853
7-C-5	1.216	2.349	0.717
8-A-3	1.218	2.144	0.838
8-A-4	1.210	2.213	0.826
8-C-3	1.236	2.272	0.746
8-C-4	1.236	2.363	0.654
9-A-0	1.238	2.462	0.875
9-A-1	1.230	2.188	0.765
9-C-0	1.268	2.272	0.850

Table 3.6: Measured eye width τ_{Eye} , extinction ratio ER and quality factor Q_{Eye} for HB 2. Also on the second half-barrel the Q_{Eye} factor of all half-staves is close to 1 and the eye width and extinction ratio show similar values.

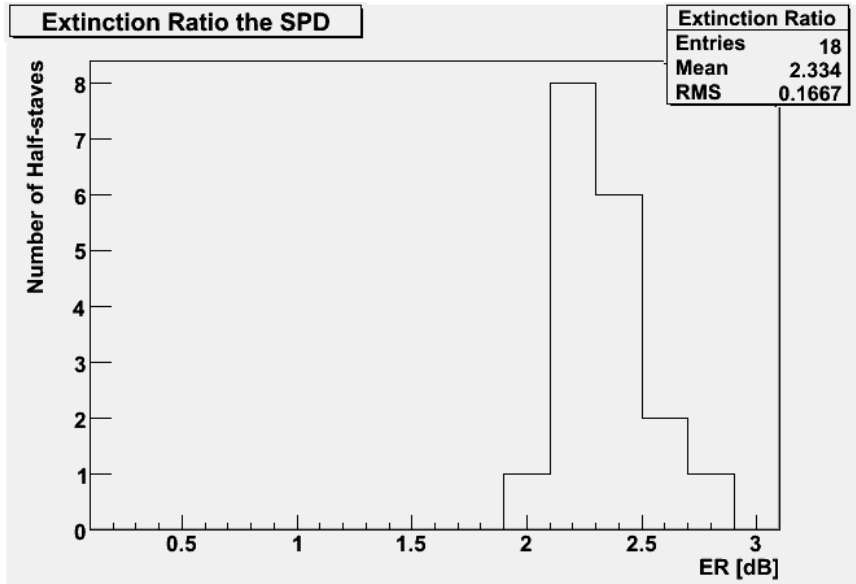
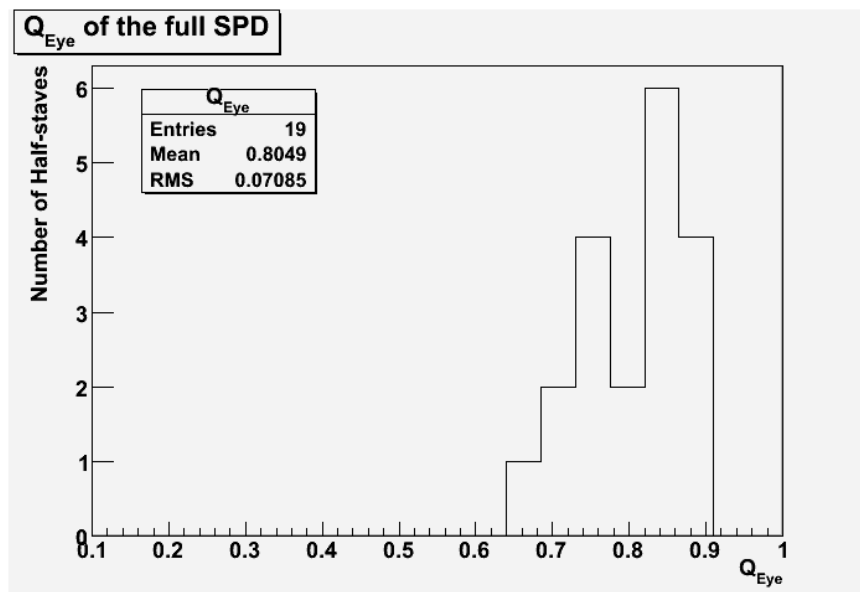


Figure 3.38: Extinction ratio of the half-stave sample.

Figure 3.39: Q_{Eye} of the half-stave sample.

Chapter 4

Commissioning and Integration

In this chapter a description of the setup for the sector and half-barrel tests is given. This thesis also focuses on the testing, commissioning and integration of the ALICE SPD. The tests have been carried out in the Departmental Silicon Facility (DSF) at CERN using the final power supply installation, cables, readout chain and cooling system as foreseen in the experiment. Each of the ten sectors was tested separately after arrival. The results of each step in the sector tests are compared with the tests after integration to the two half-barrels. Further, a short description of the installation of the SPD in the ALICE experiment is given in the last part of this chapter.

4.1 Test Setup

4.1.1 Carbon Fibre Support

After assembling of the half-staves, the modules are mounted on the *Carbon Fiber Support* (CFS) with a precision of $100\ \mu\text{m}$ (Fig. 4.1). Each sector consists of four half-staves in staged mounting configuration forming the inner layer and six half-staves in windmill configuration to form the outer layer of the SPD. The CFS, which houses also the cooling tubes, allows a direct contact between cooling and the silicon chip backplane via a thermal grease and maximizes the thermal coupling of the system. The CFS has a very high global and local stiffness with a deformation of the order of $1\ \mu\text{m}$ or less in the service conditions. The wall thickness of the CFS is about $200\ \mu\text{m}$ in

the sensitive area increasing to $600\ \mu\text{m}$ at the ends in order to allow the positioning of the mechanical references and of the components needed for the global assembly of the sectors. To minimize high Z material close to the sensitive volume the coupling pins and pin seats also are made of carbon fiber. The half-stave is strongly coupled to the stiff carbon fibre structure by using UV tags and carbon fiber springs. The expected maximum deformation of a fully equipped sector will be $\sim 10\ \mu\text{m}$ in all directions. [44]

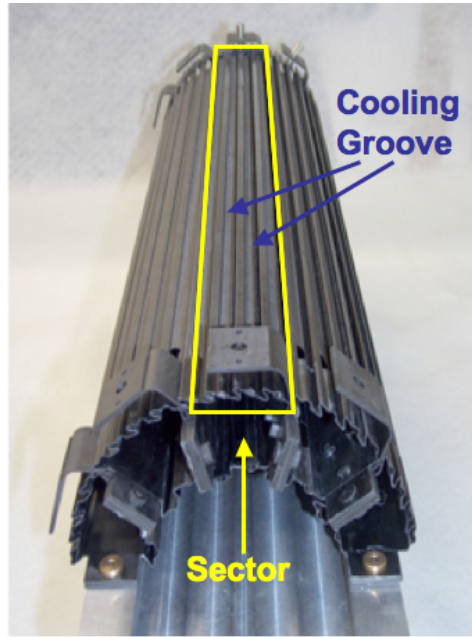


Figure 4.1: Picture of an unequipped carbon fiber support forming a half-barrel.

4.1.2 Cooling System

The produced heat load of the on-detector electronics is $\sim 23\ \text{W}$ per stave. an evaporative cooling system using C_4F_{10} as coolant was chosen due to following strict design requirements:

- low material budget
- long term stability
- chemical compatibility with the carbon fibre and the beryllium beam pipe in case of a leak
- minimal the temperature gradient along the stave

- temperature of the cooling duct above the dew point

It follows the Joule-Thomson cycle. The compressed and overcooled liquid is brought to the coexistence phase inside the cooling duct by a pressure drop inside the oblate capillaries with internal dimensions of $600 \mu\text{m} \times 550 \mu\text{m}$. The heat abduction through phase transition takes place inside the cooling tube at 15 - 18 °C and a pressure of 1.9 - 2.0 bar. The gas is pushed to the condenser by a compressor, where the liquid phase is recovered again by heat transfer to cold water ($\sim 6 \text{ °C}$). The evaporation temperature is controlled by regulating the pressure in the return line. The PHYNOX tubes have a wall thickness of $40 \mu\text{m}$ and an initial diameter of 2.6 mm squeezed down to a flat profile with a overall thickness of $600 \mu\text{m}$. The thermal contact with the half-stave is carried out via a thermal grease layer. The cooling system is controlled by an PVSS graphical interface providing access and pressure control for each loop and weight monitoring of the liquid tank [44].

During the sector and half-barrel tests the temperature distribution of the half-stave is measured with a thermal camera and with Pt1000 sensors. (Fig. 4.2).



Figure 4.2: Infrared picture of the outer layer of an half sector during operation.

4.1.3 Sector and Half-Barrel Tests

The sector and half-barrel tests were carried out in a clean-room at CERN. The assembled sector was mounted on a test bench and connected to the power supplies and off-detector electronics (Fig. 4.3). In order to get as

close to "real" conditions as prevailing in the ALICE experiment, final components are used for the sector and later also in the half-barrel tests:

- C₄F₁₀ cooling plant
- 30 m low and 100 m high voltage cables
- 35 m optical fibres
- CAEN Easy crates, high and low voltage modules
- Interlock system
- DAQ and trigger system
- SPD DCS and ECS



Figure 4.3: Test bench in the clean-room at CERN. In foreground 2 sectors are mounted, in the background the first half-barrel is mounted.

Each sector had to be qualified separately before five sectors are mounted to a half-barrel in order to guarantee the full functionality of the SPD. In parallel a qualification of the off-detector electronic elements is carried out. The following list gives an overview of the tested components:

- Final cooling system

- DCS and interlock
- Final Power supplies
- Off-detector electronics
- ALICE trigger modules
- ALICE DAQ system and online monitoring
- Calibration procedure in the ALICE
- DCSFramework

The functionality tests can be divided into two groups, *Static Tests* and *Calibration Tests*. Table 4.1 lists the different steps processed in these tests:

Static Tests	Calibration Runs
Visual inspection	Minimum Threshold Scan
Pixel chip and MCM current consumptions	Mean Threshold Scan
Sensor I-V characteristic	Generic DAC Scan
Pixel chips and MCM temperature	Uniformity Matrix Scan
Thermal image	Noise Scan
Optical power	Delay Scan
	Fast-OR Uniformity Scan

Table 4.1: Functionality tests carried out on each sector and on both half-barrels.

Fig. 4.4 shows the setup schematic of the integration tests. Noise Scan and FastOR uniformity scan is carried out with a ~ 1 MBq Sr^{90} source. After the integration of the sectors to the half-barrel the same tests are carried out, except the source test since the radiation of the source would not allow to sufficiently illuminate both layers due to the relative low energy spectrum of the source and the amount of material present. Finally, a detailed mechanical integration test is carried out in order to test the integration of the SPD around the beam pipe in ALICE.

4.1.4 Cosmic Test

A cosmic run has been performed on sectors with six hours in total of data taking using the FastOr trigger. For this run the complete readout chain and data analysis tools were used and the sector was controlled via the DCS.

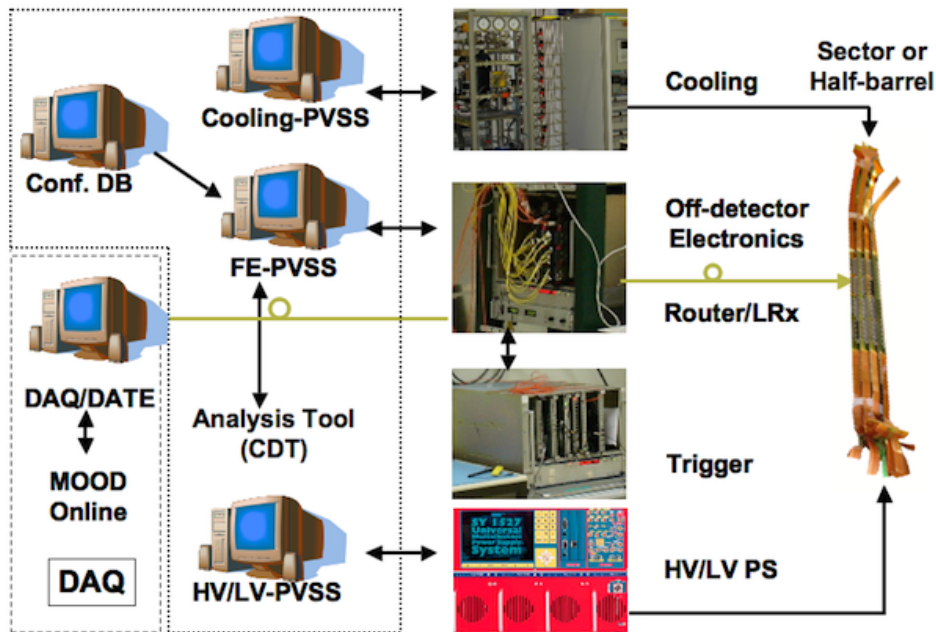


Figure 4.4: Test setup of the SPD sector and half-barrel tests. Sector or half-barrel were connected to the off-detector electronics via fibre optics [38].

In section 4.2.6 the results of this run are shown. The sector is mounted horizontally in order to increase the probability of cosmic ray passing through the sector (Fig. 4.5).

4.2 Measurements and Results

4.2.1 Visual Inspection

The first step during the sector test is the visual inspection (Fig. 4.6). The aim of this procedure is to detect any damages that could have occurred during the transport of the sector to CERN. Further, a cross check of the half-stave IDs and positions on the sector is done, which is important to load the right configuration file for the calibration runs. After the integration of the sector in the half-barrel the IDs are not visible any more.

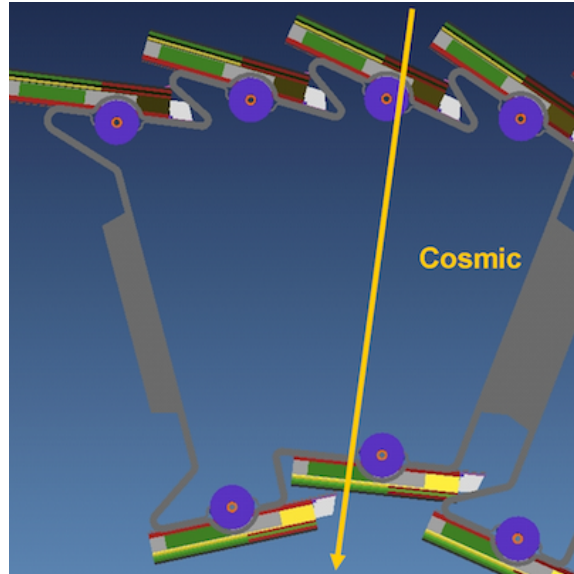


Figure 4.5: Position of the sector during the cosmic run. Inner and outer layer are parallel to the test bench.



Figure 4.6: Picture taken during a visual inspection. It is important to find any damage on the sector before switching on. For instance bended wire bonds would cause short circuits.

4.2.2 Leakage Current

The standard operation voltage (working point) of the ALICE silicon sensor is set to 50 V (depletion voltage is ~ 12 V). The I-V curve of each half-stave is recorded between 0 - 50 V. 11 half-stave sensors are not operable at 50 V due to current breakdown, but all can be operated above the depletion voltage. The working point is then set to a lower voltage in order to comply with the current limit of $5 \mu\text{A}$. Fig. 4.7 shows the leakage current distribution of all 120 half-staves at working point and normalized to 25°C . Also during the half-barrel test the leakage current was measured (Fig. 4.8). It can be seen that some half-staves have higher values whereas most of the other half-staves have a shift to smaller leakage current. This is a result of the integration of the sectors since the outer layer is covered by the CFS and for that not illuminated with light. The inner layer on the other hand was not covered and the leakage current increased due to the sensitiveness to light. During the sector tests the sector was covered with a opaque cover to reduce the light influence on the sensor. The mean leakage current is $1.27 \pm 1.00 \mu\text{A}$ measured during the sector tests and $1.49 \pm 1.65 \mu\text{A}$ for the half-barrel tests. The large rms can be explained by the long tail of the distribution (see Fig. 4.8).

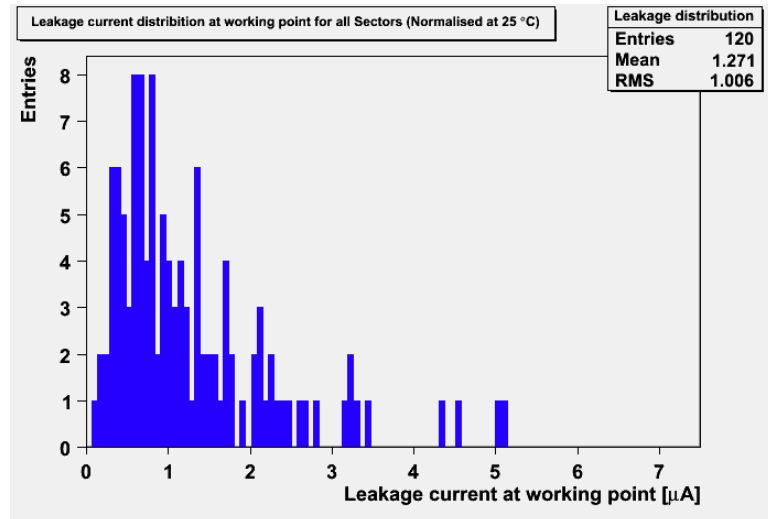


Figure 4.7: Leakage current of all half-staves at working point.

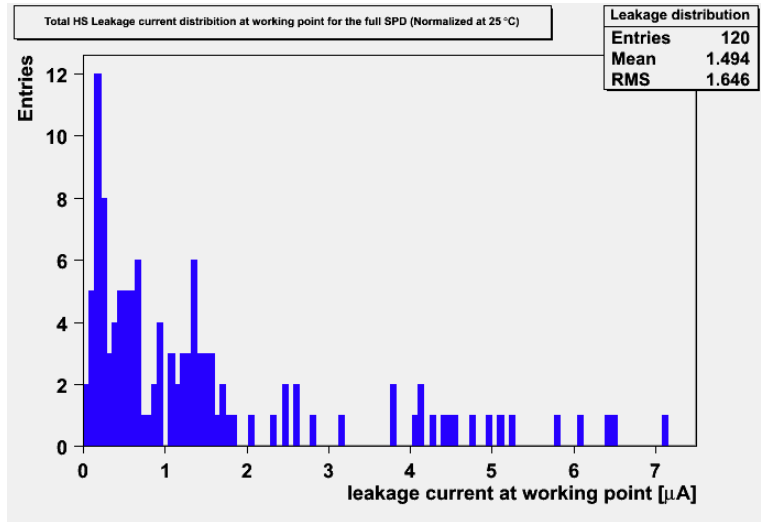


Figure 4.8: Leakage current of the full SPD after half-barrel integration at working point.

4.2.3 Temperature

The half-stave temperatures along the bus are measured by two independent Pt1000 chains. On each chip a Pt1000 element is mounted. One chain is read by the routers, one is directly measured by the PLC system. Both systems provide an interlock at high temperature, which turns off the complete half-stave in order to avoid damage on the module.

Out of 120 half-staves three show connection problems in the Pt1000 chain read by the PLC. On those half-staves the chip temperature can only be measured using the second Pt1000 chain. The mean temperature on all sectors is 28.3 ± 2.0 °C (Fig. 4.9), which is - as expected - the same also for both half-barrels (Fig. 4.10). The mean temperature for the sector and half-barrel tests is 28.3 ± 2.0 °C.

4.2.4 Minimum Threshold

The minimum threshold (MinTHR) is measured by varying the global Pixel Chip DAC named pre_VTH. It is the lowest global value at which the noise induced by the system is suppressed. Each pixel cell has a digital readout which converts the charge deposited on the sensor to voltage and compares this with a threshold given by the internal discriminator. This threshold is inversely proportional to the pre_VTH DAC value. Thus, a higher DAC

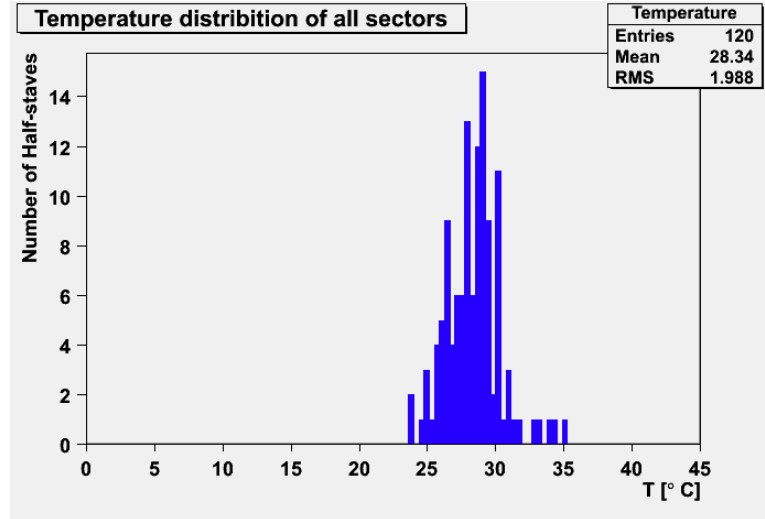


Figure 4.9: Temperature distribution for all half-staves mounted on sectors.

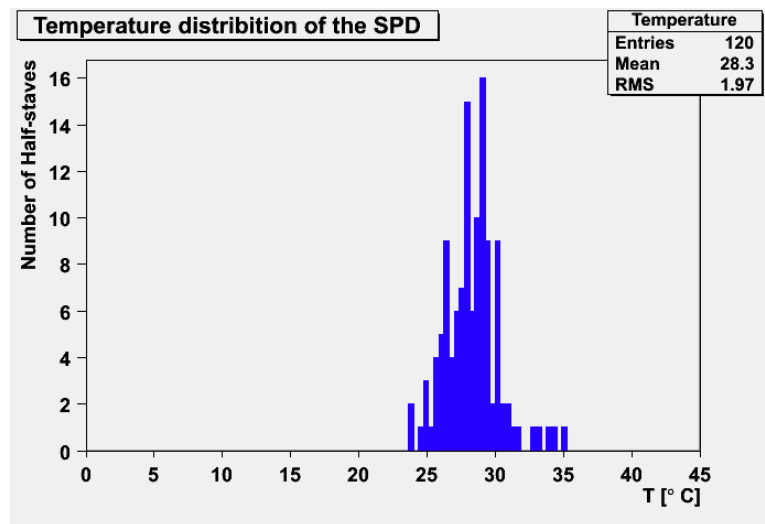


Figure 4.10: Temperature distribution of all half-staves after integration into the two half-barrels of the SPD.

value results in a lower threshold and vice versa. The correspondence between DAC units and electrons equivalent depends on different electronic settings. To get a rough estimation one can consider that a pre_VTH DAC of 200 corresponds to $\sim 2500 e^-$ and a DAC unit corresponds to $\sim 120 e^-$. As expected the values do not change between sector and half-barrel tests. The minimum threshold for the sector tests is 193.5 ± 2.1 (Fig. 4.11) and for the half-barrel tests 195.5 ± 1.8 (Fig. 4.12).

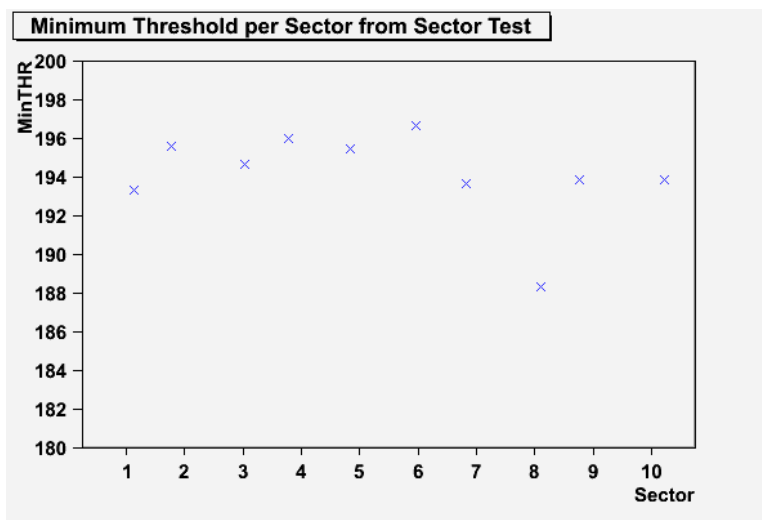


Figure 4.11: Minimum threshold for all sectors measured in the sector tests.

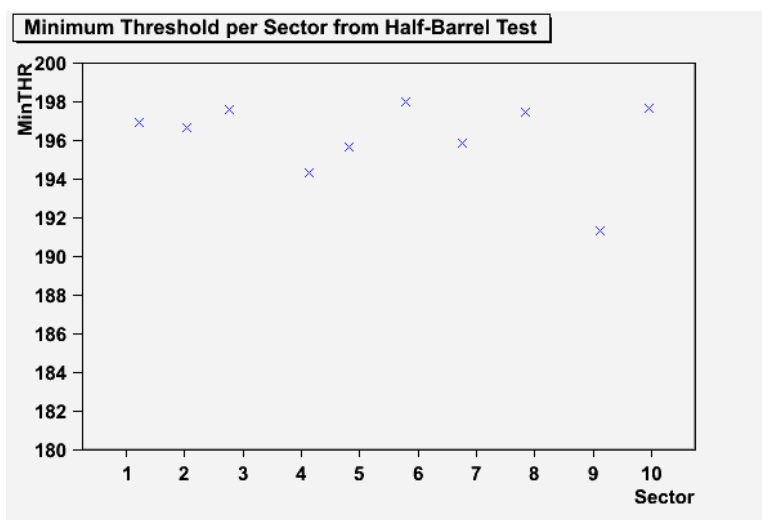


Figure 4.12: Minimum threshold for the complete SPD measured in the half-barrel tests.

4.2.5 Noisy Pixel

Using the test pulse noisy pixels were found by screening the first steps of the minimum threshold scan which corresponds to high thresholds ($\approx 3000 e^-$). The test pulse is injected into the pre-amplifier of the analog part of a pixel cell. If the discriminator of the pixel cell is then firing on the pulse at this high threshold, the pixel is counted as noisy. The total amount of noisy pixels evaluated from the sector test (Fig. 4.13) is 51 which is 0.0005 % of all pixel (~ 10 Millioncells), whereas in the half-barrel test (Fig. 4.14) the noisy pixels amount to 39 which is 0.0004 % of all pixel. Noisy pixels are then masked and will not have any affects to the offline track reconstruction.

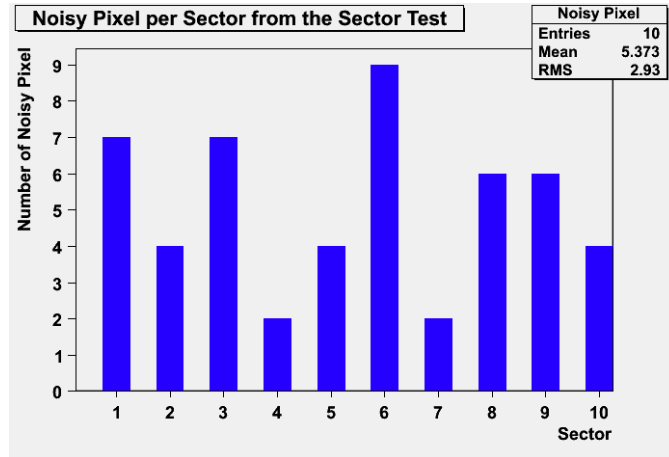


Figure 4.13: Noisy pixel for each Sector taken from the sector tests.

4.2.6 Cosmic Test

A cosmic run has been carried out with one sector. The data is analyzed using the DA software which will also be used later in ALICE. Fig. 4.15 show the z-correlation between inner and outer layer. The lines in the plot indicate noisy pixel which can be removed by software. Before the data could be analyzed a transformation between the on-detector coordinate system to the global experimental coordinate system has to be done.

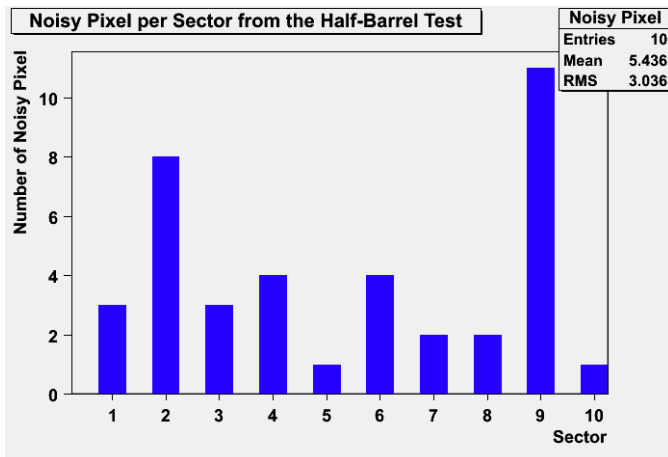


Figure 4.14: Noisy pixel for each Sector taken from the half-barrel tests.

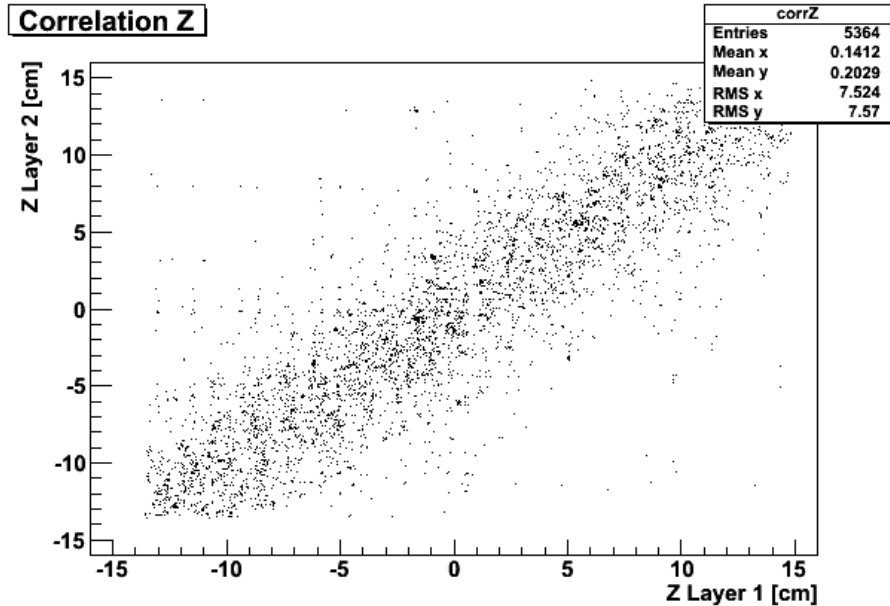


Figure 4.15: The picture shows the z correlation between inner and outer layer of the sector.

4.2.7 Integration of the SPD in ALICE

The SPD is now installed in ALICE. The two half-barrels were packed separately in two boxes which were moved from the cleanroom to the experimental area of ALICE. The installation of the detector was a challenge by itself, since the two boxes had to be moved under the magnet to a platform between TPC and absorber (Fig. 4.16). From this platform the SPD was mounted around the beam pipe (Fig. 4.17) and afterwards the previously installed ITS parts were slid over the SPD (Fig. 4.18). After that the connection to the off-detector electronics, control systems and cooling system was carried out.

After the installation first tests have been accomplished. All MCM could be powered and are working properly. Also the leakage current of all half-staves is verified. The bus could not be powered yet due to the missing cooling system whose installation is currently going on. Until now one side of the detector is completely connected to the final system. The second side will be connected by the end of November 2007. A first test with cosmic rays will be carried out in December.

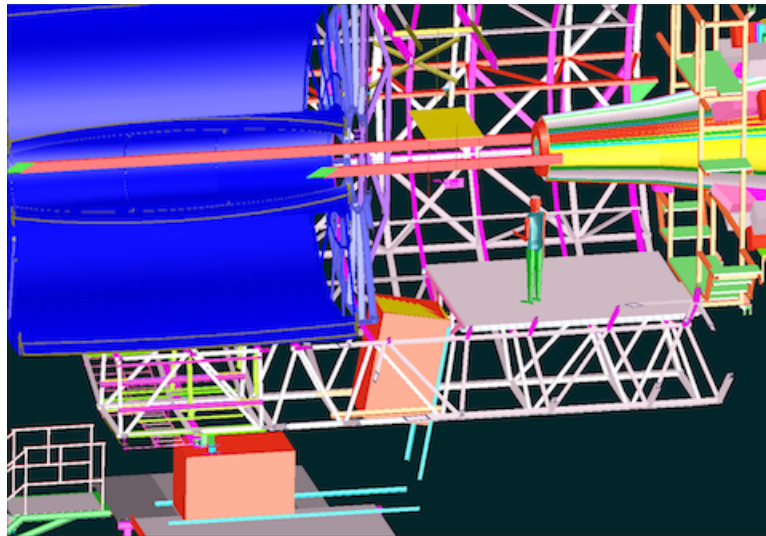


Figure 4.16: The schematic shows how the SPD is moved to the platform between TPC and absorber. Through a narrow tunnel the two boxes housing a fragile detector were moved [6].

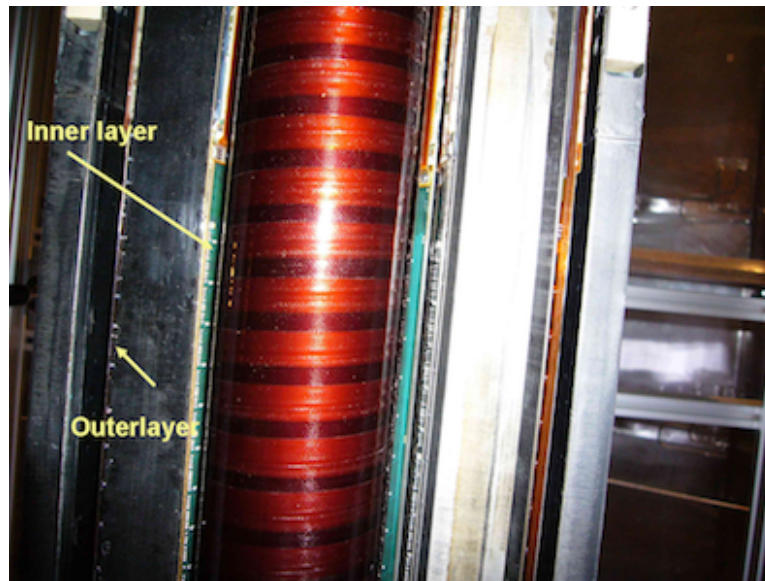


Figure 4.17: The picture shows the upper half-barrel already mounted around the beam pipe. The average distance between inner layer and beam pipe is ~ 3 mm [6].

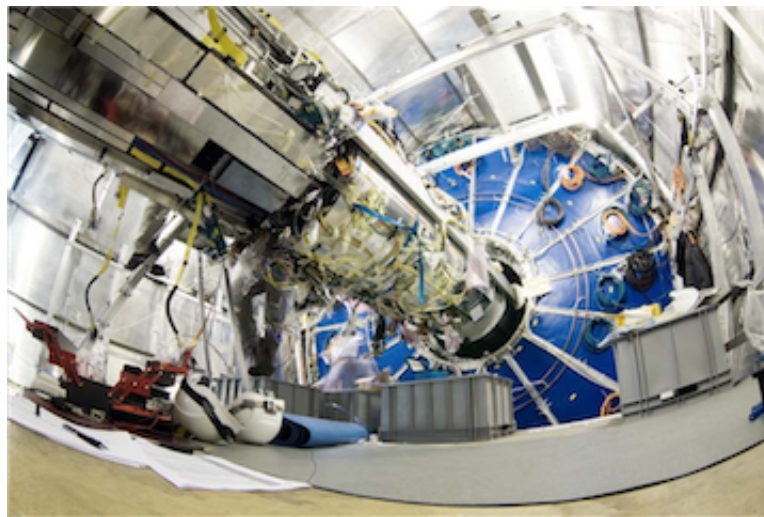


Figure 4.18: The picture shows the ITS mounted adjacent to the absorber. In the upper left corner the absorber can be seen. In the middle the ITS in front of the TPC (blue wheel in the background). The ITS is supported, during the stage of installation, by two auxiliary rails [6].

Conclusion

The ALICE SPD comprises the two innermost layers of the ALICE Inner Tracking System (ITS). The ALICE experiment is one of the experiments at the LHC and will primarily aim to study strongly interacting matter at the extreme energy densities reached at heavy ion collisions at the LHC. The ALICE experiment consists of several sub-detector systems optimized for heavy ion running. This will allow to produce and study the Quark-Gluon-Plasma which is a phase where the quarks and gluons can move freely.

High precision tracking information closest to the interaction point is provided by the SPD which is made of two layers of hybrid silicon pixel detectors. Pixel detectors can provide unambiguous 3D hit information, even in high track multiplicity environments as foreseen in heavy ion collisions. The pixel size is $50\ \mu\text{m}$ in $r\phi$ -direction and $425\ \mu\text{m}$ in z-direction. Each pixel cell in a high resistivity silicon sensor (p-in-n) is connected via a micro solder bump bond (Pb-Sn) to a electronic cell in a readout chip. The readout chip of the SPD is a mixed signal chip developed in a $0.25\ \mu\text{m}$ CMOS process with radiation hard design layout. Each chip measures $13.5\ \text{mm} \times 15.8\ \text{mm}$ and contains 8192 pixel cells. The sensor size is $70.7\ \text{mm} \times 12.8\ \text{mm}$ with a thickness of $200\ \mu\text{m}$. One sensor is connected to five readout chips which have been thinned to $150\ \mu\text{m}$ to form one ladder of the SPD. In total the detector contains 1200 readout chips and 240 ladders, respectively. Two ladders are assembled to one half-stave using a flexible multi-layer Al-polyamid laminate. The material budget of the innermost layers has to be as low as possible to provide excellent tracking performance even in the low momentum range. Thanks to the use of novel and very thin components each SPD layer corresponds to about $1.14\% X_0$. This implied the use of thin sensors ($200\ \mu\text{m}$), thinning of the readout chips after bump deposition to $150\ \mu\text{m}$, the development of an Al-polyimide based multilayer cable and a light weight support structure and cooling. The SPD is therefore the lowest mass pixel detector in all LHC experiments.

This work was carried out in the period from November 2006 to Novem-

ber 2007 and focuses on the construction of the ALICE pixel detector and the integration tests carried out before installation. To ensure the performance of the full detector each individual component needs to be tested and verified before and after each assembly step. One of the most challenging aspects of the SPD construction was the assembly of the very thin ladders. This work presents the tests carried out during the ladder production. The bump deposition and flip chip bonding of the ladders include several deposition and lithographic steps as well as a dedicated thinning process to achieve the 150 μm thin ASICs. The overall ladder quality is strongly dependent on each of the processing steps and needs to be closely monitored. Missing pixels or malfunctioning ladders will directly impact on the detector performance in the experiment. In order to verify the production quality a series of tests was carried out on each ladder which includes, visual tests, electrical tests and measurements with a source. A classification scheme was developed which selects the ladders into different categories according to the test results. Only class 1 ladders are used for the construction of the SPD. The number of non-working pixels in class 1 ladders is $\sim 77\%$ which is in full agreement with the requirements foreseeing a maximum number of non working pixels in the detector of less than 1%.

The long term operability of the half-staves in the detector is an important aspect to maintain a high and stable detector performance. A thermal cycling study was carried out to verify the long term reliability of the metallic interconnections present on the half-stave. The connections include ultrasonic-wire bonds, Al vias in the bus and the Pb-Sn solder bump bonds. A total of 200 cycles were carried out on one half-stave and for comparison on one readout chip and one single chip assembly. The results show that basic parameters such as the minimum threshold remain stable while an increase in the optical power was observed. The leakage current of the half-stave followed as expected the temperature variation. The thermal grease providing contact to the heat sink was exchanged after 50 cycles and the temperature of the half stave could be reduced. The measurements illustrated the importance of a good thermal contact to maintain stable operation. The results on minimum threshold and leakage current were cross-checked using a single chip assembly confirming no degradation over the number of thermal cycles applied.

The integration tests were carried out in a cleanroom at CERN. Each of the 10 sectors of the SPD was tested separately after arrival. The test system used the final power supply installation, cables and readout chain and cooling system as foreseen in the experiment. Each half-stave was tested electrically and using a source. In addition the temperature profile of the sectors was recorded using a thermal camera and Pt1000 sensors mounted on each half-stave. The detector control system allowed to control the read-

out, power supplies and cooling with the same interfaces as used in ALICE. Results of the sector tests are presented and compared to the results after integration into the two half-barrels. No deterioration in minimum threshold is observed. The total number of noisy pixels in the detector is ~ 51 compared to 10 million pixels in total. The mean leakage current is around $1.49 \pm 1.68 \mu\text{A}$.

After the integration tests were completed the detector was moved to the ALICE experiment and installed around the beampipe. First tests were carried out on the electronic readout system and showed full functionality. A complete test of the detector is only possible after connection to the cooling system which is foreseen to be completed by the end of November 2007.

Appendix A

Tables

Table A.1: Eye diagram half-barrel 1.

Half- Stave	t_{left} [ns]	σ_{left} [ps]	t_{right} [ns]	σ_{right} [ps]	μ_0 [mV]	σ_0 [mV]	μ_1 [mV]	σ_1 [mV]
1-C-1	502.473	112	503.719	111	585	6	993	8
2-A-0	502.434	121	503.736	106	498	8	911	5
2-A-2	502.430	93	503.746	72	165	6	308	4
2-A-5	502.410	105	503.635	102	500	9	898	6

Table A.2: Eye diagram half-barrel 2.

Half- Stave	t_{left} [ns]	σ_{left} [ps]	t_{right} [ns]	σ_{right} [ps]	μ_1 [mV]	σ_1 [mV]	μ_0 [mV]	σ_0 [mV]
5-A-0	502.467	69	503.750	58	518	26	909	8
5-A-1	504.986	64	506.206	62	507	30	869	6
5-C-0	505.038	71	506.272	66	360	9	619	7
5-C-1	505.008	50	506.295	59	495	11	833	5
6-A-2	504.900	54	506.116	64	670	10	1094	13
6-C-2	505.054	64	506.260	63	553	28	931	5
7-A-5	504.966	53	506.172	64	671	9	1080	11
7-C-5	505.018	71	506.234	60	517	29	888	6
8-A-3	504.912	85	506.130	79	666	9	1091	14
8-A-4	505.006	65	506.216	66	492	12	819	7
8-C-3	504.988	67	506.224	63	585	28	987	6
8-C-4	505.024	71	506.260	73	372	22	641	9
9-A-0	502.382	99	503.620	85	472	9	832	6
9-A-1	502.454	97	503.684	85	623	23	1031	9
9-C-0	499.924	70	501.192	53	582	12	982	8
9-C-1	502.528	67	503.651	64	377	31	594	21

Appendix B

General Principle of Semiconductors

In general the conductivity of a semiconductor is sensitive to temperature, illumination, magnetic field and the amount of impurity atoms. This sensitivity in conductivity makes this material interesting for electronic applications and detector physics. Since the 1960s silicon is the dominating material for semiconductors due to its much lower leakage current and the opportunity to grow silicon dioxide thermally. Further silicon in the form of silica and silicates comprises 25 % of the Earth's crust whereas Germanium can only be found in lower fraction in copper and tin ores. Compound semiconductors like gallium arsenide (GaAs) are mainly used in microwave and photonic applications. They have electrical and optical properties which are missing in Silicon.

B.1 Crystal Structure and Energy Bands

Semiconductor materials have a diamond lattice structure which belongs to the cubic-crystal family and in which all atoms are identical and build a covalent bonding with the nearest neighbors. Figure B.1 shows the position of Si atoms and their covalent bonds in a unit cell. Each atom in the diamond lattice is surrounded by four equidistant neighbors which are lying at the corners of a tetrahedron. At low temperatures, the electrons are bound in their respective tetrahedron lattice and are therefore not available for conduction. This changes at higher temperatures where due to thermal vibrations the covalent bonds can break. Out of this a free electron results

which then can participate in current conduction. The electrons of the atoms in the lattice can have only discrete energy levels. These energy levels are confined into two bands, which are separated by a region called *bandgap* E_g and which the electrons cannot possess. The upper band is called the *conduction band* while the lower band is called *valence band*. The bandgap is a characteristic value which classifies solids in insulators ($E_g \sim 9 \text{ eV}$), semiconductors ($E_g = 1 - 5 \text{ eV}$) and conductors where the valence band is partially filled or the valence and conduction band is overlapping.

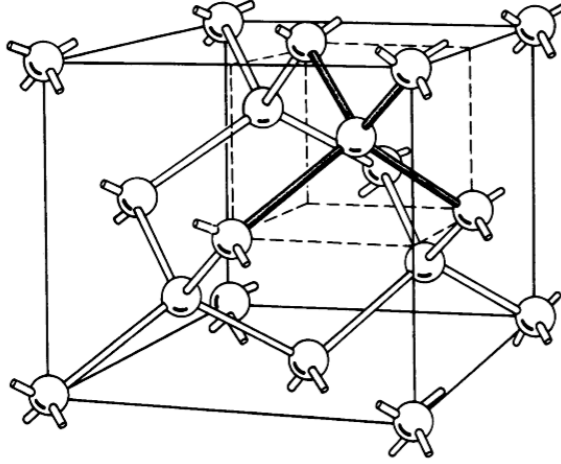


Figure B.1: Diamond lattice - the lines indicate the bonding between the nearest neighbours [26]

At room temperature and normal atmosphere the bandgap E_g is 1.12 eV for silicon and 1.42 for gallium arsenide, respectively and reaches 1.17 eV and 1.52 eV at 0 K. The thermal variation of the bandgap can be expressed as

$$E_g(T) = 1.17 - \frac{(4.73 \times 10^{-4})T^2}{(T + 636)}, \quad (\text{B.1})$$

for Si and

$$E_g(T) = 1.52 - \frac{(5.4 \times 10^{-4})T^2}{(T + 204)}, \quad (\text{B.2})$$

for GaAs. Thus the temperature coefficient $\frac{dE_g}{dT}$ is negative for both Si and GaAs which means that the bandgap decreases with increasing temperature [26].

B.2 Intrinsic Semiconductors

The continuous vibrations of the lattice lead to excitations of electrons from the valance to the conduction band leaving an equal amount of holes in the valence band. Compared to doped semiconductors materials (see Chapter 2.1) an *intrinsic semiconductor* contains only a small amount of impurities compared to electron hole pairs generated by thermal agitations. The probability that an electronic state with an energy E is occupied by an electron can be described with the *Fermi-Dirac-distribution function*

$$F(E) = \frac{1}{1 + e^{(E-E_F)/kT}}, \quad (\text{B.3})$$

where k is the Boltzmann constant, T the temperature in Kelvin and E_F is the *Fermi level*. The Fermi level is the energy at which the probability of occupation by an electron is exactly one half. Integrating the product of the Fermi-Dirac-distribution $F(E)$ and the density of allowed states per unit volume $N(E)$ leads to the electron density n in the conduction band

$$n = N_C \exp\left(-\frac{E_C - E_F}{kT}\right), \quad (\text{B.4})$$

where E_C is the energy at the bottom of the conduction band and N_C the effective density in the conduction band. For silicon at room temperature N_C is $2.8 \times 10^{19} \text{ cm}^{-3}$. A similar expression can be found for the hole density

$$p = N_V \exp\left(-\frac{E_F - E_V}{kT}\right), \quad (\text{B.5})$$

where N_V is the effective density of states in the valence band. For silicon at room temperature N_V is $1.04 \times 10^{19} \text{ cm}^{-3}$. As described above the number of electrons per unit volume in the conduction band is equal to the number of holes in the valence band, which defines the *intrinsic carrier density* as $n_i = n = p$. The intrinsic carrier density leads to the *mass action law* which can be defined as

$$n_i = \sqrt{N_C N_V} \exp\left(-\frac{E_g}{2kT}\right), \quad (\text{B.6})$$

where $E_g \equiv (E_C - E_V)$. For silicon at room temperature n_i is $1.45 \times 10^{10} \text{ cm}^{-3}$ [26].

Appendix C

List of Constants

- $\beta : \frac{v}{c}$
- v : Speed of incoming particle
- c : Speed of light
- γ : Lorentz factor = $\frac{1}{\sqrt{1-\beta^2}}$
- e : Electron charge
- m_e : Electron mass = 0.511 MeV
- N_a : Loschmidt (= Avogadro) number = $6.022 \cdot 10^{23} \text{ Mol}^{-1}$
- I : mean ionising energy (173 eV for silicon)
- Z_1 : atomic number of incoming particle
- Z, A : atomic number and atomic mass of absorber material
- ρ : density of absorber
- δ : Fermi density correction (6.02 for silicon)
- C : Shell correction
- ν : Quantum electrodynamic correction

List of Figures

1.1	The Large Hadron Collider and its experiments	1
1.2	ATLAS, CMS, ALICE, LHCb	2
1.3	Collision and expansion of two lead bunches	5
1.4	Overview of the ALICE experiment	6
1.5	Photograph of the HMPID	7
1.6	Scheme of the PHOS detector	7
1.7	Scheme of the cross-section of the PMD	8
1.8	Photograph of the TPC	9
1.9	Schematic of the placement of T0, V0 and FMD	10
1.10	The array of super modules of the EMCAL	12
1.11	The complete SSD mounted on CF support	13
1.12	Ladder of the ITS Silicon Drift Detector	13
1.13	The ALICE Silicon Pixel Detector	14
2.1	Schematic bond pictures for doped silicon	16
2.2	Current conduction in a uniformly doped semiconductor	18
2.3	pn-junction	20

2.4	p ⁺ n junction reversed biased	23
2.5	Mean energy loss rate in different materials	24
2.6	Growing techniques for producing silicon ingots	26
2.7	Layout of a silicon strip detector	27
2.8	Layout of a hybrid silicon pixel detector	29
2.9	Basic principle of a hybrid pixel detector	29
2.10	Monolithic pixel detector	30
2.11	Operating principle of a silicon drift detector	31
3.1	Schematic view of both half-barrels	33
3.2	Numbering of the half-staves seen from side A	34
3.3	Scheme of a half-stave	34
3.4	Picture and layout of a sensor ladder	36
3.5	The tdi/tfo interconnections between the pixel chips	36
3.6	Block diagram of a pixel cell	37
3.7	5" sensor wafer	38
3.8	Multi-Chip-Module	38
3.9	Cross section through a half-stave	39
3.10	SEM picture of an Al-microvia	39
3.11	Karl Süß probe station	40
3.12	Yield of the ladder production	43
3.13	Number of non working pixels	43
3.14	Structure of the DAQ and DCS System	46
3.15	GUI of the SPDMOOD and Reference Data Display	47

<i>LIST OF FIGURES</i>	95
3.16 Picture of Router and wirebonds	48
3.17 Leakage current of a half-stave of a half-stave	49
3.18 Temperature distribution of a half-stave	49
3.19 Minimum threshold scan of a half-stave - Reference Data Display	50
3.20 Minimum threshold scan of one half-stave - SPDMOOD	51
3.21 Source test of a half-stave	51
3.22 Picture of non working pixels on a chip	52
3.23 Schema of temperature cycling profile	53
3.24 Heating chamber	55
3.25 Cycling parameters	56
3.26 Minimum threshold of half-stave (Aging tests)	57
3.27 Leakage current of half-stave (Aging tests)	57
3.28 Leakage current of assembly (Aging tests)	59
3.29 Minimum threshold of readout chip (Aging tests)	59
3.30 Minimum threshold of assembly (Aging tests)	60
3.31 Dead columns after each cycling period	60
3.32 Araldite and Globtop on wire bonds	61
3.33 Setup for the optical tests of HB 1	62
3.34 Setup for the optical tests of HB 2	63
3.35 Eye diagram	63
3.36 Optical Power of all half-staves of Half-Barrel 1	66
3.37 Optical Power of all half-staves of Half-Barrel 2	66
3.38 Extinction ratio of the half-stave sample	68

3.39	Q_{Eye} of the half-stave sample	69
4.1	Carbon fiber support	71
4.2	Infrared picture of the outer layer of an half sector	72
4.3	Test bench	73
4.4	Test setup of the SPD sector and half-barrel tests	75
4.5	Position of a sector during the cosmic run	76
4.6	Visual inspection	76
4.7	Leakage current of all half-staves - sector test	77
4.8	Leakage current of all half-staves - half-barrel test	78
4.9	Temperature distribution of all half-staves - sector test	79
4.10	Temperature distribution of all half-staves - half-barrel test	79
4.11	Minimum threshold - sector test	80
4.12	Minimum threshold - half-barrel test	80
4.13	Noisy pixel of each Sector - sector test	81
4.14	Noisy pixel of each Sector - half-barrel test	82
4.15	Z correlation of inner and out layer of a sector	82
4.16	Schematic of SPD installation	83
4.17	Half-barrel around beam pipe	84
4.18	ITS adjacent to the absorber	84
B.1	Diamond lattice	90

List of Tables

3.1	Material Budget of one SPD Layer	35
3.2	Ladder classification	42
3.3	Summary of the half-stave measurements carried out after the cycling	55
3.4	Power output of each half barrel	65
3.5	Eye width τ_{Eye} , extinction ratio ER and quality factor Q_{Eye} for some half-staves of HB 1	67
3.6	Eye width τ_{Eye} , extinction ratio ER and quality factor Q_{Eye} for some half-staves of HB 2	68
4.1	Functionality tests	74
A.1	Eye diagram half-barrel 1	88
A.2	Eye diagram half-barrel 2	88

Bibliography

- [1] LHC Machine Outreach. Website, 2007. <http://lhc-machine-outreach.web.cern.ch/lhc-machine-outreach>.
- [2] CERN Web. Website, 2007. <http://www.cern.ch>.
- [3] The ATLAS Experiment. Website, 2007. <http://atlas.ch/index.html>.
- [4] CMS Experiment at LHC. Website, 2011. <http://cmsinfo.web.cern.ch/cmsinfo/Detector/index.html>.
- [5] H.Tydesjo. *Net-Charge Fluctuations in Ultra-Relativistic Nucleus-Nucleus Collisions*. PhD thesis, Department of Physics Lund University, 2004.
- [6] ALICE Web. Website, 2007. <http://aliceinfo.cern.ch/Collaboration/index.html>.
- [7] S Kiselev, W Klempt, Andreas Morsch, G Paic, Jean Pierre Charles Revol, and K Safark. *Day One Proton-Proton Physics with the ALICE Central Detector*, 2000. ALICE-INT-2000-28. CERN-ALICE-INT-2000-28.
- [8] B. Belin. The Construction of the ALICE HMPID RICH Detector. *Proceedings of HCP 2005*, 2005. Prepared for Hadron Collider Physics Symposium 2005, Les Diablerets, Switzerland, 4-9 Jul 2005.
- [9] A. Gallas. Experience from the Construction and Installation of the HMPID CsI-RICH Detector in ALICE. *Nuclear Instruments and Methods*, A581:402–405, 2007. Proceedings of the 11th VCI 2007.
- [10] Alice photographs by a.saba. Website, 2007. http://aliceinfo.cern.ch/Public/Photos/Saba_mainshots.
- [11] *A High Resolution Electromagnetic Calorimeter based on Lead-Tungstate Crystals*, 2005. ALICE-INT-2005-053.

- [12] Per Thomas Hille. *Commissioning of the ALICE PHOS Detector and Integration into the ALICE High Level Trigger*. PhD thesis, Oslo, U., 2009. Presented on Jan 2009.
- [13] *ALICE Photon Multiplicity Detector (PMD) : Technical Design Report*, 1999. CERN-LHCC-99-032.
- [14] The ALICE Collaboration et al. The ALICE experiment at the CERN LHC. *Journal of Instrumentation*, 3, 2008. JINST 3 S08002.
- [15] Tariq Mahmoud. The ALICE Transition Radiation Detector (TDR) : Technical Design Report. *Nucl. Instrum. Methods Phys. Res., A 502 (2003) 127-132*, 2003.
- [16] *The ALICE Transition Radiation Detector (TDR) : Technical Design Report*, 2001. CERN-LHCC 2001-021.
- [17] *ALICE Time Projection Chamber (TPC) : Technical Design Report*, 2000. CERN-LHCC-2000-001.
- [18] *ALICE forward detectors: FMD, T0 and V0 : Technical Design Report*, 2004. CERN-LHCC-2004-025.
- [19] E. Scapparone. The Time of Flight Detector of the ALICE Experiment. *Journal of Physics G: Nuclear and Particle Physics*, 34(8):725 – 728, 2006. Proceedings of the QM06, 10.1088/0954-3899/34/8/S82.
- [20] *The ALICE Time of Flight (TOF) : Technical Design Report*, 2000. CERN/LHCC 2000-012.
- [21] The ALICE Time of Flight Detector. Website, 2011. http://aliceinfo.cern.ch/Public/en/Chapter2/Chap2_TOF.html.
- [22] J P Coffin. Development and tests of double-sided silicon strip detectors and read-out electronics for the internal tracking system of alice at lhc. *Nucl. Phys. A*, 1999. CERN-ALI-99-01. CERN-ALICE-PUB-99-01.
- [23] *ALICE Inner Tracking System (ITS) : Technical Design Report*, 1997. CERN-LHCC-99-012.
- [24] S. Beole et al. The ALICE Silicon Drift detectors: Production and assembly. *Nuclear Instruments and Methods in Physics Research Section A: Accelerators, Spectrometers, Detectors and Associated Equipment*, 582(3):733 – 738, 2007. Proceedings of the 15th International Workshop on Vertex Detectors VERTEX 2006, <http://www.sciencedirect.com/science/article/pii/S0168900207015343>, 10.1016/j.nima.2007.07.087.

- [25] P. Riedler et al. The ALICE Silicon Pixel Detector: System, Components and Test Procedures. *Nuclear Instruments and Methods in Physics Research Section A: Accelerators, Spectrometers, Detectors and Associated Equipment*, 568(1):284 – 288, 2006. Proceedings of Proceedings of the 10th European Symposium on Semiconductor. Waldbadkreuth, <http://www.sciencedirect.com/science/article/pii/S0168900206011211>, 10.1016/j.nima.2006.05.265.
- [26] S.M. Sze. *Semiconductor Devices - Physics and Technology*. John Wiley and Sons, 1985.
- [27] Carl Hepburn. Britney's Guide to Semiconductor Physics. Website, 2007. <http://britneyspears.ac/lasers.htm>.
- [28] M. Krammer. Detectoren in der Hochenergiephysik. *Lecture notes*, 2005.
- [29] W.R. Leo. *Techniques for Nuclear and Particle Physics Experiments*. Springer-Verlag, 1987.
- [30] C.W. Fabjan. Grundlagen der Teilchendetektoren. *Lecture notes*, 2004.
- [31] Particle Data Group. *Particle Physics Booklet*. Institute of Physics Publishing, 2006.
- [32] P.Riedler. Silicon Pixel Detectors. *Lecture notes*, 2006.
- [33] G. Lutz. *Semiconductor Radiation Detectors*. Springer-Verlag, 1999.
- [34] A. Kluge et al. The ALICE Silicon Pixel Detector: Electronics System Integration. *Proceedings of IEEE 2005*, 2:761 –764, 2005. 10.1109/NSS-MIC.2005.1596367.
- [35] M. Caselle et al. Assembly Procedure of the Module (Half-Stack) of the ALICE Silicon Pixel Detector. *Proceedings of 9th Pisa Meeting and Advanced Detectors*, 2003. published in Nuclear Instruments and Methods in Physics Research A, 501 p. 111 - 118.
- [36] Fadmar Osmic. The ALICE Silicon Pixel Detector System. PHD Thesis, 2005. Technical University of Vienna.
- [37] M. Burns et al. The ALICE Silicon Pixel Detector Readout (s)ystem. *Proceedings of the 6th Workshop on Electronics for LHC Experiments in Krakow, Poland*, page pp. 105, 2000.
- [38] P. Riedler et al. Progress on Alice Pixel Detector Commissioning. *PoS, Proceedings of VERTEX 2007:3*, 2007.

- [39] Helen Cui. Accelerated Temperature Cycle Test and Coffin-Manson Model for Electronic Packaging. pages 556 – 560, 2005. <http://ieeexplore.ieee.org/iel5/9660/30517/01408421.pdf?arnumber=1408421>.
- [40] Michel R. Massénat. *Multi-Chip-Modules, dhier ... et de demain*. Polytechnica, 1999.
- [41] Horst Alexander Schödl. Commissioning and Calibration of the ALICE SPD Optical Data Links. Project Work, 2007. Technical University of Vienna.
- [42] Carsten Schmidt-Langhorst. *Optical Sampling of High Bit Rate Optical Data Signals*. PhD thesis, Technical University of Berlin, 2004.
- [43] Michel Morel. Website, 2007. <http://morel.web.cern.ch/morel/cgi-bin/alice.htm>.
- [44] A. Pepato et al. The Mechanics and Cooling System of the ALICE Silicon Pixel Detector. *Proceedings of the PIXEL 2005 Conference*, 2005.